Doctoral Dissertation

Development of Numerical Model for Washcoated
Honeycomb Monolith Catalyst based on Surface and
Gaseous Species Measurements
（気相・表面化学種計測に基づくウォッシュコ
ートハニカムモノリス触媒の数値モデル開発）

SET NAING

March 2021

Graduate School of Engineering

Hiroshima University

Development of Numerical Model for Washcoated Honeycomb

Monolith Catalyst based on Surface and Gaseous Species

Measurements

by

SET NAING

A Dissertation for Doctor of Engineering Degree submitted to
Graduate School of Engineering
Department of Mechanical Science and Engineering
Hiroshima University
in
March 2021

Supervised by

Assoc. Prof. Dr. Daisuke Shimokuri

Committee members

Prof. Dr. Akira Miyoshi

Prof. Dr. Keiya Nishida

Prof. Dr. Takayuki Ichikawa

Assoc. Prof. Dr. Youichi Ogata

List of publications

Journal publications:

1. D. Shimokuri, H. Murakami, S. Hinokuma, Y. Matsumoto, S. Naing, K. Naito, H. Yokohata, H. Takebayashi & A. Miyoshi (2020): Development of Surface Reaction Mechanisms of CO/O_2 on Pt and Rh for Three-Way Catalyst based on Gas Phase and Surface Species Analyses, Combustion Science and Technology, Combustion Science and Technology. Taylor & Francis, 00(00), pp. 1–23, in press. doi: 10.1080/00102202.2020.1817905.

2. S. Naing, I. P. A. Kristyawan, H. Murakami, S. Hinokuma, Y. Matsumoto, T. Omori, Y. Wang, H. Yokohata, M. Kawano, H. Takebayashi, A. Miyoshi & D. Shimokuri (2020): Development of Detailed Surface Reaction Mechanism of C_2H_4/C_3H_6 Oxidation on Pt/Al_2O_3 Monolith Catalyst Based on Gas Phase and Surface Species Analyses, Combustion Science and Technology. Taylor & Francis, 00(00), pp. 1–21, in press. doi: 10.1080/00102202.2020.1731486.

Peer-reviewed conference publication:

3. S. Naing, I. P. A. Kristyawan, D. Shimokuri, S. Hinokuma, H. Murakami, Y. Matsumoto, H. Takebayashi, A. Miyoshi (2019): Development of C_3H_6 surface reaction mechanism on Pt/Al_2O_3 monolith catalyst based on gaseous and surface species measurements, 12th Asia-Pacific Conference on Combustion, Fukuoka International Congress Center, Fukuoka, Japan, 1st -5th July 2019.

Acknowledgements

University.

My deepest and sincere thanks to my beloved parents, family and Dr. Han Htoo Htoo Ko. Without their kind support and encouragement, I would not have done this much during my further study.

Finally, my special thanks and appreciation to my seniors and friends both in Myanmar and Japan for their kind support and understanding.

Abstract

In this thesis, numerical modelling study of washcoated honeycomb monolith catalyst is presented based on the experimental measurements. Reactivity of important hydrocarbon species from internal combustion engines are investigated to observe the dominant hydrocarbon species that can promote the light-off performance, and reaction characteristics of C_2H_4 / O_2 and C_3H_6 / O_2 on practical Pt/Al_2O_3 monolith catalyst are investigated by gas phase conversion experiments with Fourier Transform Infrared (FT-IR), and surface species experiments with *in-situ* FT-IR. Gas phase experimental results show that the light-off temperature as well as complete conversion temperature of both C_2H_4 / O_2 and C_3H_6 / O_2 mixture shift to lower side of the temperature with the increase in oxygen concentration. The surface species analyses show the presence of stable intermediate CH_x species and linearly adsorbed CO on the platinum surface. A detailed surface reaction mechanism is proposed by taking the observed surface species and their occupied active surface sites into account. Importance of more than one active metal surface site occupations at the adsorption step of C_2H_4 or C_3H_6 and multiple-sited stable intermediate CH_x species are considered in the proposed detailed reaction mechanism. Numerical modelling method, in which a single cell of monolith honeycomb reactor can be modelled, not only along the gas flow channel direction but also into the washcoat layer direction independently with proper considerations of flow model, heat and mass transfer model, and the transport model into the washcoat layer, is used together with the proposed developed detailed surface reaction mechanism for numerical simulations. Numerically simulated light-off performance with the proposed reaction mechanism shows good agreement with the experimental results of C_2H_4 / O_2 and C_3H_6 / O_2 over different oxygen concentration from fuel lean to fuel rich conditions. Moreover, simulation results also agree well with the additional experimental results with multiple gas compositions and validate the proposed detailed reaction mechanism. Finally, from the experimental measurement results and numerical simulation results, influence of multiple-sited intermediate hydrocarbon surface species on the light-off temperature and complete conversion temperature is discussed.

List of symbols

Symbol	Description	Units
a	Constant in the laminar friction approach	(-)
A_{cross}	Cross sectional area of computational cell	(m^2)
$A_{f,i}$	Pre-exponential factor of the rate constant of forward reaction step of reaction i	(variable)
A_i	Pre-exponential factor of the rate constant of reaction i	(variable)
A_{PGM}	Total surface area of noble metal responsible for the catalytic reaction	(m^2)
$A_{r,i}$	Pre-exponential factor of the rate constant of backward reaction step of reaction i	(variable)
b	Constant in the laminar friction approach	(-)
b_i	Temperature exponent in the rate constant of reaction i	(-)
$c_{k,g}$	Concentration of gas or surface species k	(kmol/m^3)
c_k^0	Reference concentration of gas or surface species k	(variable)
$c_{k,g}^B$	Molar concentration of species k in the bulk gas phase	(kmol/m^3)
c_k^L	Concentrations of species k in the reactive surface layer	(kmol/m^3)
c_p	Specific heat at constant pressure of the entire gas phase	(kJ/(kmol·K))
$c_{p,s}$	Specific heat of the solid phase	(kJ/(kg·K))
d	Diameter	(m)
d_{hyd}	Hydraulic channel diameter	(m)
d_{mat}	Diameter of the insulation material	(m)
d_{mon}	Diameter of the monolith catalyst	(m)
d_{pore}	Pore diameter	(m)
d_{shell}	Diameter of the quartz tube reactor shell	(m)
$D_{k,eff}$	Effective mean diffusion coefficient	(m^2/s)
$D_{k,g}$	Diffusion coefficient of species k in gas mixture	(m^2/s)
D_{Kn}	Knudsen diffusion coefficient	(m^2/s)
E_i	Activation energy of the rate constant of reaction i	(kJ/kmol)

$E_{f,i}$	Activation energy of the rate constant of forward reaction step of reaction i	(kJ/kmol)
$E_{r,i}$	Activation energy of the rate constant of backward reaction step of reaction i	(kJ/kmol)
Gz	Graetz number	(-)
Gz_{heat}	Graetz number for heat transfer	(-)
Gz_{mass}	Graetz number for mass transfer	(-)
h_g	Enthalpy of the entire gas phase	(kJ/kmol)
$h_{k,g}$	Enthalpy of species k in the gas phase	(kJ/kmol)
H_k	Enthalpy of species k	(kJ/kmol)
Δh_i	Heat of reaction i	(kJ/kmol)
ΔH_i	Enthalpy of reaction i	(kJ/kmol)
$\Delta_R H_i$	Enthalpy difference between forward and backward reaction steps of reaction i	(kJ/kmol)
k_{fi}	Forward rate constant of reaction i	(variable)
k_{ri}	Backward rate constant of reaction i	(variable)
k_h	Heat transfer coefficient	(W/(m^2·K))
$k_{k,m}$	Mass transfer coefficient of species k	(m/s)
$k_{mixture}$	Thermal conductivity of the gas mixture	(W/(m·K))
k_{out}	Heat transfer coefficient to the environment	(W(m^2·K))
K_{ci}	Equilibrium constant in concentration units for reaction i	(variable)
K_{pi}	Equilibrium constant in pressure units for reaction i	(variable)
l	Channel, monolith length	(m)
m	Sum of all stoichiometric coefficients	(-)
$\dot{m}$	Mass flux of gas phase	(kg/m^2·s)
M_k	Molar mass of the specific species k	(kg/kmol)
MG_g	Molar mass of the entire gas phase	(kg/kmol)
$MG_{k,g}$	Molar mass of the species k in the gas phase	(kg/kmol)
M_{PGM}	Molar mass of noble metal	(kg/kmol)
Nu	Nusselt number	(-)
p_0	Standard state pressure	(-)

p_g	Pressure of entire gas phase	(Pa)
Pr	Prandtl number	(-)
$\dot{q}_{ext}$	Heat loss to the external surroundings	(W/m^3_cat)
$\dot{q}_i$	Rate of progress of reaction i	(kmol/(m^2·s))
$\dot{q}_{mat}$	Heat loss from the insulation material	(W/m^3_mat)
$\dot{q}_{mon}$	Heat loss from the monolith catalyst	(W/m^3_cat)
$\dot{q}_{shell}$	Heat loss from the quartz tube reactor shell	(W/m^3_shell)
Q_i^0	Reaction quotient evaluated at reference concentration	(variable)
$\dot{Q}_{mass,mixture}$	Mass transfer rate of the gas mixture	(mol/s)
$\dot{r}_i$	Reaction rate of reaction i per catalyst unit volume	(kmol/(m^3_cat·s))
$\dot{r}_k$	Reaction rate of species k	(kmol/(m^3·s))
$\overline{\dot{r}_i}$	Reaction rate or reaction i per washcoat unit volume	(kmol/(m^3_wcl·s))
R	Universal gas constant	(kJ/(kmol·K)
Re	Reynolds number	(-)
s	Monolith repeat thickness	(m)
Sc	Schmidt number	(-)
Sh	Sherwood number	(-)
S_k	Entropy of species k	(kJ/kmol·K)
ΔS_i	Entropy of reaction i	(kJ/kmol·K)
$\Delta_R S_i$	Entropy difference between forward and backward reaction steps of reaction i	(kJ/kmol·K))
t	Time	(s)
T_e	Environment temperature	(K)
T_g	Gas temperature	(K)
T_s	Solid temperature	(K)
ΔT_{s-e}	Temperature difference between solid and environment	(K)
v_g	Mean mass weighed gas velocity	(m/s)
$v_{k,g}$	Velocity of the species k in gas phase	(m/s)
$v_{k,g}^D$	Diffusive velocity of the species k in gas phase	(m/s)
V	Volume of computational cell	(m^3)
V_g	Volume of computational cell (gaseous part)	(m^3)

V_{conv}	Volume of converter (monolith)	(m^3)
$w_{k,g}$	Mass fraction of the species k in gas phase	(-)
w_k^B	Mass fraction of the species k in the bulk gas	(-)
w_k^L	Mass fraction of the species k in the washcoat layer	(-)
W_{PGM}	Metal loading of the noble metal	(g/L)
$y_{k,g}$	Molar fraction of the species k in gas phase	(-)
z	Spatial coordinate in Cartesian coordinates	(m)
α_{out}	Heat transfer coefficient between shell and environment	(W/m^2)
γ_{cat}	Metal dispersion	(%)
γ_i	Sticking coefficient of the reaction i	(-)
Γ_{tot}	Total surface site concentration	(mol/m^2)
δ	Total thickness of monolith's wall	(m)
δ_{wall}	Thickness of substrate wall	(m)
δ_{wcl}	Thickness of washcoat	(m)
ε_g	Gas or fluid volume fraction	(m^3/m^3)
ε_{ki}	Surface coverage parameter of surface site species k in reaction i	(-)
ε_s	Solid volume fraction in catalyst	(m^3/m^3)
ε_{wcl}	Porosity of washcoat in catalyst	(-)
ζ	Friction factor	(-)
ζ_{lam}	Laminar friction factor	(-)
η_{ki}	Surface coverage parameter of surface site species k in reaction i	(-)
κ_k	Symbol for the species k	(-)
λ_g	Thermal conductivity of gas	(W/(m·K))
λ_{mat}	Thermal conductivity of the insulation material	(W/(m·K))
λ_s	Thermal conductivity of solid	(W/(m·K))
λ_{shell}	Thermal conductivity of the quartz tube reactor shell	(W/(m·K))
μ_{ki}	Surface coverage parameter of surface site species k in reaction i	(-)
ρ_g	Density of the entire gas phase	(kg/m^3)

$\rho_{k,g}$	Density of the species k in gas phase	(kg/m^3)
ρ^B	Density of the bulk gas	(kg/m^3)
ρ^L	Density of the gas mixture in the washcoat layer	(kg/m^3)
ρ_s	Solid density	(kg/m^3)
$v_{i,k}$	Stoichiometric coefficient of species k in reaction i	$(-)$
θ_k	Surface coverage fraction of species k	$(-)$
Θ	Site density	$(kmol/m^2)$
σ_k	Number of surface sites occupied by species k	$(-)$
τ_{wcl}	Tortuosity of washcoat in catalyst	$(-)$
ϕ	Equivalence ratio	$(-)$
φ	Fanning friction factor	$(-)$

List of abbreviations

ATM   Aftertreatment Model

CPSI   Cell Per Square Inch

CPSM   Cells Per Square Meter

CR   Conversion Rate

DFT   Density Functional Theory

DOC   Diesel Oxidation Catalyst

FT-IR   Fourier Transform Infrared

GSA   Geometric Surface Area

IC   Internal Combustion

MCT   Mercury Cadmium Telluride

PGM   Platinum Group Metal

RDE   Real Driving Emissions

SF-MS   Single Focusing Mass Spectrometer

TWC   Three Way Catalyst

WLTC   Worldwide harmonized Light vehicles Test Cycle

List of tables

List of figures

Table of contents

Chapter 1

Introduction

1.1   Background

Worldwide exhaust gas emission standards for automotive vehicles, such as carbon monoxide (CO), nitrogen oxides (NO_x) and hydrocarbons (HCs), are becoming considerably more stringent year by year.   State-of-the-art regulations, such as Euro 6d or US Tier 3 standards start to enforce nowadays and other regulations as well.   In Fig. 1.1, non-methane hydrocarbon standards of Europe and Japan can be observed and automotive makers using internal combustion (IC) engines are trying their best to meet these kinds of regulations.

In addition, modernized test cycles like WLTC and JC08 become representatives to test the emission standards of the fossil fuel using vehicles.   Driving cycles including different modes, such as urban driving or motorway driving, and variations of vehicle speeds from low to high speed, are being tested in order to regulate the emission standards at each transient period.   An example image of the speed variations during a JC08 driving cycle is shown in Fig. 1.2.   Moreover, new and additional vehicle test mode such as Real Driving Emissions (RDE) is introduced to check and test on the public real-life driving conditions.   On the mode, gaseous compositions as well as temperatures tend to be drastically fluctuated (Delphi, 2020).

Usually, in IC engine powered vehicles, toxic substances from exhaust gases are purified by the catalytic converter before they emit from the tailpipe into the surroundings. Inside the catalytic converter, there is Three Way Catalyst (TWC) for gasoline vehicles or Diesel Oxidation Catalyst (DOC) for diesel vehicles, which convert these pollutants mostly into nitrogen, carbon dioxide and water vapor (Kummer, 1980).   However, automakers depending on the IC engine power sources try to develop their technologies competitively in order to increase the fuel efficiency and durability of hybrid power resources.   Work generated and heat dissipated from the combustion of fossil fuel resources in the IC engines are being tried to recover or conserve as much as possible. State-of-the-art IC engine technologies include thermally efficient lean burn technologies so that the average exhaust gas temperature tends to be decreased significantly (Srivastava et al., 2018).   Such kind of low exhaust gas temperature conditions make the catalytic

converter difficult to convert the harmful gases resulting higher number of emissions, especially for TWC of gasoline engines because the exhaust gas composition tends to be out of so-called "window" due to the lean combustion. The narrow range of equivalence ratios at which all of the major pollutants can be eliminated simultaneously by a TWC is shown in Fig. 1.3 (Kummer, 1980).

Furthermore, cold engine start is an important issue, especially for HCs emissions, since the catalyst is mostly inactive during the cold start period. Therefore, catalysts are strongly required to be activated for the wide range of temperature or gaseous compositions of exhaust gas conditions (Malamis et al., 2018). To develop such system, the computer aided development, i.e., numerical modelling which is capable of quantitative predictions of catalyst performance is desired. Development of catalytic performance by the experiments is costly and a task of time consuming. Numerical modelling can provide an alternate method for the investigation of catalytic performance of a converter.

Automotive catalytic converter is mostly designed as monolithic honeycomb structure which consists of cordierite ceramic catalyst support and washcoat layer. It is made in such a way that a large catalytic surface area, low pressure loss, high thermal stability and strong mechanical strength can be achieved in a single design. The monolithic structure contains several parallel cell channels. Inside each channel, there is a layer of washcoat which consists mainly of platinum group noble metals such as platinum (Pt), palladium (Pd) or rhodium (Rh). Catalytic conversion of harmful exhaust gases is mainly carried out on the noble metal of the washcoat layer and on the support material in some kinds of catalysts as well. Support materials are usually made up of alumina (γ-Al_2O_3) and ceria (γ-Al_2O_3/CeO_2). Addition of cerium oxide to the support material features the storage and release of oxygen which is considerably advantageous during the lean and rich operations. State-of-the-art catalysts are made up of various noble metals and support materials for the purpose of having significant durability and longevity (Malamis et al., 2018). Structure of a catalytic converter, washcoat layer and demonstration from macro scale to nano scale are shown in Fig. 1.4.

Since the structure and functions of a catalytic converter is complicated, numerical modelling of catalytic performance of it is quite challenging. There are numerous physical and chemical parameters such as flow field description, heat and mass transfer phenomena, diffusion transport phenomena, and catalytic surface reaction chemistry. Therefore, careful considerations of these parameters are needed in order to obtain a good numerical model for catalytic performance predictions.
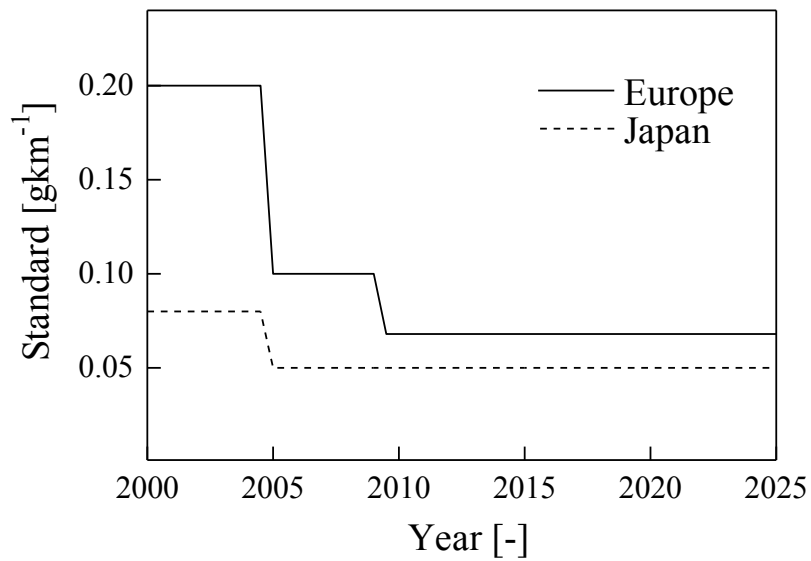
Fig. 1.1 Non-methane hydrocarbon emission standards of Europe and Japan
(Data adapted from passenger cars and light duty vehicles, worldwide emission
standards, Delphi 2020)
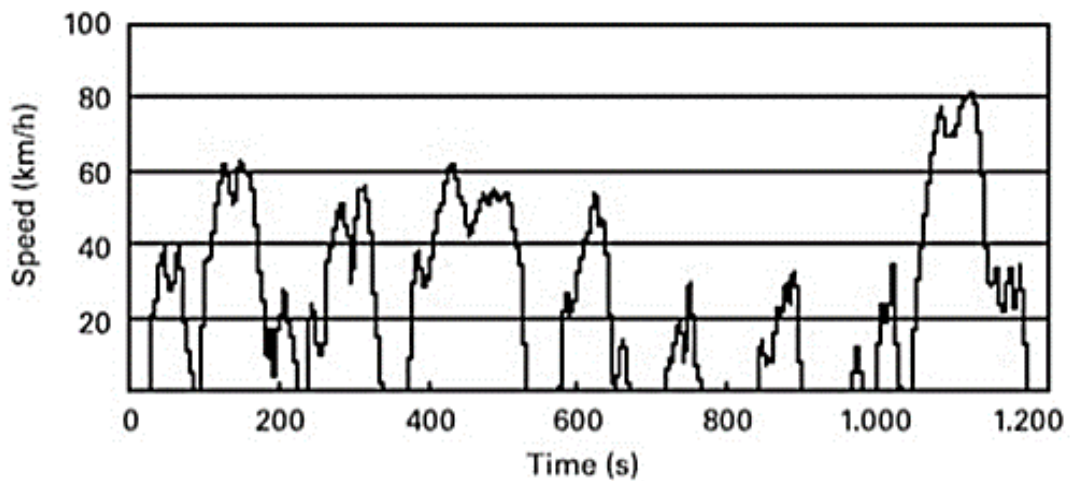
Fig. 1.2 JC08 driving cycle
(Image from passenger cars and light duty vehicles, worldwide emission standards,
Delphi 2020)

3
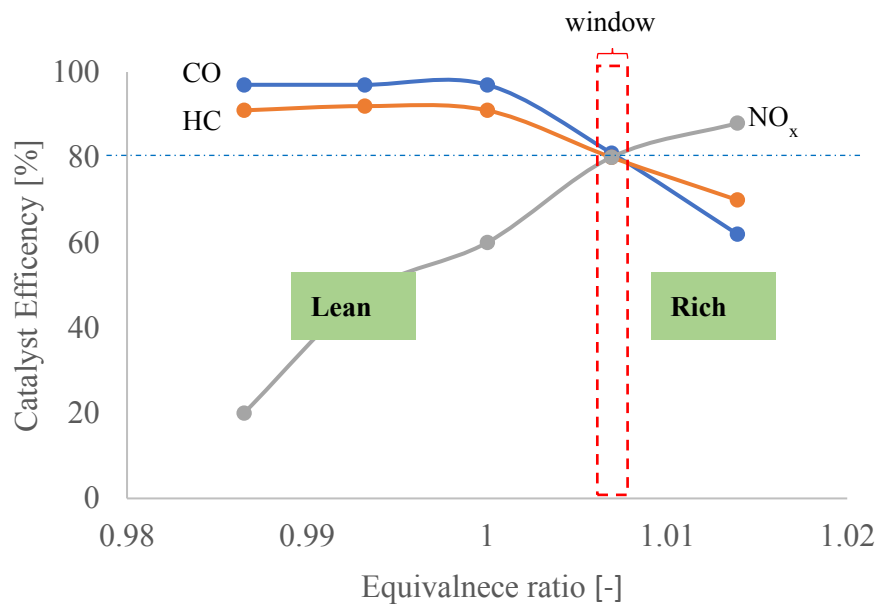
Fig. 1.3   Illustration of "window" in a TWC of a gasoline powered vehicle
(Data adapted from catalysts for automobile emission control, Kummer 2018)
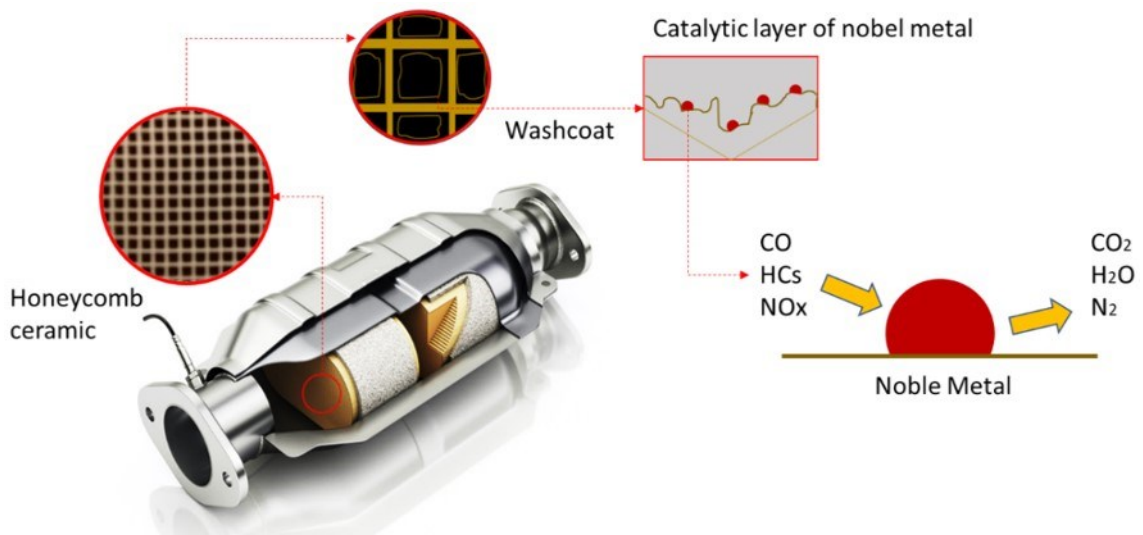
Fig. 1.4   Structure of a catalytic converter
(Part of the image from post catalyst fuel trim system too lean (Bank 1), Staff
Writers 2020)

1.2   Research studies of numerical modelling

Recent progress on the computer performance as well as the measurement techniques led to the deep understanding, and thus, the drastic improvement of numerical modelling of these processes.   Several models of monolith honeycomb catalyst which can be applied even for the practical automotive car system have been appeared (Deutschmann, 2015; Hayes and Kolaczkowski 1998; Mladenov et al., 2010).   In these models, not only the gas flow in the monolith cell but also the diffusions of reactants into the washcoat layer have been included (Hayes and Kolaczkowski 1998; Hayes et al., 2000; Wakao and Smith, 1962).   However, numerical predictions of catalytic conversion still have limitations.   This is because of the lack of accurate "surface reaction mechanism", which describes the adsorption, oxidation / reduction reaction and desorption processes.

In most of the recent studies, global models for the reaction mechanisms are used so that their validation of range of the gas compositions and conditions are mostly applicable for the fitting of the global reaction rate coefficients.   Therefore, detailed surface reaction mechanisms in which various single reactions occurring on the surface are more preferred to the global surface reaction mechanisms.   Several detailed surface reaction mechanisms have been proposed (Chatterjee et al., 2001; Koop and Deutschmann, 2009; Kota et al., 2017; Rankovic et al., 2011), however, their applicable gaseous composition or PGM compositions are quite limited.

These limitations are considered to come from their treatment of surface species. Even CO is known to have several adsorption regimes depending on the catalytic metal species and gaseous conditions, i.e., CO adsorb on PGM not only by linear regime but also by twin or bridge regime (Almusaiteer and Chuang, 2000; Demoulin et al., 2005; Holmgren et al., 1999; Sasmaz et al., 2017; Trautmann and Baerns, 1994).   Such absorption regimes have never been considered in surface reaction mechanisms, therefore, in our work (Shimokuri et al., 2020), surface reaction mechanisms for CO / O_2 on Pt and Rh have been constructed based on gaseous as well as surface species measurements. Results show that the mechanisms can reproduce gaseous conversion of monolith honeycomb catalyst and tendency of surface species coverage.   Furthermore, conversions of bimetal catalysts are well reproduced with the mechanism for wide range of (Pt : Rh) ratio.   Inclusion of surface species adsorption regime lead to the successful development of CO / O_2 reaction mechanism on Pt and Rh.

As for hydrocarbons (HCs), several detailed surface reaction mechanisms have been proposed (Chatterjee et al., 2001; Koop and Deutschmann, 2009; Kota et al., 2017),

however, their proposed reaction mechanisms have limited predictability and their validated gas compositions range are either narrow or very few conditions. There are deviations of light-off temperatures and inverse hysteresis behavior during the oxidation of HCs and they reported that these come from the simplified mixture of HCs and due to the blocking of active surface sites by the hydrocarbon intermediate species. Moreover, in their study, adsorption regimes of HCs have hardly been considered. On the other hand, recent development of fundamental research using Density Functional Theory (DFT) revealed that HC initially adsorb on PGM with single site occupation, but with three sites occupations during the decomposition process (Chesters et al., 1990; Kesmodel et al., 1979; Mohsin et al., 1988; Tsai et al., 1997; Zaera and French, 1999). Such multiple site occupations strongly affect to the progress of surface reaction, and therefore, must be considered for the detailed surface reaction mechanism. Moreover, in the modelling studies of HC catalytic reactions, propylene (C_3H_6) is mostly used as representative of HCs for both global and detailed kinetics despite the fact that actual HC composition in exhaust gas contains various kinds with different structures (Buzková Arvajová et al., 2018; Chatterjee et al., 2001) and an example of HC composition in the cold start period is shown in Fig. 1.5 (Kubo, 1995).

1.3   Objective

The objective of this study is to propose a numerical model with a detailed hydrocarbon surface reaction mechanism by taking the possibilities of more than one active surface PGM site occupations by the intermediate hydrocarbon species into account. In order to develop it, hydrocarbon species which may dominate the catalytic ignition are required to be investigated, and the important HC species that are typical components of unburned HCs emitted from the internal combustion engines are examined first to understand their reactivity. Gaseous conversion experiments of selected HC species are conducted and compared, and from these results, a detailed ethylene (C_2H_4) and propylene (C_3H_6) surface reaction mechanism on the practical platinum alumina (Pt/Al_2O_3) monolith catalyst is proposed from the aspect of more than one occupied active surface sites by the C_2H_4 and C_3H_6 intermediate species.

In the numerical model proposed in this study, proper considerations of flow along the cell channels, heat and mass transfer in the cells and diffusion inside the washcoat layer are included with experimentally determined physical parameters, and the detailed surface reaction mechanism proposed in this study is developed by using gaseous species conversion experiments and surface species experiments. Gaseous conversion

experiments of C_2H_4 / O_2 and C_3H_6 / O_2 are examined for different oxygen (O_2) concentration and the characteristics of their conversions are discussed. Surface species experiments are examined for the same conditions and detected surface adsorbed species are discussed. From the surface species measurements and facts from the recent DFT studies, the detailed surface reaction mechanism is constructed, and kinetic parameters are fitted by using gaseous conversion experiments and fixed to be thermodynamically consistent. Lastly, additional gas phase experimental results including multiple gas components are used to validate the versatility of the proposed reaction mechanism and to discuss the conversion of the included gaseous components. In Fig. 1.6, the concept used to develop the detailed surface reaction mechanism of C_2H_4 / C_3H_6 is illustrated.

1.4   Organization of Thesis

The thesis is organized as follows,

In Chapter 2, experimental studies used in this study are presented. Experimental methods, to investigate the reaction characteristics of exhaust hydrocarbon species and surface species adsorbed on the platinum group metal, are discussed with the types of catalysts used in this study. Experimental apparatus, setup and conditions are presented, and then the experimental results are discussed.

In Chapter 3, construction of the reaction steps of the detailed surface reaction mechanism for C_2H_4 and C_3H_6 over Pt/Al_2O_3 are presented. Based on the observed facts from the experimental results of gas phase and surface species measurements, and based on the literature studies, considerations for the reaction steps of the detailed surface reaction mechanisms are discussed.

In Chapter 4, numerical modelling method used in this study is presented. Fundamental considerations essential to include in the numerical modelling study of heterogenous catalytic reactions are presented. Monolith honeycomb catalytic converter model together with equations and thermodynamic consistency method used in this study are discussed.

In Chapter 5, numerical studies carried out in this study are presented. Systematic development of surface reaction mechanism is presented and discussed. Numerically simulated results by using numerical method and proposed developed surface reaction mechanism are discussed and validation of the versatility of the developed surface reaction method is discussed.

In Chapter 6, conclusions and suggestions for future work are presented.
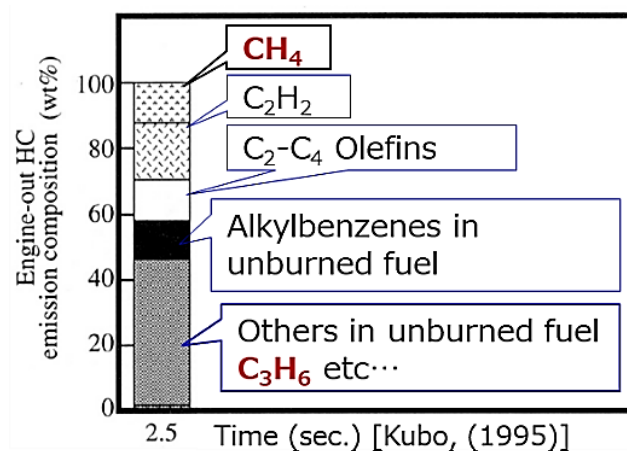
Fig. 1.5   Types of hydrocarbon emissions in the cold start period
(Image from formation and emission characteristics of unburned hydrocarbons
during cold start of a spark-ignited engine system, Kubo 1995)
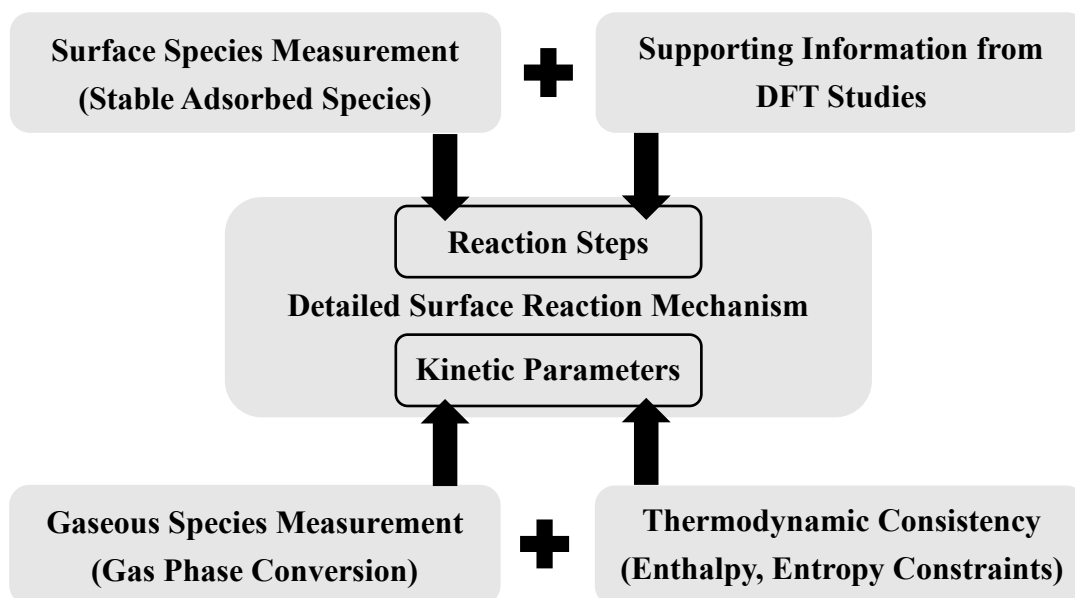
Fig. 1.6   Concept used to develop the detailed surface reaction mechanism

Chapter 2

Experimental Studies

2.1 Introduction

In this study, monometallic catalyst of Pt impregnated on γ-alumina washcoat is used in two forms. One is the monolith honeycomb catalyst used in the practical automotive cars for the gas phase conversion rate experiments. The other one is the powdered catalyst, which is the fragment of monolith washcoat for characterization. Gas phase conversion rate experiments are measured by using Fourier Transform Infrared (FT-IR) equipment and gas analyzers. Surface species experiments are measured by using *in-situ* FT-IR equipment. The physical parameters of catalyst such as metal dispersions, washcoat pore diameters and so on are identified with powdered catalyst, and furthermore, coverage of surface species in various adsorption regimes are examined by *in-situ* FT-IR under the same conditions of inlet gas temperature and compositions as monolith honeycomb experiments. Both of gaseous species conversion experimental results and surface species coverage measurements are used to validate the surface reaction mechanisms. Catalyst preparation, experimental setups and conditions are described in the following sections.

2.2 Catalyst preparation

Monometallic catalyst of Pt is prepared by impregnation of an aqueous solution of $Pt(NH_3)_2(NO_2)_2$ followed by drying and calcination at 500 °C for 2 hours in air. Monolithic honeycomb catalyst is prepared by dipping a cordierite honeycomb (600 cell / in^2) into a slurry, which is prepared by ball-milling of the powder catalyst, an inorganic binder (Al_2O_3, 250 nm in diameter), and water, followed by drying and calcination in air at 450 °C for 1.5 hours.
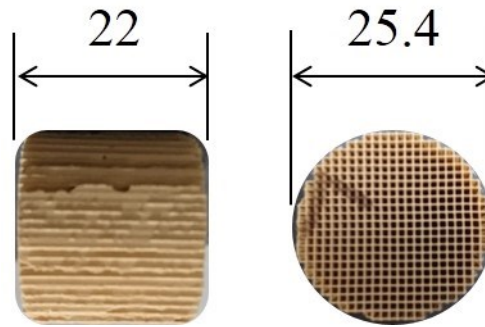
Fig. 2.1   Monolith honeycomb catalyst (units in mm)

Table 2.1   Details of monolith honeycomb catalyst

Catalyst Metal	Pt	
Support Material	Al_2O_3	
Metal Dispersion	66.4	%
Thickness of substrate wall δ_{wall}	0.09	mm
Repeat distance of the monolith s	1.04	mm
Cell density	600	cells/inch^2
Density of substrate	1741.1	kg/m^3
Thickness of washcoat δ_{wcl}	0.057	mm
Pore diameter d_{pore} [*1]	13.907	nm
Mean pore volume [*1]	0.955×10^{-3}	m^3/kg
Density of washcoat	1836.31	kg/m^3
Porosity of washcoat ε_{wcl}	0.590	
Thermal conductivity of		
Substrate and washcoat	4.00	W/mK
Insulator	0.06	W/mK
Quartz reactor	1.38	W/mK

*1   Measured with nitrogen porosimetry
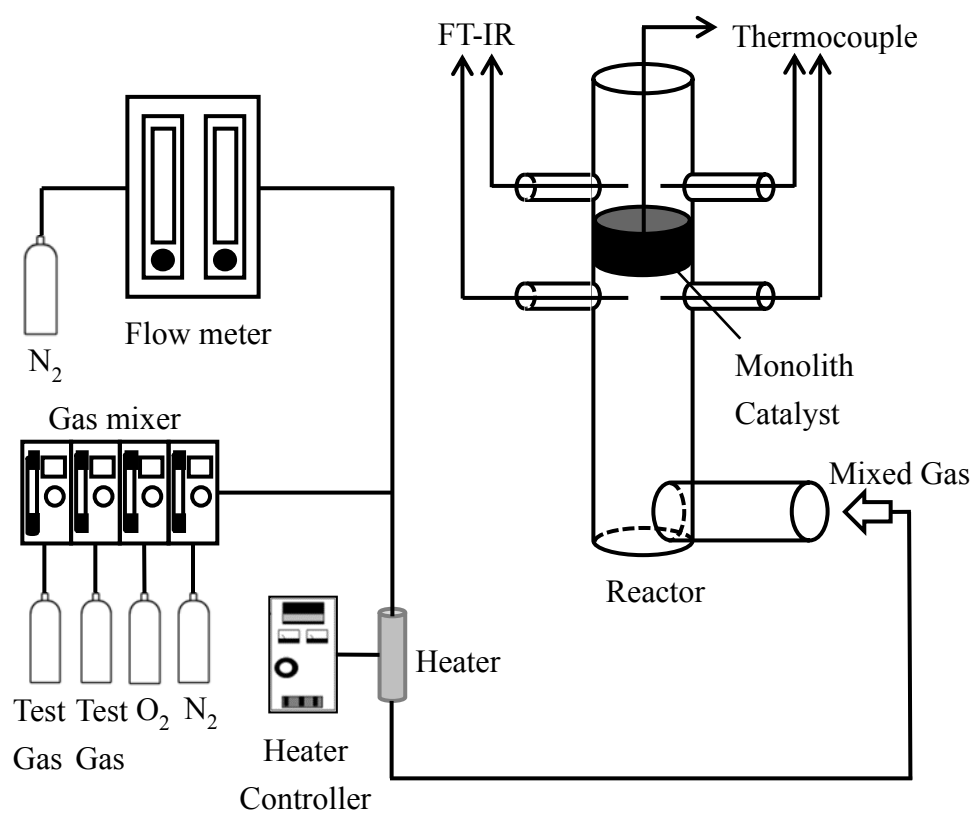
Fig. 2.2   Schematic of experimental setup
(Gas phase conversion rate experiments with monolith honeycomb reactor)
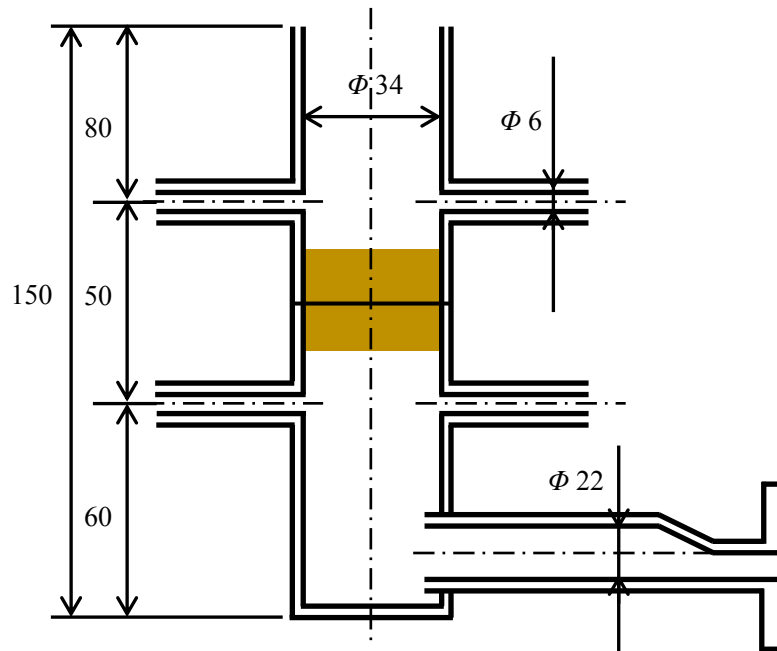
Fig. 2.3   Schematic of the monolith honeycomb reactor
(Monolith honeycomb catalyst fixed inside the reactor and shown as colored part,
units in mm)

Gas flow
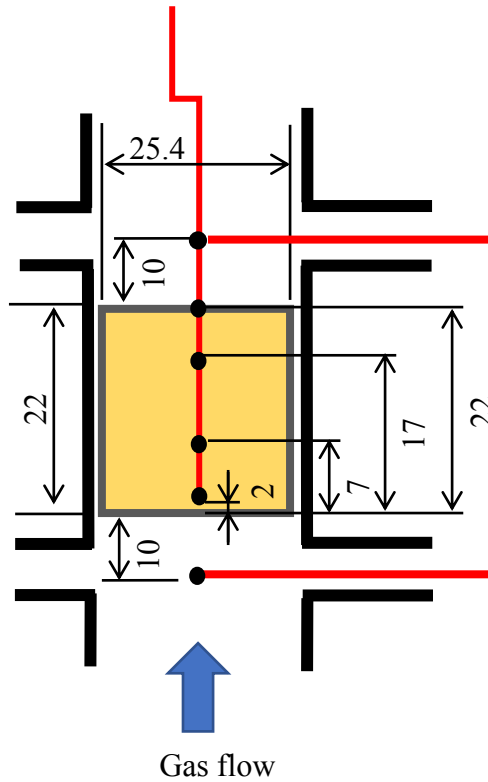
Fig. 2.4   Schematic diagram of the temperature measuring points (units in mm)

2.3   Gas phase conversion experimental setup and apparatus

In the gas phase conversion experiments, monolith honeycomb catalyst and reactor are used.   The monolith honeycomb catalyst used in this study is shown in Fig. 2.1 and reactor is shown in Fig. 2.2 and Fig. 2.3, and details of monolith honeycomb catalyst are shown in Table 2.1.

The monolith honeycomb catalyst contains a platinum γ-alumina washcoat of 1 mm thickness which is supported on a cordierite monolith with a cell density of 600 cpsi and the metal loading of 0.8 g/L and 66.4 % metal dispersion.   It is thermally treated in advance at 500 °C for 3 hrs.   Figure 2.2 illustrates the experimental set up of gas phase conversion experiments.   In the experimental setup, there are flow meters, gas mixers, heater, heater controller, gas flow switching devices, quartz tube reactor, thermocouples, FT-IR equipment and gas analyzers.   Types of the components, structure and functions of devices in the experimental setup are demonstrated in the following sub-sections.

2.3.1   Quartz tube reactor

The monolith catalyst of 25.4 mm in outer diameter and 22 mm in length is fixed inside the quartz tube reactor.   The outer side of monolith catalyst is wrapped with heat insulator, and the outside of quartz reactor is covered by the glass wool to reduce the heat loss to surrounding.   Figure 2.3 shows the illustration together with the schematic of the monolith honeycomb catalyst fixed inside the quartz tube reactor.   The quartz tube reactor is 34 mm in diameter, and 150 mm in length.   It is fabricated with quartz channels before and after the catalyst to be able to measure the gas compositions and temperatures.

2.3.2   Flow meters and gas mixers

Nitrogen gas balanced test gas mixture is supplied from standard gas cylinders and flow rates of gases are separately measured and mixed by gas mixers (Front Corp., LogMIX).   Test gas mixture is preheated by the gas heater (Nihon heater, QA-3KW) in the line, and supplied to the reactor.   Nitrogen gas is used to preheat the catalyst before the test gas mixture and flow rate of it is monitored by an AP - 0250 U area flow meter made by Showa Instrumentation Co., Ltd.   The total gas flow rate is fixed at 20 L/min resulting in the space velocity of 100000 h^{-1} and pressure at 1 bar.

2.3.3 Gas flow switching devices

Preheating the catalyst with nitrogen gas process, surface cleaning process (which is described in the experimental procedure section) and testing with test gas mixture process are controlled and monitored by using electronic gas flow switching devices. Switching devices help to prevent the gases from mixing during each process so that the experiments can proceed without errors. Timings of the gas flow switching are described in the experimental procedure section.

2.3.4 Heater and heater controller

Preheating the catalyst and test gas mixture is done by using a high-temperature gas heater (QA 200 V 3 KW) made by Nippon Heater, and the range of the heater is from room temperature to 600 °C. Temperature for the gas heater is controlled by using a heater controller manufactured by Rika Kogyo Co. Gas heater is installed immediately before the reactor so that the outlet gas temperature from the gas heater is the set value of the experimental temperature. In addition, heat insulation is applied to the supply line to prevent heat loss in it.

2.3.5 Thermocouples

Temperature measurements are done by using K-type sheathed thermocouple of 250 μm outer diameter. Temperature is measured at each point before and after the catalyst and at 4 points inside the catalyst. Figure 2.4 shows the temperature measuring points, and red solid lines represent thermocouple and light-yellow section represent the catalyst). The temperature measured can be monitored together with the gas concentration in the FT-IR.

2.3.6   FT-IR and gas analyzers

Gas species concentrations are measured by Fourier Transform Infrared (FT-IR) spectroscopy, and the exhaust gas analyzer named Bex-2200FT, manufactured by Best Instruments Co., Ltd., which consists of FT-IR spectrometer, O_2 gas analyzer and H_2 gas analyzer is used.   This instrument can measure two lines which are in inlet and outlet gas positions at the same time.   It can measure target gas components as time series data. Types of gas species that can be measured by Bex-2200FT is shown in Table 2.2. Infrared spectroscopy is well known for its promising application to exhaust gas analysis (Twiss et al., 1955).   Since the Fourier Transform Infrared (FT-IR) is used for gas and surface species experiments, it is important to know briefly about its principles.

FT-IR spectrometer detect the band of the specific species that measure same as the classical spectrometer.   The difference lay on the usage of interferometer.   In classical spectrometer, the beam from the source hit the prism or monochromator and separated.   The separated beams, with different wavelengths, then separated again in two by beam splitter.   One goes to sample and other go as reference.   In the end, they will be detected by the detector and send the analog signal as record energy with a function of wavelength.   In the FT-IR, the use of monochromator is replaced by interferometer.   In general, the original design of the interferometer (Michelson Interferometer) is still in use and it consists of beam splitter, stationary mirror and moving mirror, as shown in Fig. 2.5.

In the interferometer, the beam is split into two by the beam splitter.   One goes to stationary mirror and one goes to moving mirror.   Those both separated beams will be reunited again but with the difference path lengths.   This beam is called interferogram. The interferogram then goes to species or sample.   The species will absorb or subtracts their specific wavelengths.   The specific wavelengths will be detected by detector as an energy diagram and the diagram is then processed with Fourier transformation simultaneously.   Fourier transform is performed for every point in the interferogram to get the intensity of the infrared spectrum.

Most of the state-of-the-art FT-IR spectrometers are built in with computational assistance.   Calculation is performed by FT-IR software and the results will be given in a view seconds time.   Source of beam used is infrared beam and a frequency range of infrared wavelength is absorbed by most of the organic molecules, and the absorption spectrum is correlated with the chemical bonds of the molecules.

FT-IR is generally a single beam measurement.   Therefore, the transmission spectrum of the sample is obtained from two measurements, one with the sample in the sample chamber and the other without the sample (background).   The transmission

spectrum, which is the ratio of the sample to the background, directly shows the compounds or molecules in the sample.   The transmission spectrum is calculated by the following expression.

$$Transmission\ spectrum = \frac{Sample\ single\ beam}{Background\ single\ beam} \times 100 \qquad (2.1)$$

Furthermore, by using computer calculation, the spectrum value can be converted as concentration value of each species detected and displayed as real time values in the FT-IR software.   General components consisting in a FT-IR spectrometer are shown in Fig. 2.6.

Oxygen gas analyzer incorporated in the Bex - 2200 FT is a magnetic type, and in this type, oxygen concentration is continuously obtained by utilizing the attraction force generated when the large paramagnetic oxygen molecules are magnetized in the magnetic field.   The analyzer consists of a sampling unit, where containers filled with nitrogen are equipped within a strong magnetic field.   When oxygen containing sample gas flows through the sampling unit, oxygen is attracted to the magnetic fields, resulting a displacement on the containers.   The displacement, which is proportional to the oxygen concentration, is measured and converted to an oxygen concentration with computational assistance.

Hydrogen gas analyzer used in this study is a total mass spectrometer for hydrogen and helium.   Measurement is based on a magnetic field deflection mass spectrometry (SF-MS, single-focusing mass spectrometry).   Sample ions generated by the electron ion source are accelerated, converged and further separated at a constant energy in the magnetic field, and a mass range of 2 to 4 amu is detected with a response time of less than 1 second.   In principle, it is practically impossible to directly measure by using gravity because mass of the atoms and molecules are very small, therefore, it is measured by using electromagnetic force.   To utilize electromagnetic force, it is necessary to first charge (ionize) atoms or molecules.   Next, when the generated ions are moved in an electromagnetic field, since there is a difference in motion depending on the mass of the ions (the ratio of the mass and the charge number), the difference is used to separate the ions.   By detecting the separated ions, the mass and number of ions can be measured.   The produced mass spectrum is then processed to a gas concentration with computational assistance.

Table 2.2   Measurable gas species by Bex-2200 FT

Carbon monoxide	CO
Carbon dioxide	CO_2
Water vapor	H_2O
Sulphur dioxide	SO_2
Nitric oxide	NO
Nitrogen dioxide	NO_2
Nitrous oxide	N_2O
Ammonia	NH_3
Methane	CH_4
Acetylene	C_2H_2
Ethylene	C_2H_4
Ethane	C_2H_6
1,2-Propadiene	C_3H_4
Propylene	C_3H_6
Propane	C_3H_8
1,3-Butadiene	$1\text{-}3,C_4H_6$
Normal butane	$n\text{-}C_4H_{10}$
Normal pentane	n-C5H12
Isopentane	$iso\text{-}C_5H_{12}$
Normal hexane	$n\text{-}C_6H_{14}$
Normal octane	$iso\text{-}C_8H_{18}$
Benzene	C_6H_6
Toluene	C_7H_8
Acetaldehyde	CH_3CHO
Formaldehyde	HCHO
Ethanol	C_2H_5OH
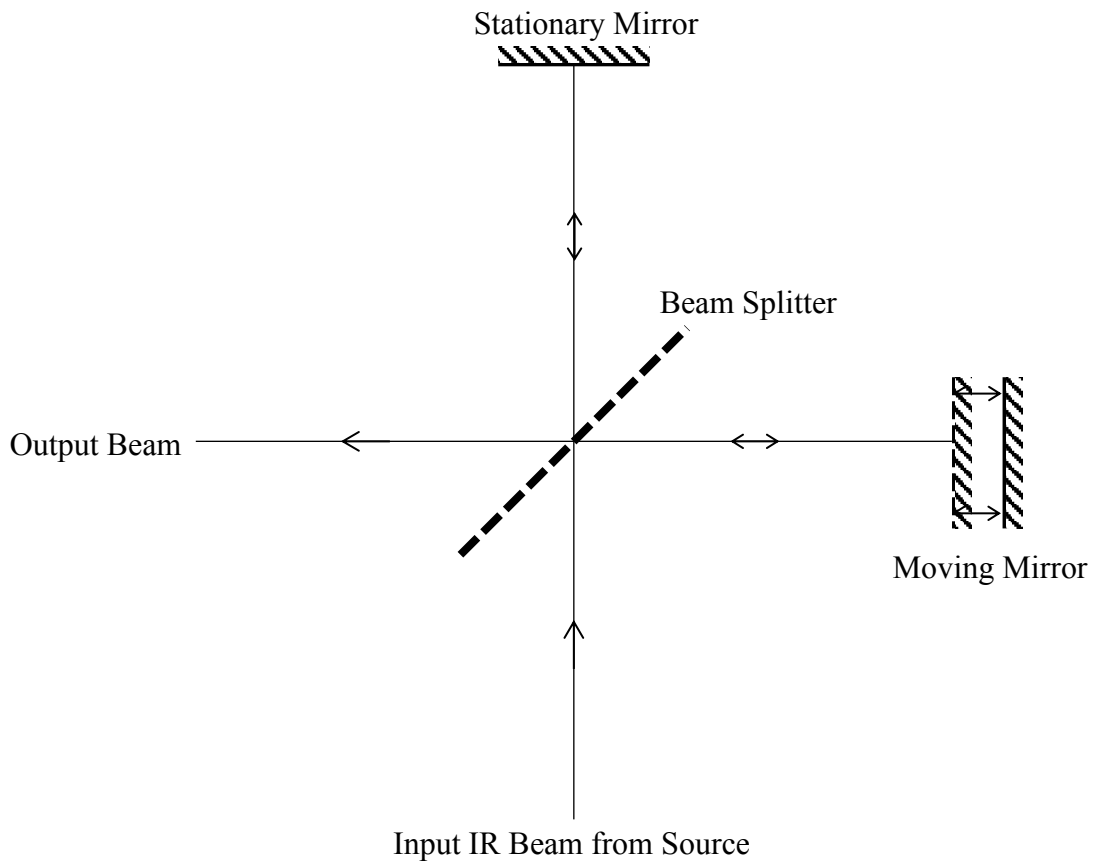
Fig. 2.5   Schematic diagram of an original Michelson interferometer
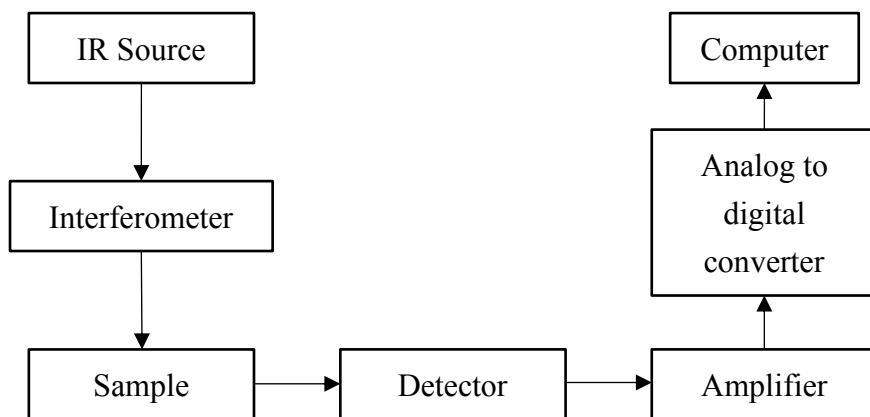
Fig. 2.6   Block diagram of the components of a FT-IR spectrometer

2.3.7   Experimental procedure

Gaseous species are sampled at the upstream and downstream of the catalyst and the composition is identified by the FT-IR.   Temperature at the upstream and downstream of catalyst are also measured simultaneously.   Nitrogen gas balanced test gas mixture is supplied from standard gas cylinders and flow rates of gases are separately measured and mixed by gas mixer.   The mixture is heated by the gas heater in the line and supplied to the reactor.

Figure 2.7 shows the experimental procedure at each experimental point. Horizontal axis is the time history and vertical axis is the gas concentration.   Total gas flow rate for each process is kept constant at 20 L/min.   Catalyst is preheated by the nitrogen gas until it reaches the experimental temperature.   Test gas temperature and temperature inside the catalyst are carefully monitored to be at the experimental temperature.   Then the surface of the catalyst is cleaned by using carbon monoxide gas for 1 minutes to eliminate any residual surface oxygen from the surface, and then the test gas is issued for the conversion measurement.   Between the surface cleaning process and test gas measuring process, nitrogen gas is issued for 15 seconds to make sure that the surface cleaning gas and the test gas mixture are not mixed inside the supply line. During the gas phase conversion measurement process, gas concentrations and temperatures are logged by a computer as time series data and experiment is stopped when the stable conversion of the test gas mixture is achieved, usually the stable conversion is reached at about 5 minutes.   All of the gas flow switching processes are carefully monitored by the gas flow switching devices.

2.4   Experimental conditions

Gas phase conversion experiments are conducted mainly for C_2H_4 / O_2 and C_3H_6 / O_2 system to construct the surface reaction mechanisms of ethylene and propylene, and additional experiments are also conducted for CH_4, C_2H_6, C_3H_8, and C_7H_8 to compare their reactivity.   As for the main target of C_2H_4 and C_3H_6, experimental conditions are indicated in Table 2.3 and 2.4.   First, C_2H_4 / O_2 and C_3H_6 / O_2 mixtures are simply examined (Table 2.3) and then, C_2H_4 / C_3H_6 / CO / O_2 mixtures are investigated (Table 2.4) to validate the surface reaction mechanism.   On the experiments (in Table 2.3), to maintain the heat release of mixture, HC concentration is changed for each HC, i.e., 500 ppm for C_2H_4, 333 ppm for C_3H_6, and fixed through the experiments.

Here, Φ is defined as the equivalence ratio, which is the ratio of the fuel-to-

oxidizer ratio to the stoichiometric fuel-to-oxidizer ratio, and it is varied by changing the oxygen concentration under the fixed concentration of HCs.   In this study, oxygen concentration is fixed as 1500 ppm for stoichiometric condition (in Table 2.3), 3000 ppm, 10000 ppm for fuel lean (oxygen excess) conditions (in Table 2.3), and 1000 ppm for fuel rich condition (in Table 2.3).   On the validation process of surface reaction mechanism, conversions of several mixtures of C_2H_4 / C_3H_6 / CO / O_2 are examined as shown in Table 2.4 and the stoichiometric and fuel lean (oxygen excess) conditions are treated in the same way.

As for the other HCs (CH_4, C_2H_6, C_3H_8, C_7H_8), experiments are conducted just to confirm the relative importance of C_2H_4 and C_3H_6 among typical component of unburned HCs emitted from the internal combustion engines.   Gas phase conversion rates are examined under stoichiometric condition with 1500 ppm O_2.   Each HC concentration is 750 ppm for CH_4, 428 ppm for C_2H_6, 300 ppm for C_3H_8, and 167 ppm for C_7H_8 to maintain the heat release of mixture.   For toluene (C_7H_8), liquid is bubbled by small amount of preheated nitrogen (70 °C) fed from the bottom of liquid tank, and obtained HC / N_2 mixture is further mixed with O_2 and N_2 to control the mixture composition before the gas heater ("Heater" in Fig. 2.2).   For every experiment, HC concentration is monitored at the upstream of reactor by FT-IR.

The conversion experiments are conducted by ramping up from low temperature to high temperature to investigate the light-off nature of test gas mixture.   Results of gaseous conversion experiments are shown as the conversion rate (CR) defined by following equation,

$$CR = \frac{[X]_{upstream} - [X]_{downstream}}{[X]_{upstream}} \qquad (2.2)$$

where $[X]_{upstream}$ and $[X]_{downstream}$ are respective test gas concentrations at the upstream and downstream of monolith catalyst.   CR is calculated after $[X]_{downstream}$ is attained steady state, which is within 5 minutes for all experimental conditions.

Table 2.3　Experimental inlet gas conditions before the catalyst for the construction of proposed surface reaction mechanism

Case	Condition	C_2H_4[ppm]	C_3H_6[ppm]	O_2[ppm]	Φ [-]
I	Stoichiometric	500	-	1500	1.00
II	Fuel Lean (O_2 excess)	500	-	3000	0.50
III	Fuel Lean (O_2 excess)	500	-	10000	0.15
IV	Fuel Rich	500	-	1000	1.5
V	Stoichiometric	-	333	1500	1.00
VI	Fuel Lean (O_2 excess)	-	333	3000	0.50
VII	Fuel Lean (O_2 excess)	-	333	10000	0.15
VIII	Fuel Rich	-	333	1000	1.5

Table 2.4　Experimental inlet gas conditions before the catalyst for the validation of proposed surface reaction mechanism

Case	Condition	C_2H_4[ppm]	C_3H_6[ppm]	CO[ppm]	O_2[ppm]	Φ [-]
IX	Stoichiometric	200	-	5000	3100	1.00
X	Stoichiometric	-	111	5000	3000	1.00
XI	Stoichiometric	200	100	5000	3550	1.00
XII	Fuel Lean (O_2 excess)	200	100	5000	6000	0.60
XIII	Fuel Lean (O_2 excess)	200	100	5000	10000	0.36
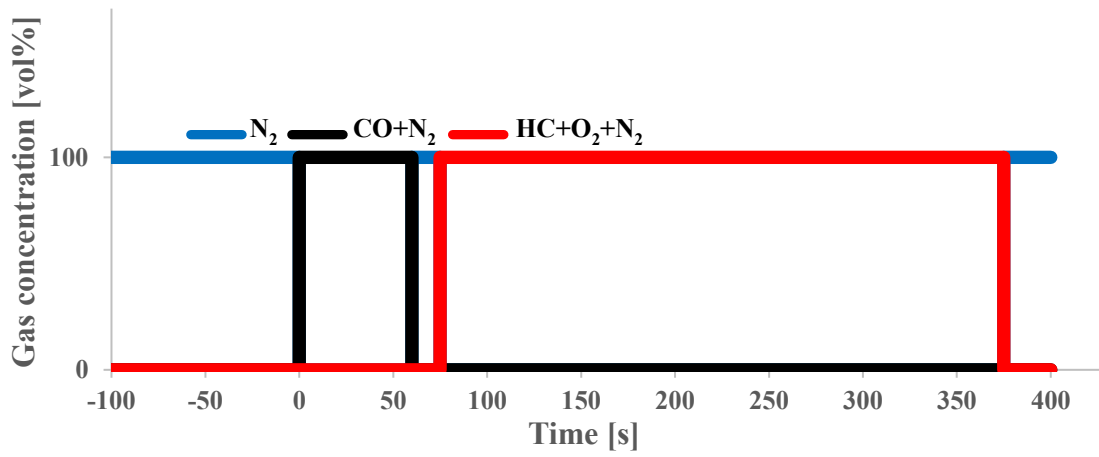
Fig. 2.7 Experimental procedure at each experimental point
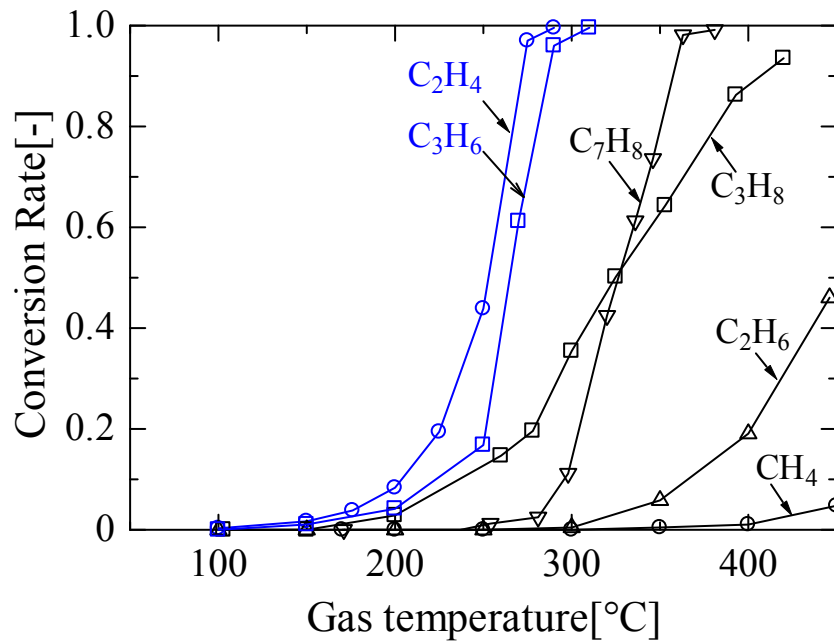
Fig. 2.8 Reactivity of selected HCs on Pt/Al$_2$O$_3$ catalyst

2.5   Gas phase conversion experimental results

2.5.1   Reactivity investigation of HCs on Pt/Al$_2$O$_3$

First, to confirm the relative importance of C$_2$H$_4$ and C$_3$H$_6$ among typical components of unburned HCs emitted from internal combustion engines, gaseous conversions are examined for CH$_4$, C$_2$H$_6$, C$_3$H$_8$, and C$_7$H$_8$ under stoichiometric conditions. Here, for every experimental condition, oxygen concentration is kept at 1500 ppm as constant while HC gas concentrations are adjusted to be stoichiometric accordingly so that the reactivity can be clearly observed.   Figure 2.8 shows the reactivity of the selected HC species.   In this figure, horizontal axis is the gas temperature before catalyst and vertical axis is the conversion rate of HC species.

As for discussion, the term "light-off performance" is used and here, light-off temperature is defined as the temperature at which 0.2 or 20 % of conversion rate is achieved.   It is investigated that for the saturated HCs, light-off performance increase with the increase in carbon number and for the unsaturated HCs, light-off performance decrease with the increase in carbon number.   Here, only the conversion of C$_7$H$_8$ is added for the comparison between the reactivity of HCs on the catalyst used in this study. Other HCs such as C$_2$H$_2$, C$_3$H$_4$ and C$_6$H$_6$ are also investigated experimentally and their results are not included due to the restriction of the information from the collaborative research institution.

To be concluded, it is confirmed that C$_2$H$_4$ has the highest reactivity among them while CH$_4$ has the lowest for the catalyst used in this study.   Similar results were reported by Bart et.al. (Bart et al., 1992) for Pt-Rh/Al$_2$O$_3$-CeO$_2$ catalyst.   According to this result, both C$_2$H$_4$ and C$_3$H$_6$ can be said as important because they show the highest reactivity, and thus, dominate the light-off performance of the unburned HCs in internal combustion engines.

2.5.2   Reaction characteristics investigation of C$_2$H$_4$ and C$_3$H$_6$ on Pt/Al$_2$O$_3$

Figure 2.9 shows the experimental results of the gaseous conversion rate of C$_2$H$_4$ / O$_2$ / N$_2$ (Fig. 2.9 (A)) and C$_3$H$_6$ / O$_2$ / N$_2$ (Fig. 2.9 (B)) for different oxygen concentrations.   Horizontal axis is the gas temperature at the upstream of monolith catalyst and vertical axis is the conversion rate of C$_2$H$_4$ and C$_3$H$_6$.   In Fig. 2.9 (A), result shows that the light-off temperature of C$_2$H$_4$ conversion for stoichiometric conditions (Case I in Table 2.3) is 230 °C and the complete (100 %) conversion is achieved at 290 °C.

With the increase of O_2 concentration ($\Phi = 0.5$ and 0.15, Case II & III in Table 2.3), light-off and complete conversion temperatures are 208 °C and 255 °C for $\Phi = 0.5$, while 160 °C and 200 °C for $\Phi = 0.15$.   The light-off temperature is decreased by 70 K by increasing O_2 concentration from 1500 ppm to 10000 ppm, i.e., light-off performance increases with the increase in oxygen concentration.   When the O_2 concentration is decreased ($\Phi = 1.5$, Case IV in Table 2.3), light-off and maximum conversion temperatures are 250 °C and 350 °C.   Here, it can be noted that only the maximum conversion of 66.667% can be achieved for the rich case ($\Phi = 1.5$) due to the lack of O_2 for complete conversion.

C_3H_6 shows similar tendency with C_2H_4, as shown in Fig. 2.9 (B).   Under the stoichiometric condition ($\Phi = 1.0$), the light-off temperature is 250 °C and 100 % conversion can be attained at 310 °C, which is about 20 K higher than C_2H_4.   In the fuel lean conditions of $\Phi = 0.5$ and 0.15 (Case VI & VII in Table 2.3), the corresponding light-off and 100 % conversion temperatures are 215 °C and 280 °C for $\Phi = 0.5$ while 197 °C and at 230 °C for $\Phi = 0.15$.   Light-off temperature is confirmed to be decreased about 50 K by increasing O_2 concentration.   In the fuel rich condition, $\Phi = 1.5$ (Case VIII in Table 2.3), the corresponding light-off and maximum conversion temperatures are 295 °C and 400 °C.   Light-off performance of C_3H_6 as well as C_2H_4 is found to increase with the increase in oxygen concentration.

In both cases, i.e., C_2H_4 / O_2 / N_2 and C_3H_6 / O_2 / N_2, complete or optimal conversion ranges become narrower with the increase in oxygen concentration. Oxidation processes become sharper and the presence of higher concentration or partial pressure of oxygen make the rate of reactions faster.   Previous studies reported the same fact for Pt catalyst (Burch and Watling, 1997; Captain et al., 1998; Gervasini et al., 1999; Liu et al., 2006; Shen and Kawi, 2001), and even in the presence of NO, unsaturated double bonds of C_2H_4 and C_3H_6 make their combustion higher with the increase in oxygen concentration.   Presence of surface oxygen species on the catalyst promote the decomposition of C_2H_4 and C_3H_6 and this fact is considered in the construction of surface reaction mechanism.   Moreover, other types of HCs that can be measured by the FT-IR used in this study are monitored during the experiments whether they have any or significant concentration from the oxidation of C_2H_4 and C_3H_6 to be included in the surface reaction mechanism.
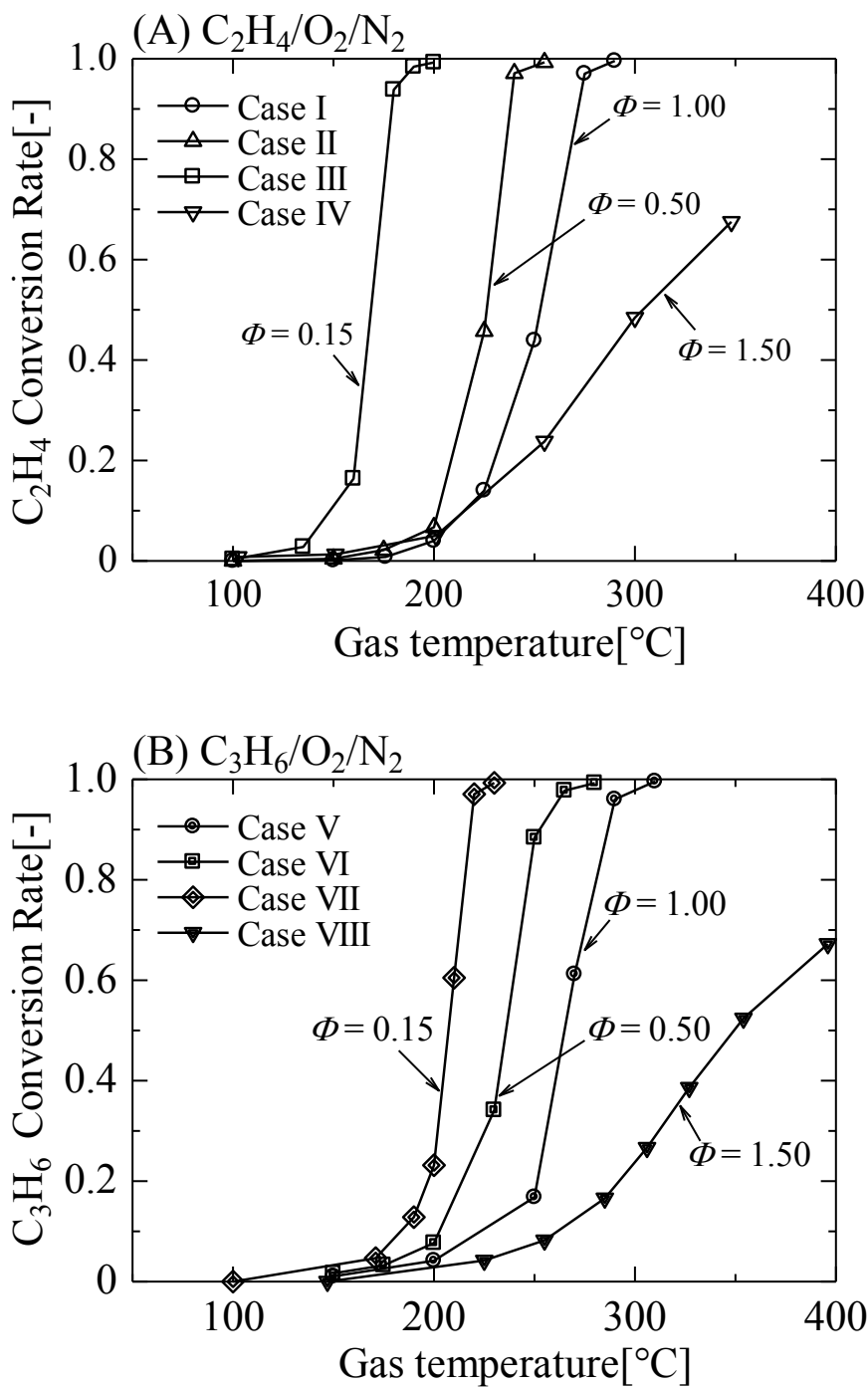
Fig. 2.9   Conversion rate for various O_2 concentrations (A) C_2H_4 (B) C_3H_6

2.6   Surface species experiments

Variations of the adsorbed surface species on the sample catalyst are identified by using *in-situ* FT-IR.   In these measurements, diffuse reflection spectra, which is the spectra measured in transmission then converted to absorbance with computational assistance, is used instead of the transmission spectrum itself.   It is a promising method to investigate the adsorbed surface species on the powdered material (Lindon, 2010). The spectral information (peak position, peak value and their variation with temperature) provide information about the adsorbed species, adsorption regime and qualitative variations of their coverage (Hinokuma et al., 2016; Satsuma and Shimizu, 2003).   *In-situ* FT-IR spectra of the chemisorbed substrate on each catalyst are acquired by a FT-IR-6600 (Jasco) and the schematic diagram of the experimental setup is as shown in Fig. 2.10.   The samples are prepared by scraping the washcoat of monolith honeycomb catalyst and grinding them.   On this measurement, a temperature-controllable diffuse reflectance reaction cell and a mercury cadmium telluride (MCT) detector are used.   The cell is heated to 300 °C for 30 min, and then, the background spectra at each temperature (50~300 °C) are collected after cooling to the room temperature.   Then, the powdered catalyst is then exposed to the test gas stream under various temperature conditions for over 5 minutes before its spectrum is collected.

In-situ experiments are conducted under the same conditions (space velocity, temperatures and compositions) as honeycomb monolith reactor except for the balance gas.   Here, it should be noted that quantitative measurement of surface species is possible with *in-situ* FT-IR for some cases, however, the catalyst is in "powdered" form as described above.   Because our main target is the modelling of "monolith honeycomb catalyst", quantitative information from powdered catalyst cannot be (or must not be) directly used for the modelling of monolith honeycomb catalyst.   Then, in this study, only qualitative information of surface species is used for the development of the surface reaction mechanism.   Helium is used as balance gas to control the system temperature precisely, besides nitrogen is used in monolith honeycomb experiments considering the practical exhaust gas component.   It is confirmed that effects of the inert gas on the surface reaction seems negligible by our preliminary experiments of monolith honeycomb reactor using both of helium and nitrogen as balanced gas.

It is found in our work (Shimokuri et al., 2020) that (1) the gaseous temperature and catalyst wall temperature is different in the monolith honeycomb reactor, and (2) the monolith wall temperature is almost uniform along the flow direction in all experimental conditions (±5 K).   Then, the obtained *in-situ* FT-IR spectra for each temperature

condition is treated as the surface species information based on the wall temperature of monolith honeycomb catalyst.

2.7   Surface species experimental results

Surface experimental results are presented by processing the raw measurements. Background spectrum at the experimental temperature is eliminated from the experimental test gas spectrum at the same temperature, and an example of it is shown in Fig. 2.11.   In Fig. 2.11, horizontal axis is the wavenumber and vertical axis is the absorbance, and the spectra are measured at 200 °C.   Balanced gas spectrum, here Ar spectrum, test gas spectrum and the difference spectrum of these spectra are included in Fig. 2.11, and the difference spectrum at each experimental temperature is presented as surface species experimental result.

Figure 2.12 to Fig. 2.17 show the experimental results of surface species measurements for experimental conditions shown in Table 2.3 obtained by *in-situ* FT-IR in which the adsorption intensities of each surface species for various temperature conditions are shown.   The adsorbed species are identified based on the literature (Bazin et al. 2005; Bamwenda *et al.*, 1995; Captain and Amiridis, 1999; Chauvin et al. 1990; Ermini et al., 2000; Finocchio et al. 1999; Haneda et al. 2015; Matsouka et al., 2008; Schießer et al. 2001).   In the figures from Fig. 2.12 to Fig. 2.17, horizontal axis is the wavenumber and vertical axis is the absorbance, which is the converted measured spectra after the elimination of background spectra.   In these figures, species detected below the wavenumber of 2000 cm^{-1} are assigned as species adsorbed on the support material, Al_2O_3, and above the wavenumber of 2000 cm^{-1} are assigned as species adsorbed on the metal, Pt.

Here, on the support material, it can be noted that different peaks from around 1300 cm^{-1} to around 1650 cm^{-1} are detected.   Band assignments for these species are acetone species at 1538 cm^{-1} and 1650 cm^{-1}, and carboxylate species such as formates and acetates at 1305 cm^{-1}, 1380 cm^{-1}, 1460 cm^{-1} and 1580 cm^{-1}.   In all experimental conditions, intensities of the detected species increase with the increase in temperature and oxygen concentrations so that the stable existence of these species can be confirmed.

On the metal, Pt, the spectra around 2350 cm^{-1} came from gaseous CO_2.   The absorption band of hydrocarbon fragments, HC species, is supposed to be detected at 2910 cm^{-1}, however, only peak with weak intensity is observed.   Here, HC peak on *in-situ* FT-IR (at 2910 cm^{-1}) is known to be intrinsically lower than other peaks (Zaki et al., 2001).   The peak can be increased by increasing metal loading or measurement time

(Beebe et al., 1985; Wang and Yates, 1984), however, those ways seem not adequate because (1) light-off behavior cannot be clearly observed with higher metal loading due to the excessive reactivity and (2) metal surface condition can be changed as it is exposed to the reactive gas long time. Then, in this study, despite the weak intensity, the fact of the existence of CH_x intermediate species is considered to include in the construction of the surface reaction mechanism.

The observed peaks at 2090 cm^{-1} and 2015 cm^{-1} are CO species adsorbed linearly on the Pt. Here, the peak at 2090 cm^{-1} represent the presence of linearly adsorbed CO on the large Pt particles, while 2015 cm^{-1} represent on the small Pt particles. Experiments to examine the Pt particle size and detailed parameters for the catalyst used in this study are conducted by CO pulse method and nitrogen porosimetry (Table 2.1). It is confirmed that the average particle size of the catalyst is about 1.7 nm with 66.4 % dispersion revealing that the presence of small Pt particles with high dispersion. Bazin et.al. (Bazin et al. 2005) found that the peak at 2090 cm^{-1} can be observed mostly for large Pt particles (*ca.* 4 nm) with poor dispersion and they concluded that the peak comes from the local platinum oxidation at the metal-support interface. Therefore, only the observed peak for small Pt particles at 2015 cm^{-1} is considered in the surface reaction mechanism construction process.

Here, it can be noted that the intensities of the intermediate HC species show only weak peaks despite the fact that the intensities from gaseous CO_2 and linearly adsorbed CO on the small Pt particles show significant peaks compared to them. This fact also reflects the fast reaction rate of the HC intermediate species after their adsorption on the Pt surface. Moreover, gaseous CO_2 intensities increase higher than those of linearly adsorbed surface CO on the small Pt particles with the increase in temperature and oxygen concentrations. This fact reflects that there is early formation of CO_2 during the oxidation process and it comes from the early C-C bond cracking and not from the oxidation of surface CO which is formed by the skeletal decomposition of HC species. The facts mentioned before and the qualitative tendencies of the adsorbed CO peak with temperature are considered on the development of surface reaction mechanism. Surface experiments are also conducted for fuel rich cases, but the results are not shown because the gas compositions are different from Table 2.3 and it is confirmed that the results also show the same tendency as the surface experimental results shown.
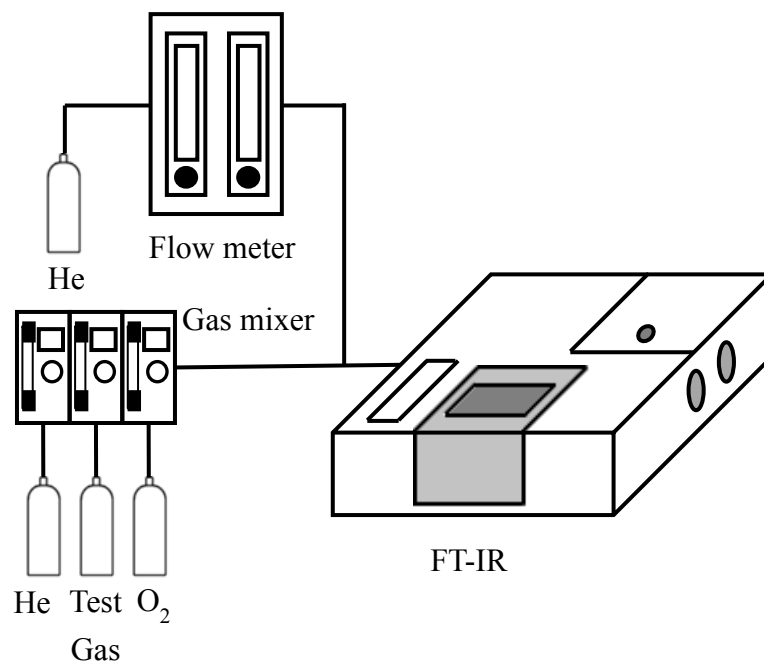
Fig. 2.10   Schematic of experimental setup for surface species measurements
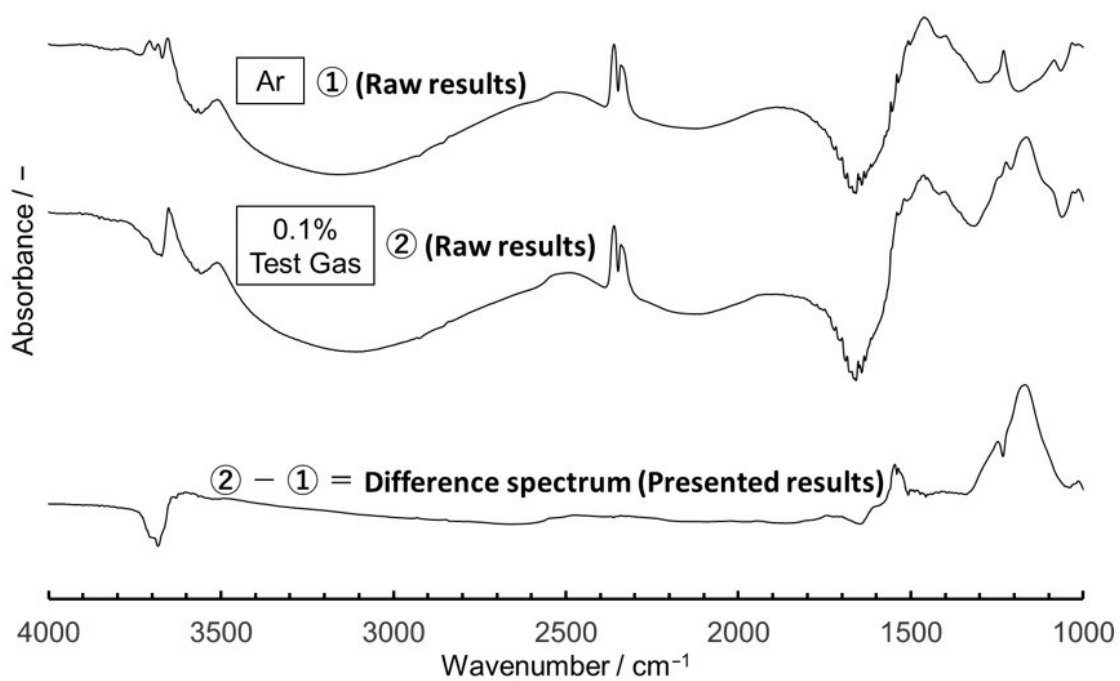
Fig. 2.11   Example of raw surface experimental results and presented surface
experimental results
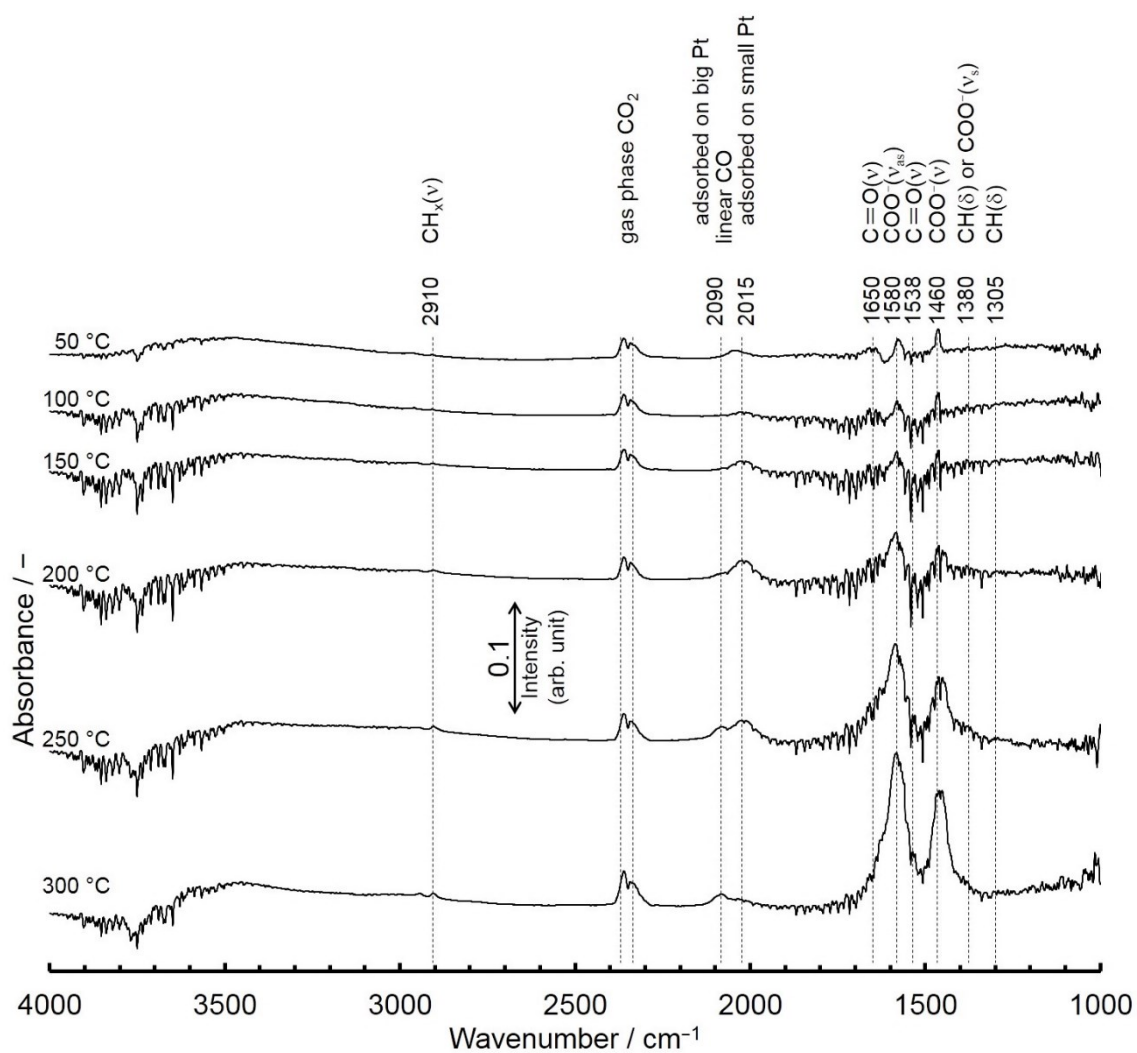
Fig. 2.12   *In situ* FT-IR spectra of C_2H_4 and O_2 adsorbed on Pt/Al_2O_3.
(Spectra are measured in gas feeds of 500 ppm C_2H_4, 1500 ppm O_2 and He balance)
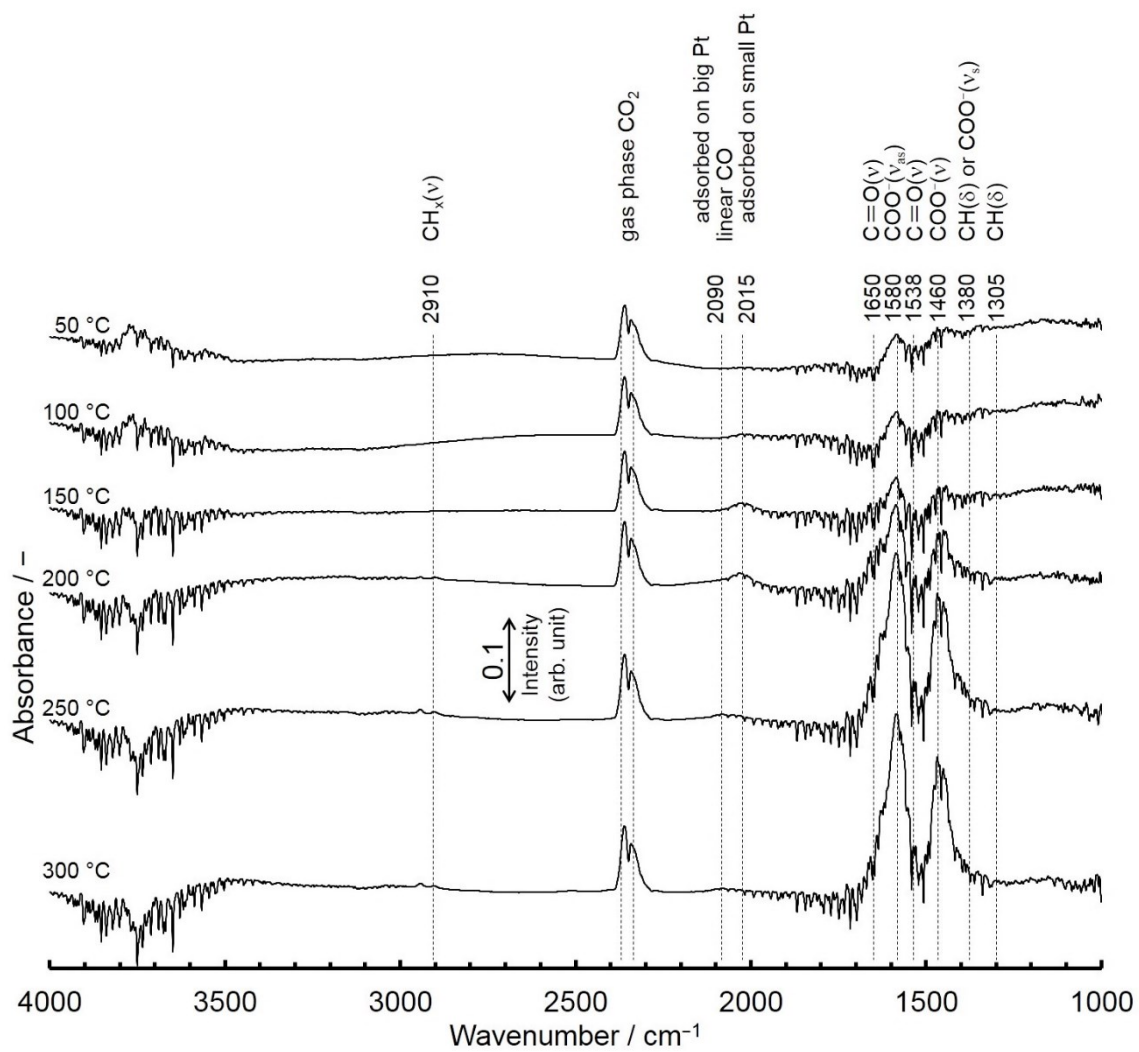
Fig. 2.13   *In situ* FT-IR spectra of C_2H_4 and O_2 adsorbed on Pt/Al_2O_3.
(Spectra are measured in gas feeds of 500 ppm C_2H_4, 3000 ppm O_2 and He balance)
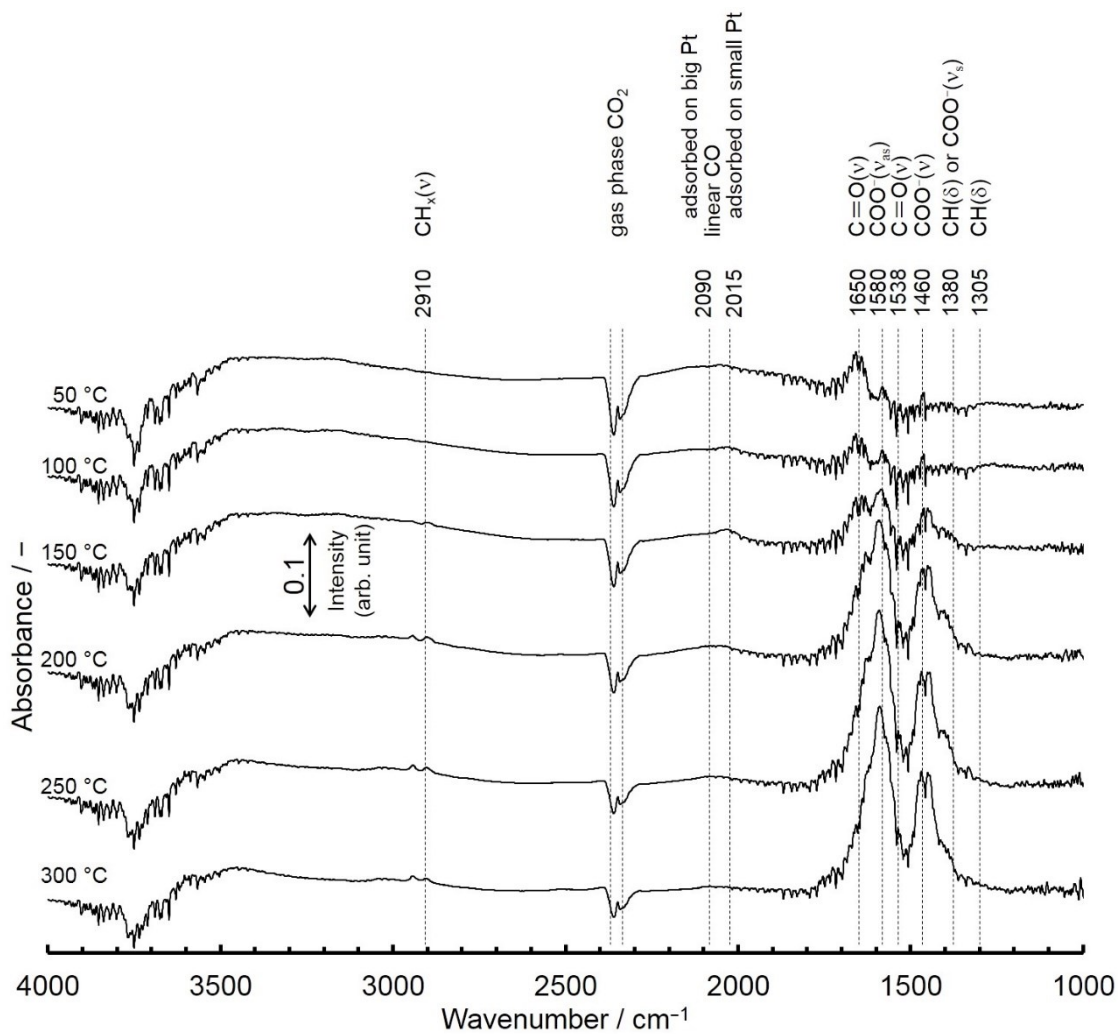
Fig. 2.14   *In situ* FT-IR spectra of C_2H_4 and O_2 adsorbed on Pt/Al_2O_3.
(Spectra are measured in gas feeds of 500 ppm C_2H_4, 10000 ppm O_2 and He balance)
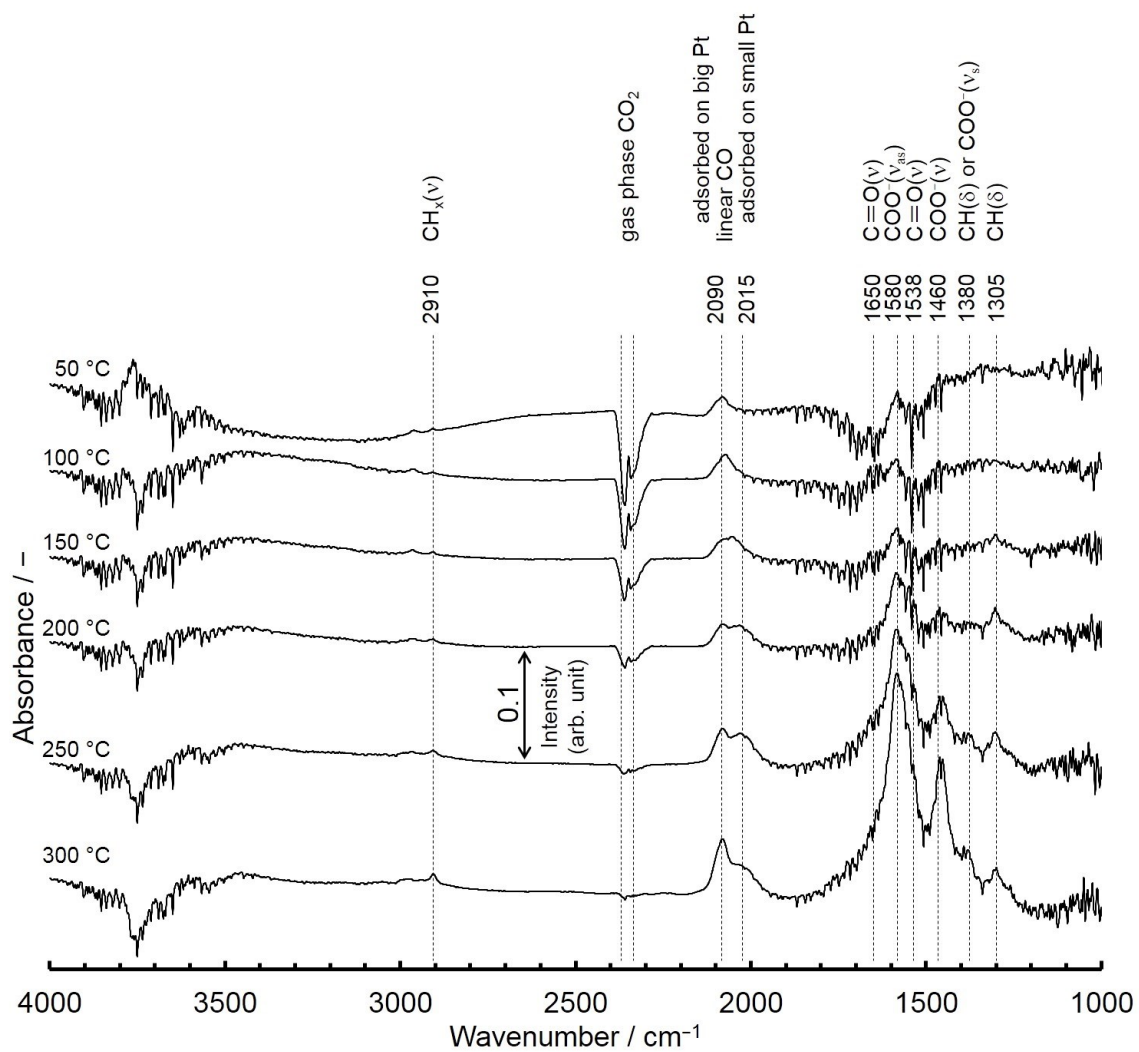
Fig. 2.15 *In situ* FT-IR spectra of C_3H_6 and O_2 adsorbed on Pt/Al_2O_3.
(Spectra are measured in gas feeds of 333 ppm C_3H_6, 1500 ppm O_2 and He balance)
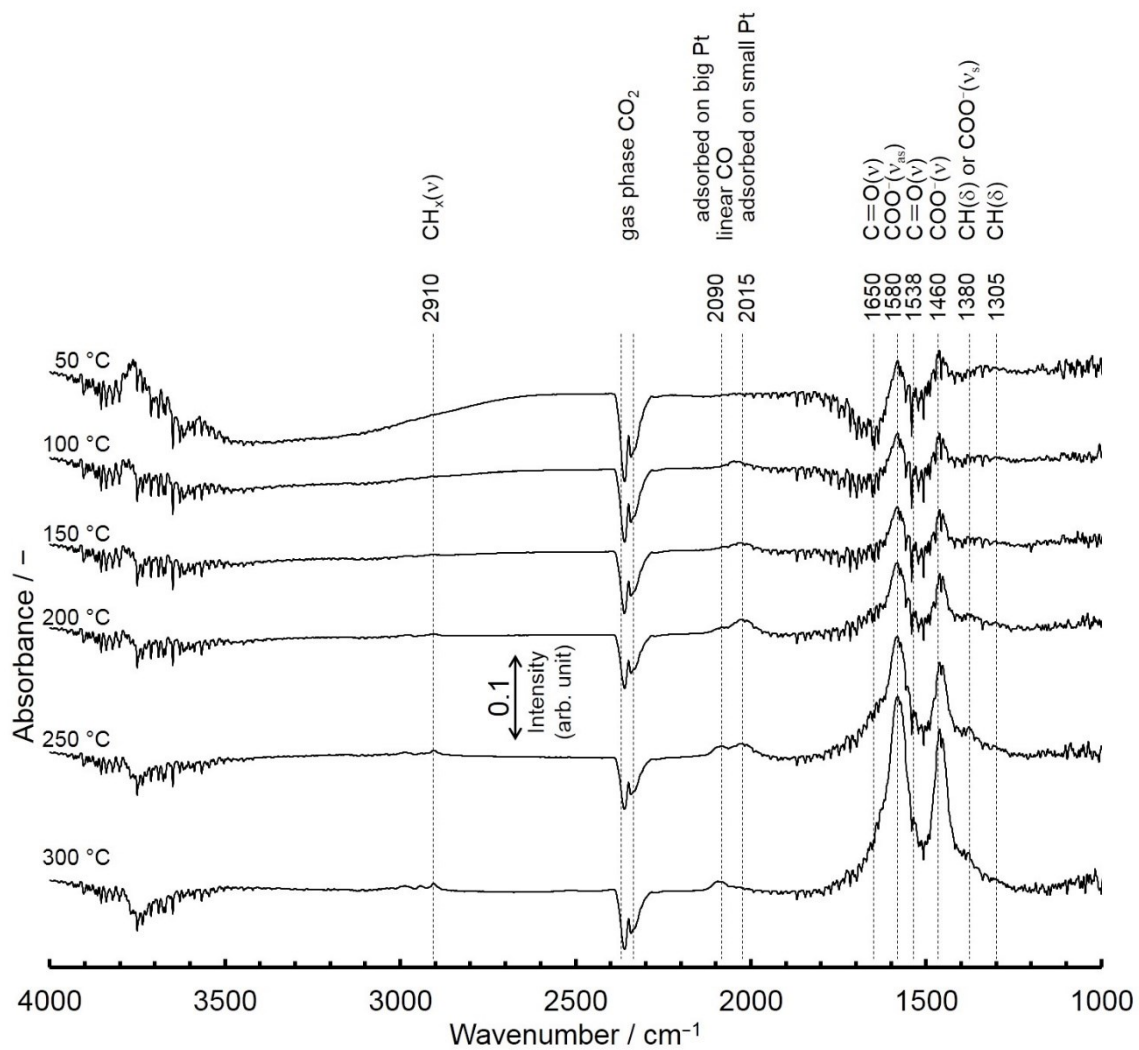
Fig. 2.16   *In situ* FT-IR spectra of C_3H_6 and O_2 adsorbed on Pt/Al_2O_3.
(Spectra are measured in gas feeds of 333 ppm C_3H_6, 3000 ppm O_2 and He balance)
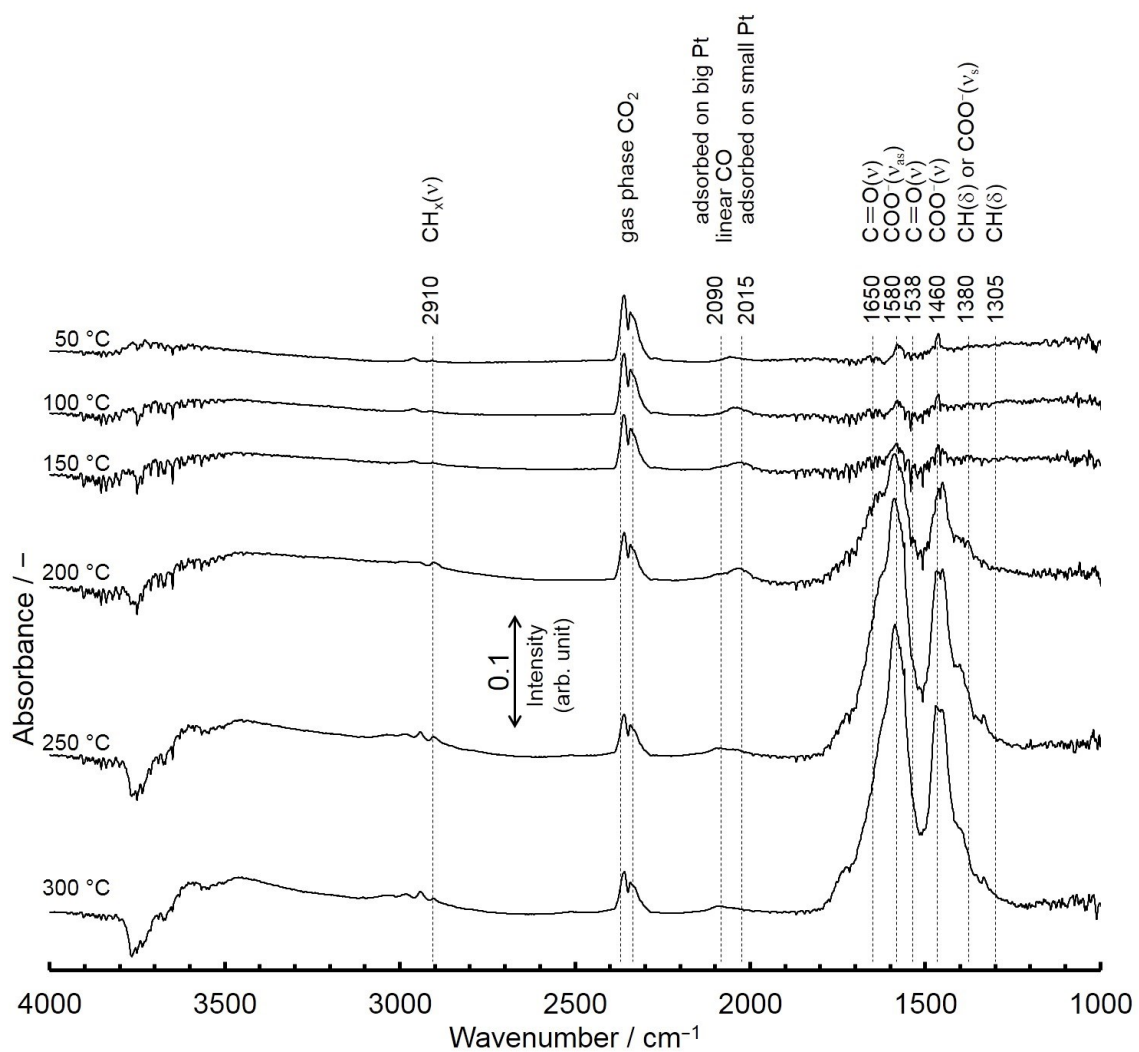
Fig. 2.17 *In situ* FT-IR spectra of C_3H_6 and O_2 adsorbed on Pt/Al_2O_3.
(Spectra are measured in gas feeds of 333 ppm C_3H_6, 10000 ppm O_2 and He balance)

2.8   Conclusions

Experimental studies of the gas phase conversion and surface species are conducted by using monolith honeycomb catalyst and powdered catalyst, which is the fragment of monolith washcoat.   Gas phase conversion rate experiments are measured by using Fourier Transform Infrared (FT-IR) equipment and gas analyzers.   Surface species experiments are measured by using *in-situ* FT-IR equipment.   The physical parameters of the catalyst such as metal dispersions, washcoat pore diameters and so on are identified with powdered catalyst, and furthermore, coverage of surface species in various adsorption regimes are examined by *in-situ* FT-IR under the same conditions of inlet gas temperature and compositions as monolith honeycomb experiments.

From the gas phase experimental results, conclusions can be drawn as the following:

1. C_2H_4 has the highest reactivity among the exhaust hydrocarbon species from the internal combustion engines while CH_4 has the lowest for the catalyst used in this study.
2. Both C_2H_4 and C_3H_6 are important HC species because they show the highest reactivity, and therefore, dominate the light-off performance of the unburned HCs in internal combustion engines.
3. Complete or optimal conversion temperature ranges of C_2H_4 and C_3H_6 become narrower with the increase in oxygen concentration and presence of surface oxygen species on the catalyst promote the decomposition of C_2H_4 and C_3H_6.

From the surface species experimental results, conclusions can be drawn as the following:

4. On the platinum metal, presence of adsorbed HC species and linearly adsorbed CO are confirmed.
5. Faster reaction or oxidation rate of intermediate HC species compared to the oxidation of linearly adsorbed surface CO are observed.
6. Early formation of CO_2 is detected so that the early C-C bond cracking to form the CO_2 is observed.

Chapter 3

Surface Reaction Mechanism

3.1 Introduction

In this chapter, construction of the reaction steps of the detailed surface reaction mechanism for C_2H_4 and C_3H_6 over Pt/Al_2O_3 are presented. Based on the observed facts from the experimental results of gas phase and surface species measurements, reaction steps of the detailed surface reaction mechanisms are considered. Reaction steps are constructed as widely used Langmuir-Hinshelwood mechanism (Baxter and Hu, 2002) in which reactant gas species are chemisorbed as surface species first, then the surface species reactions take place, and then the product surface species are desorbed as gas species. In the following sections, construction of the reaction steps of C_2H_4, C_3H_6 and the basic reaction chemistry sets of $CO / H_2 / O_2$ which are essential for the oxidation of C_2H_4 and C_3H_6 are discussed. Surface reaction steps are proposed depending on the fact that all gas species adsorb to the surface competitively. Detailed structures of the intermediate surface HC species are not clearly observed in the surface species measurements so that the reaction steps for C_2H_4 and C_3H_6 are mainly discussed from the literature.

3.2 C_2H_4 surface reaction mechanism

Ethylene, C_2H_4, gas species usually adsorb on the Pt surface by two means, *di-σ* configuration and *π* configuration. The dominant configuration type varies depending on the kind of surface and co-adsorbed surface species. From the surface experimental studies and fundamental density functional theory (DFT) studies, C_2H_4 gas mostly adsorbs as bridge *di-σ* configuration by occupying two adjacent Pt atoms on the clean crystal Pt (111) surface, supported catalysts, and when the co-adsorbed surface species is atomic surface oxygen (Kesmodel, et al., 1979; Mohsin, et al., 1988; Paffett *et al.*, 1989; Chesters *et al.*, 1990; Tsai, et al., 1997; Zaera and French, 1999; Watwe *et al.*, 2001; Mittendorfer *et al.*, 2003; Burnett *et al.*, 2005). Although there is *π* configuration type adsorption of C_2H_4 gas species on such kinds of surfaces, it is not the main dominant type and the desorption of such species take place even from the low temperature due to the

weakly bound state.   Moreover, for the decomposition or oxidation process, adsorbed *di-σ* configurated C_2H_4 species are the main dominant species, and from the gas phase experimental results discussed in the previous chapter, it is observed that with the increase in oxygen concentration, conversion process take place from the very low temperature. Therefore, for the adsorption step of C_2H_4 gas onto the Pt surface, bridge *di-σ* configuration type occupying two adjacent Pt atoms is adopted and the illustration of adsorbed species is shown in Fig. 3.1.

As for the following oxidation steps, removal of hydrogen by the co-adsorbed surface atomic oxygen is considered because from the gas phase experimental results, it is found that the increase in oxygen concentration makes the light-off temperature lower so that the presence of co-adsorbed oxygen facilitates the dehydrogenation of C_2H_4. After the initial adsorption step, the adsorbed C_2H_4 species occupies one more active surface Pt site, and molecular rearrangement occurs to produce stable ethylidyne (C_2H_3) species (Berlowitz et al., 1985; Chesters et al., 1990; Kesmodel et al., 1979; Mohsin et al., 1988; Tsai et al., 1997; Zaera and French, 1999) and surface OH species.   Here, the ethylidyne species is considered occupying three adjacent Pt surface sites as shown in Fig. 3.2.

Then, the first formation of surface CO_2 from the C-C bond breaking of surface C_2H_3 by two co-adsorbed surface atomic oxygen, is considered as the following step due to the facts that the oxidation reactions are very fast and increase sharply in the gas phase conversion experimental results, and early gas phase CO_2 is detected in the surface species measurement results.   At this step, three occupied Pt sites by surface C_2H_3 species are considered as available open active sites for other species.   Schematic imaging from adsorption step to this step is shown in Fig. 3.3 and the proposed reaction steps are shown in Table 3.1.   From this step, skeletal oxidation of the CH_3 by the co-adsorbed surface atomic oxygen is considered to be proceeded as the following steps until the complete oxidation without the formation of surface carbon.   Formation of surface carbon is not observed both in the gas phase conversion experiments and in the surface species experiments.   Total number of twelve reversible reaction steps are proposed for C_2H_4 reaction mechanism as shown in Table 3.1.   Here, it can be noted that only up to the formation of linearly adsorbed surface CO is shown in Table 3.1 and the oxidation of linearly adsorbed surface CO to surface CO_2 is discussed in the CO / O_2 reaction mechanism section and shown in Table 3.3.
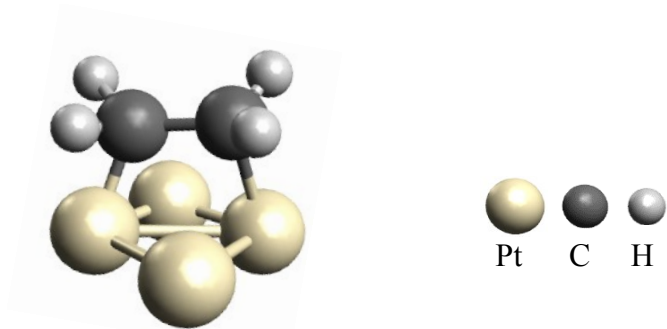
Fig. 3.1   Illustration of the adsorbed C_2H_4 species
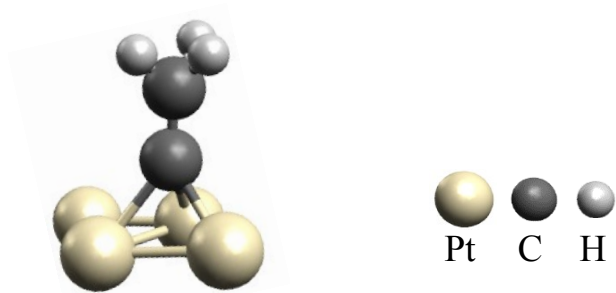
Fig. 3.2   Illustration of the adsorbed C_2H_3 species

Table 3.1   Proposed reaction steps for C_2H_4 surface reaction mechanism
(Notation 'S' stands for one active surface site or one occupied surface site, and '2S'
and '3S' stand for two and three active surface sites or occupied surface sites)

No.	Reaction		
R1:	$C_2H_4 + 2.0\ Pt(S)$	$\rightarrow$	$C_2H_4(2S)$
R2:	$C_2H_4(2S)$	$\rightarrow$	$C_2H_4 + 2.0\ Pt(S)$
R3:	$C_2H_4(2S) + O(S) + Pt(S)$	$\rightarrow$	$C_2H_3(3S) + OH(S)$
R4:	$C_2H_3(3S) + OH(S)$	$\rightarrow$	$C_2H_4(2S) + O(S) + Pt(S)$
R5:	$C_2H_3(3S) + 2.0\ O(S)$	$\rightarrow$	$CH_3(S) + CO_2(S) + 3.0\ Pt(S)$
R6:	$CH_3(S) + CO_2(S) + 3.0\ Pt(S)$	$\rightarrow$	$C_2H_3(3S) + 2.0\ O(S)$
R7:	$CH_3(S) + O(S)$	$\rightarrow$	$CH_2(S) + OH(S)$
R8:	$CH_2(S) + OH(S)$	$\rightarrow$	$CH_3(S) + O(S)$
R9:	$CH_2(S) + O(S)$	$\rightarrow$	$CH(S) + OH(S)$
R10:	$CH(S) + OH(S)$	$\rightarrow$	$CH_2(S) + O(S)$
R11:	$CH(S) + O(S)$	$\rightarrow$	$CO(S) + H(S)$
R12:	$CO(S) + H(S)$	$\rightarrow$	$CH(S) + O(S)$
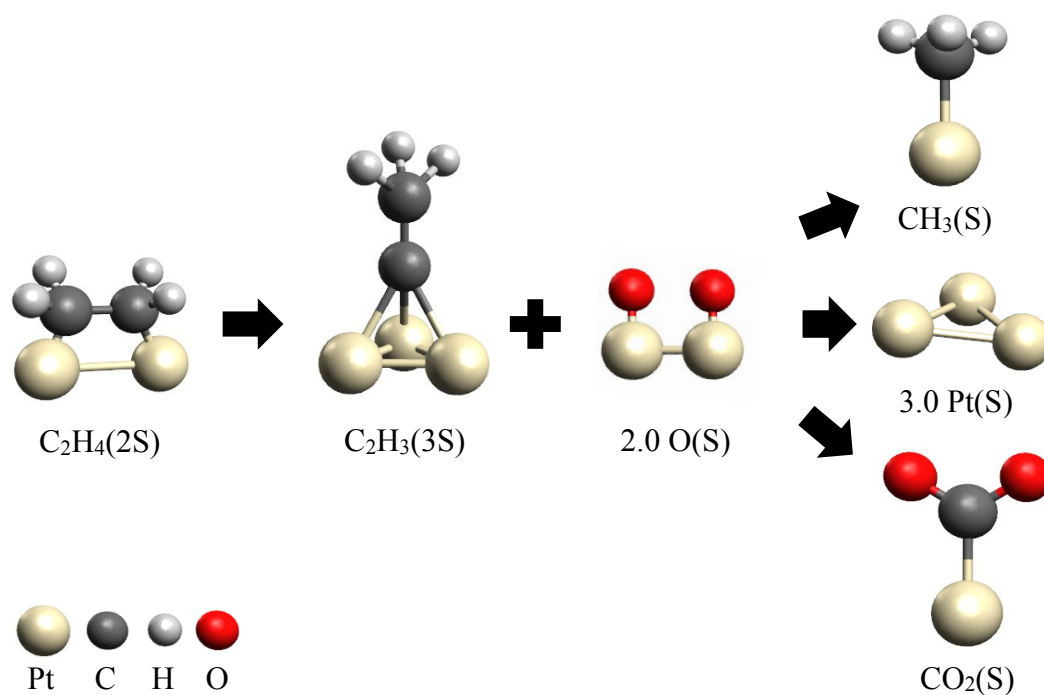
Fig. 3.3   Schematic diagram of the reaction steps of C_2H_4 reaction mechanism from the adsorption step to the first formation of surface CO_2 step

(Notation 'S' stands for one active surface site or one occupied surface site, and '2S' and '3S' stand for two and three active surface sites or occupied surface sites)

3.3   C₃H₆ surface reaction mechanism

Propylene, C_3H_6, gas species also usually adsorb on the Pt surface by two means, *di-σ* configuration and *π* configuration.   As ethylene, the dominant configuration type of propylene varies depending on the kind of surface and co-adsorbed surface species. From the surface experimental studies and fundamental density functional theory (DFT) studies, C_3H_6 gas mostly adsorbs as bridge *di-σ* configuration by occupying two adjacent Pt atoms on the clean crystal Pt (111) surface, supported catalysts, and when the co-adsorbed surface species is atomic surface oxygen (Chesters et al., 1990; Koestner et al., 1982; Nykänen and Honkala, 2013, 2011; Tsai et al., 1997; Valcárcel et al., 2002). Similar to ethylene, there is also *π* configuration type adsorption of C_3H_6 gas species on such kinds of surfaces, it is not the main dominant type and the desorption of such species take place even from the low temperature because of their weakly bound state. Moreover, for the decomposition or oxidation process, adsorbed *di-σ* configurated C_3H_6 species are the main dominant species, and from the gas phase experimental results discussed in the previous chapter, it is observed that with the increase in oxygen concentration, conversion process take place from the low temperature.   Therefore, for the adsorption step of C_3H_6 gas onto the Pt surface, bridge *di-σ* configuration type occupying two adjacent Pt atoms is adopted and the illustration of adsorbed species is shown in Fig. 3.4.

Here, the same dehydrogenation concept, which is the removal of hydrogen by the co-adsorbed surface atomic oxygen, is considered as ethylene reaction steps.   After the adsorption step, the adsorbed surface C_3H_6 dehydrogenates to form C_3H_5 surface species.   Some studies report that the surface species can be assigned as propylidyne species, which occupies three-fold Pt atoms, after the molecular rearrangement.   Some other studies report the species as 2-propenyl or 1-methyl vinyl species which occupies three adjacent Pt atoms (Gabelnick et al., 2000; Nykänen and Honkala, 2013; Valcárcel et al., 2006).   However, the species is an arguable one because the band assignment for the experimental results is complicated (Hazlett et al., 2017; Valcárcel et al., 2006). Different from the ethylene, propylene has a methyl group with hydrogen atoms and also in the vinylic positions so that the hydrogen atom, which is firstly dehydrogenated is contradictory.   Isotope experimental studies using deuterated propylene species prove that the vinylic hydrogen atoms are supposed to be dehydrogenated first by the co-adsorbed surface atomic oxygen (Gabelnick et al. 2000; Gabelnick and Gland 1999). Therefore, formation of stable intermediate surface C_3H_5(1-methyl vinyl) species which occupies three adjacent Pt atoms, as shown in Fig. 3.5, is considered as a following step

after the adsorption step of C_3H_6.

Then the next vinylic hydrogen dehydrogenated by the co-adsorbed surface atomic oxygen, and the formation of stable intermediate surface C_3H_4 species as shown in Fig. 3.6 is considered.

After this step, the first breaking of C-C bond resulting the formation of surface one Pt atom sited CH species and the same stable intermediate species, ethylidyne (C_2H_3) shown in Fig. 3.2, as C_2H_4 reaction mechanism is considered. Then, the same surface reaction steps are considered as C_2H_4 oxidation process for the following steps. Schematic imaging from adsorption step of C_3H_6 to the formation of C_2H_3 step is shown in Fig. 3.7 and the proposed reaction steps are shown in Table 3.2. Formation of surface carbon is also not observed for C_3H_6 both in the gas phase conversion experiments and in the surface species experiments. Total number of sixteen reversible reaction steps are proposed for C_3H_6 reaction mechanism as shown in Table 3.2. Here, it can also be noted that only up to the formation of linearly adsorbed surface CO is shown in Table 3.1 and the oxidation of linearly adsorbed surface CO to surface CO_2 is discussed in the CO / O_2 reaction mechanism section and shown in Table 3.3.
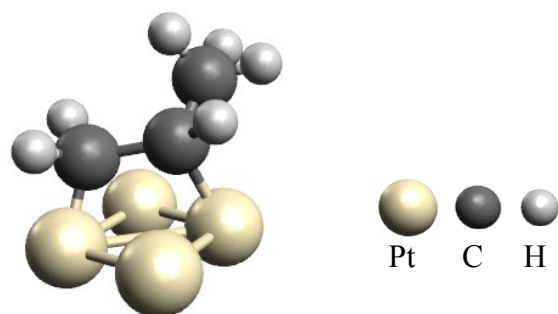
Fig. 3.4   Illustration of the adsorbed C_3H_6 species
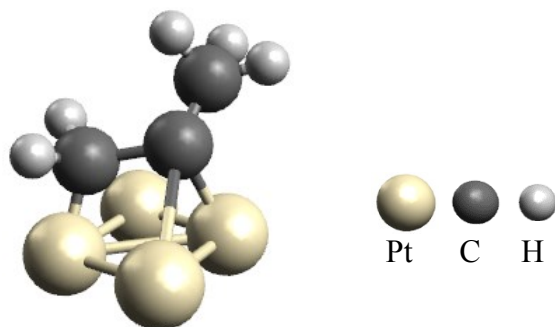
Fig. 3.5   Illustration of the adsorbed C_3H_5 species
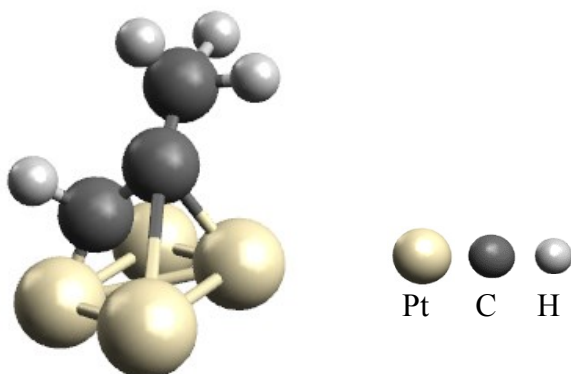
Fig. 3.6   Illustration of the adsorbed C_3H_4 species

Table 3.2 Proposed reaction steps for C_3H_6 surface reaction mechanism
(Notation 'S' stands for one active surface site or one occupied surface site, and '2S'
and '3S' stand for two and three active surface sites or occupied surface sites)

No.	Reaction		
R1:	$C_3H_6 + 2.0\ Pt(S)$	$\rightarrow$	$C_3H_6(2S)$
R2:	$C_3H_6(2S)$	$\rightarrow$	$C_3H_6 + 2.0\ Pt(S)$
R3:	$C_3H_6(2S) + O(S) + Pt(S)$	$\rightarrow$	$C_3H_5(3S) + OH(S)$
R4:	$C_3H_5(3S) + OH(S)$	$\rightarrow$	$C_3H_6(2S) + O(S) + Pt(S)$
R5:	$C_3H_5(2S) + O(S)$	$\rightarrow$	$C_3H_4(3S) + OH(S)$
R6:	$C_3H_4(3S) + OH(S)$	$\rightarrow$	$C_3H_5(2S) + O(S)$
R7:	$C_3H_4(3S) + Pt(S)$	$\rightarrow$	$C_2H_3(3S) + CH(S)$
R8:	$C_2H_3(3S) + CH(S)$	$\rightarrow$	$C_3H_4(3S) + Pt(S)$
R9:	$C_2H_3(3S) + 2.0\ O(S)$	$\rightarrow$	$CH_3(S) + CO_2(S) + 3.0\ Pt(S)$
R10:	$CH_3(S) + CO_2(S) + 3.0\ Pt(S)$	$\rightarrow$	$C_2H_3(3S) + 2O(S)$
R11:	$CH_3(S) + O(S)$	$\rightarrow$	$CH_2(S) + OH(S)$
R12:	$CH_2(S) + OH(S)$	$\rightarrow$	$CH_3(S) + O(S)$
R13:	$CH_2(S) + O(S)$	$\rightarrow$	$CH(S) + OH(S)$
R14:	$CH(S) + OH(S)$	$\rightarrow$	$CH_2(S) + O(S)$
R15:	$CH(S) + O(S)$	$\rightarrow$	$CO(S) + H(S)$
R16:	$CO(S) + H(S)$	$\rightarrow$	$CH(S) + O(S)$
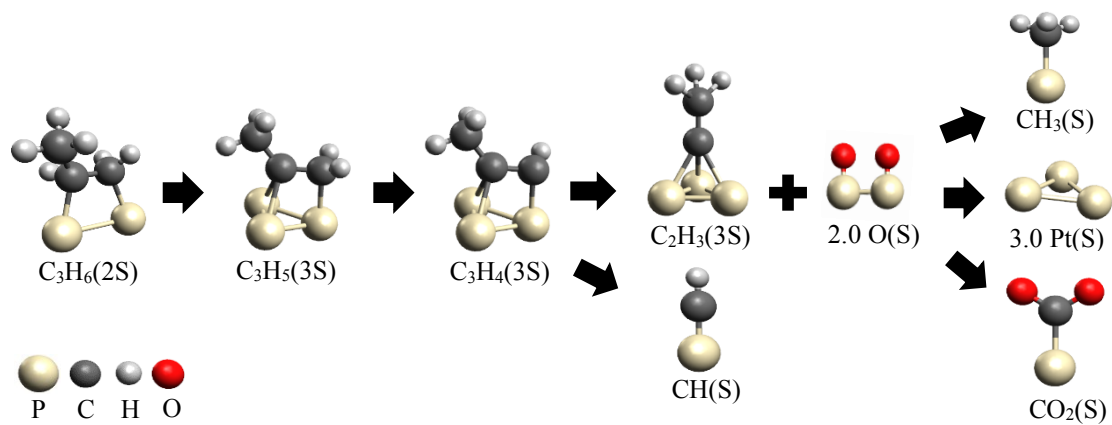
Fig. 3.7   Schematic diagram of the reaction steps of C_3H_6 reaction mechanism from

the adsorption step to the first formation of surface CO_2 step

(Notation 'S' stands for one active surface site or one occupied surface site, and '2S'
and '3S' stand for two and three active surface sites or occupied surface sites)

3.4   CO / H₂ / O₂ surface reaction mechanism

As for CO / O_2 surface reaction mechanism, which is one of the essential parts of hydrocarbon oxidation mechanisms, extensive gas phase conversion experimental and surface experimental studies have been conducted (Shimokuri et al., 2020).   In the studies, the same hypothesis has been applied that the detailed CO / O_2 surface reaction mechanism on Pt/Al_2O_3 is developed by the gas phase and surface species measurements. CO / O_2 gas phase conversion experiments are conducted by using the same catalyst, the experimental setup and method presented in chapter 2, and surface species experimental setup and method are also conducted in the same way.

Figure 3.8 shows the result of *in-situ* FT-IR on Pt/Al_2O_3, in which the adsorption intensities of each surface species for various temperature conditions are shown.   The adsorbed species are identified based on the literature (Holmgren et al., 1999).   On Pt/Al_2O_3 surface, it can be seen that only "linear" CO adsorption, i.e., one molecule of CO adsorbed on one Pt site is detected (2060 cm^{-1}, 2080 cm^{-1} and 2100 cm^{-1}).   Same as the C_2H_4 and C_3H_6 surface experimental measurements, only linear CO species is detected on the Pt and therefore, the developed CO / O_2 surface reaction mechanism (Shimokuri et al., 2020) can be applied.

Moreover, CO / H_2 / O_2 surface reaction mechanism is continued to develop with the same methods and procedures by the gas phase and surface species measurements. Figure 3.9 shows the result of *in-situ* FT-IR on Pt/Al_2O_3, in which the adsorption intensities of each surface species for various temperature conditions are shown.   The adsorbed species are also identified based on the literature (Holmgren et al., 1999). Similarly, as CO / O_2 surface measurement results, it can be seen that only "linear" CO adsorption, i.e., one molecule of CO adsorbed on one Pt site is detected (2060 cm^{-1}, 2080 cm^{-1} and 2100 cm^{-1}).

From the surface species measurement results and literature studies (Chatterjee et al., 2001; Koop and Deutschmann, 2009; Kota et al., 2017; Shimokuri et al., 2020), CO / H_2 / O_2 surface reaction mechanism is considered.   As for adsorption steps, dissociative adsorption of H_2 and O_2, and non-dissociative adsorption of CO, are considered and the oxidation steps are accordingly.   Total number of eighteen reversible reaction steps are proposed for CO / H_2 / O_2 reaction mechanism as shown in Table 3.3.   Formation of surface CO_2 and H_2O steps are included, and single Pt active site is considered to be used for each surface species throughout the oxidation process.
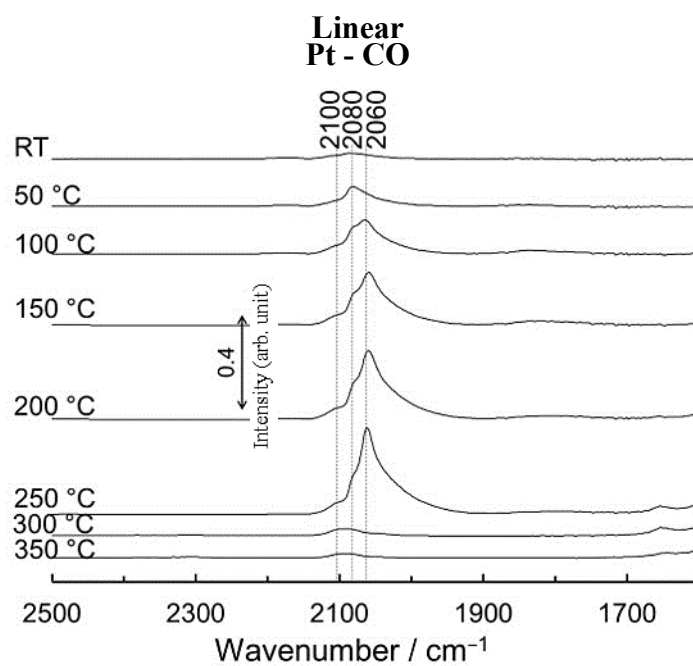
Fig. 3.8   *In situ* FT-IR spectra of CO and O$_2$ adsorbed on Pt/Al$_2$O$_3$.
(Spectra are measured in gas feeds of 3000 ppm CO, 1500 ppm O$_2$ and He balance)
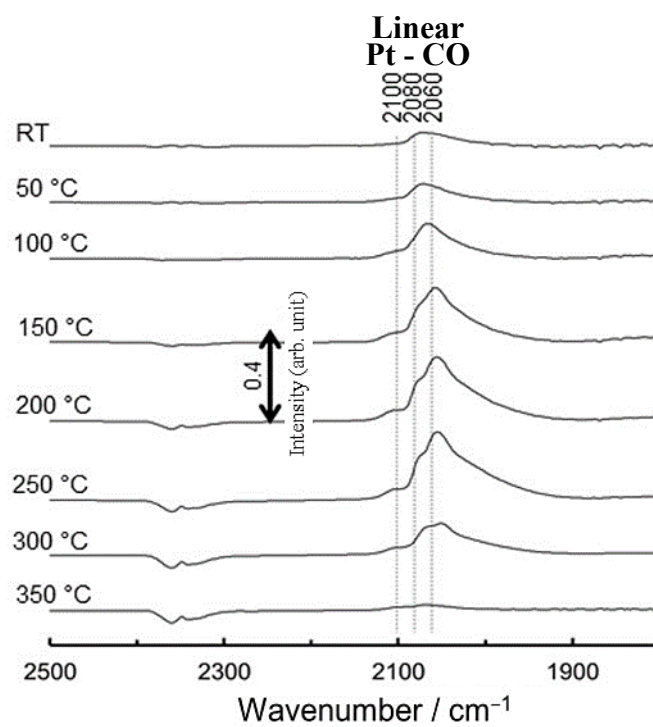
Fig. 3.9   *In situ* FT-IR spectra of CO, H_2 and O_2 adsorbed on Pt/Al$_2$O$_3$.
(Spectra are measured in gas feeds of 1000 ppm CO, 3000 ppm H_2, 1500 ppm O_2 and He balance)

Table 3.3   Proposed reaction steps for CO / H_2 / O_2 surface reaction mechanism
(Notation 'S' stands for one active surface site or one occupied surface site)

No.	Reaction		
R1:	O_2 + 2.0 Pt(S)	$\rightarrow$	2.0 O(S)
R2:	2.0 O(S)	$\rightarrow$	O_2 + 2.0 Pt(S)
R3:	CO + Pt(S)	$\rightarrow$	CO(S)
R4:	CO(S)	$\rightarrow$	CO + Pt(S)
R5:	H_2 + 2.0 Pt(S)	$\rightarrow$	2.0 H(S)
R6:	2.0 H(S)	$\rightarrow$	H_2 + 2.0 Pt(S)
R7:	CO_2 + Pt(S)	$\rightarrow$	CO_2(S)
R8:	CO_2(S)	$\rightarrow$	CO_2 + Pt(S)
R9:	H_2O + Pt(S)	$\rightarrow$	H_2O(S)
R10:	H_2O(S)	$\rightarrow$	H_2O + Pt(S)
R11:	CO(S) + O(S)	$\rightarrow$	CO_2(S) + Pt(S)
R12:	CO_2(S) + Pt(S)	$\rightarrow$	CO(S) + O(S)
R13:	H(S) + O(S)	$\rightarrow$	OH(S) + Pt(S)
R14:	OH(S) + Pt(S)	$\rightarrow$	H(S) + O(S)
R15:	OH(S) + H(S)	$\rightarrow$	H_2O(S) + Pt(S)
R16:	H_2O(S) + Pt(S)	$\rightarrow$	OH(S) + H(S)
R17:	OH(S) + OH(S)	$\rightarrow$	H_2O(S) + O(S)
R18:	H_2O(S) + O(S)	$\rightarrow$	OH(S) + OH(S)
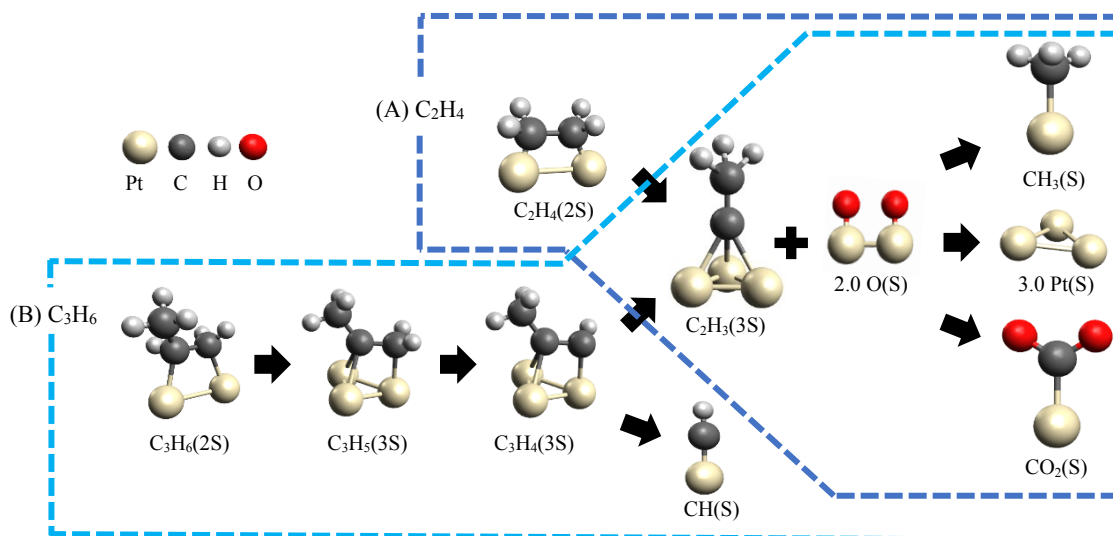
Fig. 3.10   Schematic diagram of formation of former surface species from the
oxidation of (A) C_2H_4 and (B) C_3H_6 in proposed surface reaction mechanism
(Notation 'S' stands for one active surface site or one occupied surface site, and '2S'
and '3S' stand for two and three active surface sites or occupied surface sites)

3.5   Reactions on the support material

In this study, it is assumed that reactions on the support material (Al_2O_3) are enough slower than that on PGM, and therefore, negligible.   Some intermediate species, reported by the recent studies (Hazlett et al., 2017; Hazlett and Epling, 2016), such as formates, formaldehyde, acetate, acetic acid and acetone are not included since it is not clearly observed on Pt by the surface species measurements used in this study.

3.6   Conclusions

In this chapter, from the surface species measurement results and literature studies, consideration and construction of reaction steps of C_2H_4 and C_3H_6 are discussed and conclusions can be drawn as the following:

1. Multiple site occupations of active Pt surface sites are included for both C_2H_4 and C_3H_6 surface reaction steps from the adsorption step to the oxidation steps and schematic of it is shown in Fig. 3.10.
2. Formation of the same intermediate surface species with three Pt, which is C_2H_3, is proposed in the surface reaction steps and schematic of it is shown in Fig. 3.10.
3. Early formation of surface CO_2 reaction step is included and the early bond breaking of Carbon-Carbon is included as it observed from the surface species measurement results and schematic of it is shown in Fig. 3.10.

As the core part of hydrocarbon surface reaction mechanism, CO / H_2 / O_2 reaction steps are considered and discussed from the surface species measurements as well and conclusions can be drawn as the following:

4. Linearly adsorbed surface CO is observed for the cases of both CO / O_2 and CO / H_2 / O_2 surface species measurements, and, it is included in the surface species reaction mechanisms.
5. Adsorption and desorption of surface CO, H_2, O_2, CO_2 and H_2O reversible reaction steps are included.

Chapter 4

Numerical Modelling

4.1 Introduction

In this chapter, numerical modelling method used in this study is presented. On the numerical simulation, the numerical simulation code "aftertreatment model" (ATM model) of BOOST^{TM} (AVL Corp.) which models a single cell of monolith honeycomb reactor is used. In this simulation code, not only the gas flow along the cell channel but also diffusion into the washcoat layer can be simulated. The principles of ATM model are almost the same as well-established numerical models for honeycomb monolith catalyst (Hayes and Kolaczkowski, 1998; Mladenov *et al.*, 2010; Deutschmann, 2015). Details of the governing equations for mass conservation, momentum conservation, energy conservation and species transport, together with user defined catalytic reactions in the model are explained in the following sections. As for the kinetic parameter estimation and validation, thermodynamic consistency between the gas phase reactions and detailed surface reactions is used as the same manner as Stotz et.al. (Stotz et al., 2017).

4.2 Principle of Heterogeneous Catalytic Reactions

In the catalytic reaction modelling, heterogeneous catalytic reactions are the major and important reactions in which gas phase (reactants and products) and solid catalyst contained. In the practical monolith catalysts, reactants from the bulk gas phase must be entered into the porous catalytic washcoat layer, carried out the reactions to form products and transported again into the bulk gas phase. Numerical modelling for the overall heterogenous catalytic reaction process needs to consider not only the physical transport phenomena but also the kinetic reaction steps. The existence of a boundary layer between the solid catalyst surface and the bulk fluid stream can have the variations of velocity, temperature and concentrations. Therefore, not only the kinetic parameters of the heterogenous chemistry steps and transport properties from the bulk fluid stream to the solid catalyst surface can have limiting effect on the rate of reactions.

Individual steps taking place during the heterogenous catalytic reaction are as follows and can be seen in Fig. 4.1, which is adapted from Hayes et.al. and BOOST Aftertreatment documentation (Hayes and Kolaczkowski, 1998; Boost).

1. Transport of the reactants from the bulk gas phase to the external solid surface across the boundary layer.
2. Diffusion of the reactants into the porous washcoat layer of the catalyst.
3. Adsorption of the gas phase reactants onto the surface to form surface reactant species.
4. Reaction of reactant species at the surface to from intermediate species, and then surface product species.
5. Desorption of the surface product species from the surface to form gas phase products.
6. Diffusion of the products to the porous washcoat layer of the catalyst.
7. Transport of the products into the bulk gas phase.

Here, in the ATM model, steps including the adsorption and desorption reactions to proceed the catalytic reactions as surface species reactions can be treated so that the proposed C_2H_4 and C_3H_6 reaction mechanism discussed in chapter 3 can be applied as the surface reaction mechanism of the heterogenous catalytic reaction model.
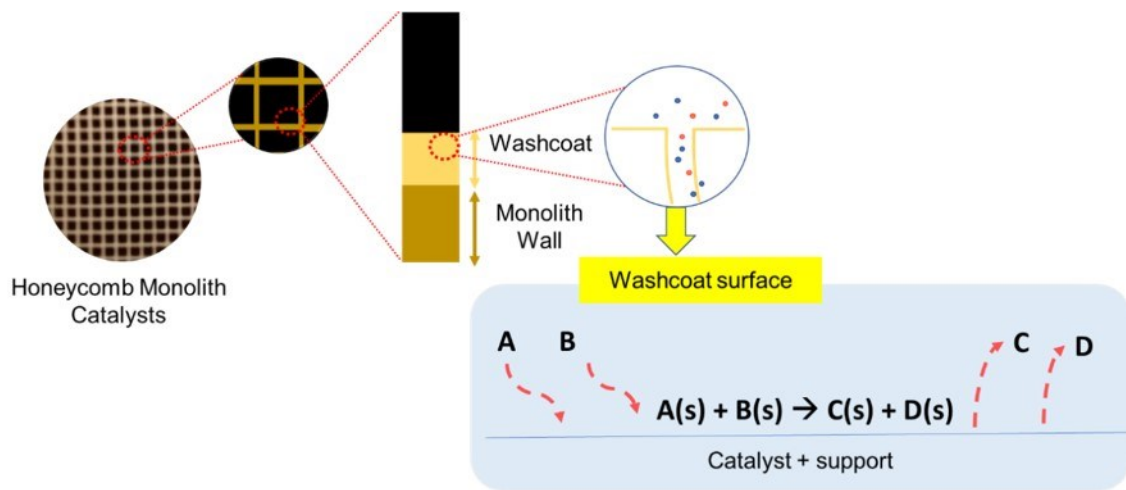
Fig. 4.1   Principle steps of the heterogenous catalytic reaction
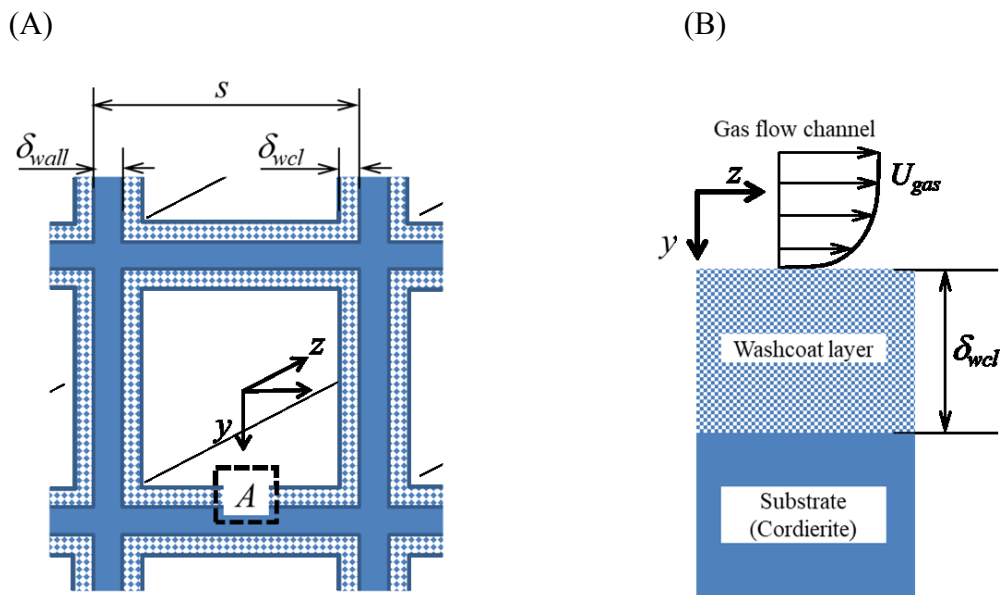
Fig. 4.2   Schematic of honeycomb monolith reactor model (cross-sections normal (A) and parallel (B) to the honeycomb cell). (B) is the magnified image of part A in (A)

4.3   Monolith honeycomb catalytic converter model

First, the equations presented in the ATM model are discussed and the additional equations considered in the numerical model are discussed in later section.

4.3.1   Cell Specification of the model

There are numerous cell channels, in which the washcoat layer and solid substrate is comprised, in a monolith honeycomb catalyst. The cells present in the catalyst used in the experimental studies composed of square cell channels and in the catalytic model, it is treated in such a way. Schematic image of the numerical model used in this study is illustrated in Fig. 4.2. On the model, the monolith honeycomb catalyst consists of wash coat layer and inert monolith wall. The honeycomb cell is discretized in z and y direction where z axis is the direction of main gas flow and y axis is perpendicular to the catalyst solid wall.

The repeat distance of the monolith (indicated as "s" in Fig. 4.2(A)) can be derived from the cell density, CPSM (Cells Per Square Meter) according to

$$s = \sqrt{\frac{1}{CPSM}} \qquad (4.1)$$

In this study, systematic thorough characterization of catalyst is done by the surface species measurements, and 600 CPSI (Cell Per Square Inch) is reported as shown in Table 2.1. With the CPSI number, CPSM value can be obtained by the following equation,

$$CPSM = \frac{1}{(0.0254)^2} CPSI \qquad (4.2)$$

Total thickness of the monolith's wall, δ, is obtained by the following equation,

$$\delta = \delta_{wall} + 2\delta_{wcl} \qquad (4.3)$$

where δ_{wall} is the thickness of the substrate wall and δ_{wcl} is the thickness of the washcoat layer.   The value of each parameter is 0.09 mm and 0.057 mm respectively, as shown in Table 2.1.   Then the hydraulic channel diameter is obtained by the following equation,

$$d_{hyd} \ = \ s - \delta \qquad (4.4)$$

From that parameter, fluid volume fraction, ε_g , and Geometric Surface Area (GSA), which is the channel wetter perimeter in surface per monolith volume is obtained by the following equations,

$$\varepsilon_g = \frac{d_{hyd}^2}{s^2} \qquad (4.5)$$

$$GSA = \frac{4d_{hyd}}{s^2} \qquad (4.6)$$

4.3.2   Assumption of mass or mole balance

In the ATM model, mass balance is assumed as a preference over mole balance due to the following reasons,

(1) Total mass remains constant while the number of mole changes during the chemical reactions, and

(2) Various physical properties such as enthalpies or caloric values are given as a function of their mass while the molar mass necessary is not usually accessible.

4.3.3   Assumption of fractions

In the ATM model, assumptions of fraction are included to state the volume and density of the species.   For a heterogeneous catalytic reaction, gas phase as well as solid phase is considered.   Gas phase or fluid phase volume fraction, ε_g, can also be defined by the following equation,

$$\varepsilon_g = \frac{V_g}{V} \tag{4.7}$$

where, V is the reactor volume. Solid volume fraction, ε_s, can be defined as follows,

$$\varepsilon_s = 1 - \varepsilon_g \tag{4.8}$$

Density of a single phase can be considered as integration of the densities of all species in that phase if the phase is composed of various species. The mass fraction of specific species, $w_{k,g}$, in that phase can be defined in a ratio of specific species density, $\rho_{k,g}$, to the total density of the phase, ρ_g, as follows,

$$w_{k,g} = \frac{\rho_{k,g}}{\rho_g} \tag{4.9}$$

The sum of all mass fractions can always be defined as one by the above equations.

4.3.4 State equation

In the ATM model, the ideal gas law is assumed to be sufficient enough as an equation of state since the pressures and temperatures in a catalytic application are in the range of P <10 bar and T <3000 K.

$$\rho_g = \frac{p_g}{RT_g} MG_g \tag{4.10}$$

where ρ_g is mass density, p_g is the pressure, and MG_g is the total molar mass, T_g is the temperature and R is the ideal gas constant. The molar mass is a function of each composition consisting of different chemical species k.

$$MG_g = \frac{1}{\sum_k^k \frac{w_{k,g}}{MG_{k,g}}} \tag{4.11}$$

where $MG_{k,g}$ represents the molar mass of chemical species k in the gas phase.

4.3.5   Single channel balance equations

In the ATM model, the entire catalytic converter can be treated as a single channel by assuming that radial transport effects are small enough comparing with axial heat transport.   Radial gradients in the channel can be neglected and,

(1) the convective, diffusive and conductive transport in the gas phase,

(2) mass and energy transfer through the boundary layer,

(3) diffusion and catalytic conversion in the washcoat, and

(4) conduction in the solid phase are assumed as the phenomena taking place in the channel.

Therefore, the transient and one dimensional in the axial direction (z direction in Fig. 4.2) are considered.   Here, in this ATM model, the diffusion phenomenon in the washcoat can be treated independently with the axial gas flow phenomena so that it can be represented as a 1+1 dimensional tool for heterogenous catalytic reaction modelling in which the washcoat layer diffusion phenomenon is important.

Based on the above assumptions, mass, momentum and energy differential conservation equations in gas phase along the square cell can be written as follows.

The continuity equation of the gas phase is,

$$\frac{\partial \rho_g}{\partial t} = \frac{\partial \rho_g v_g}{\partial z} \tag{4.12}$$

where ρ_g is the density of the gas phase, t is the time, v_g is the interstitial gas velocity and z is the spatial coordinate in axial direction.

The momentum conservation equation is,

$$\frac{\partial p_g}{\partial z} = -\left[\frac{\varphi \zeta}{2} \cdot \frac{\dot{m}}{A_{cross} d_{hyd}}\right] v_g \qquad (4.13)$$

where p_g is the pressure of the system, and the terms in the square brackets are derived by the steady state Darcy equation and Darcy constant (Kaviany, 1991) in which fanning friction factor (φ), friction coefficient (ζ), and hydraulic diameter (d_{hyd}) are included. The cell channel of the monolith catalyst used in this study has a square cross section and in the ATM model, the value of fanning friction factor (φ) is defined as 0.89. The friction coefficient (ζ) is typically described as function of Reynolds Number, Re and the gas flow in the cell channel is the laminar flow, therefore, the laminar friction coefficient (ζ) is defined as follows,

$$\zeta = \zeta_{lam} = aRe^b \qquad (4.14)$$

where *a* and *b* are input values. The default values of these parameters are used as 64 and -1 as default values according to the Hagen-Poisseuille-law for laminar tube flow.

The species conservation equation is considered for all the species in the gas phase by integrating the number of species in the gas flow, species in the diffusion and species in the chemical reaction and, is as follows,

$$\varepsilon_g \frac{\partial \rho_g w_{k,g}}{\partial t} = \qquad (4.15)$$

$$-\varepsilon_g \frac{\partial \rho_g w_{k,g} v_g}{\partial z} + \varepsilon_g \frac{\partial}{\partial z}\left(\rho_g D_{k,eff} \frac{\partial w_{k,g}}{\partial z}\right) + MG_{k,g} \sum_i^I v_{i,k} \dot{r}_i(c_k^L, T_S)$$

where $w_{k,g}$ is the mass fraction of species k and $D_{k,eff}$ is an effective diffusion coefficient. $\dot{r}_i(c_k^L, T_S)$ represents the molar reaction rate of the catalytic surface reactions with their stoichiometric coefficients $v_{i,k}$.

In the ATM model, homogeneous gas phase reactions are negligible due to their temperature range of applications, and therefore, not considered. The energy conservation considers for the gas and solid phase. In the gas phase, comparing to changes in internal energy, changes in potential energy and kinetic energy are small enough to be ignored (Hayes and Kolaczkowski, 1998). Assuming that, the energy

conservation is generated from heat transfer of all the species in the gas phase, conduction in the gas phase, heat transfer between solid and gas phase due to the diffusion, heat transport in the solid substrate and heat from the catalytic surface reaction, and is as follows,

$$\varepsilon_g \frac{\partial}{\partial t}\left(\rho_g \sum_k^K \omega_{k,g}\, h_{k,g}\right) = -\varepsilon_g \frac{\partial}{\partial z}\left(\rho_g \sum_k^K \omega_{k,g} h_{k,g} v_g\right) + \varepsilon_g \frac{\partial}{\partial z}\left(\lambda_g \frac{\partial T_g}{\partial z}\right)$$

$$+ \sum_k^K \varepsilon_g \frac{\partial}{\partial z}\left(\rho_g D_{k,eff} \sum_k^K \frac{\partial \omega_{k,g}}{\partial z} h_{k,g}\right) + GSA \cdot k_h(T_s - T_g) - \sum_i^I \Delta h_i \dot{r}_i(c_k^L, T_s)$$

$$\tag{4.16}$$

where T_g is the gas temperature and $h_{k,g}$ is the total enthalpy of the component k. Conductive heat transport in the gas phase is modeled by Fourier's law using the thermal conductivity λ_g. The third term on the right side considers the enthalpy transport due to species diffusion. k_h is the heat transfer coefficient between the gas phase and the solid walls, and *GSA* represents the total channel surface area per unit of substrate volume.

Here, the heat of reaction of the catalytic surface reaction is represented by Δh_i, included in the last term of eq. (4.16). The heat of reaction is subsequently added to the solid phase energy balance equation, which is given by

$$\left(1 - \varepsilon_g\right)\rho_s \frac{\partial(c_{p,s} T_s)}{\partial t} =$$

$$-\left(1 - \varepsilon_g\right)\frac{\partial}{\partial z}\left(\lambda_s \frac{\partial T_s}{\partial z}\right) - GSA \cdot k_h(T_s - T_g) + \sum_i^I \Delta h_i \dot{r}_i(c_k^L, T_s) + \dot{q}_{ext}$$

$$\tag{4.17}$$

where, T_s is the temperature of the cordierite, λ_s is the thermal conductivity of it and $\dot{q}_{ext}$ is the heat loss to the surrounding. In the experiment, the monolith honeycomb is wrapped with heat insulator, and the outside of quartz reactor is covered by the glass wool

to reduce the heat loss to the surroundings.   Then, heat loss to the surroundings per unit length of z direction is estimated using the thermal conductivity of cordierite, insulator and quartz, listed in Table 2.1.

In the ATM model, additional balance equations for the surface species concentrations are included because the chemical reactions occur on the catalyst surface so that the concentrations of the species directly above the catalytic surface are not equal to the bulk species concentration.   The molar reaction rate $\dot{r}(c_k^L, T_s)$ in the following equation represents the correlation between the chemical process and mass transport in the reaction.

The molar surface concentration, c_k^L can be evaluated by,

$$GSA \cdot k_{k,m} \cdot (c_k^L - c_{k,g}^B) = \sum_i^I \dot{r}_i (c_k^L, T_s) \qquad (4.18)$$

where $c_{k,g}^B$ is the molar concentration of species k in the bulk gas. $k_{k,m}$ is the mass transfer coefficient of k species.

In this study, the mass transfer coefficient for a species is described by the Sherwood number Sh.

$$k_{k,m} = \frac{Sh \cdot D_{k,g}}{d_{hyd}} \qquad (4.19)$$

where $D_{k,g}$ is the diffusion coefficient of the species k.

Sherwood number Sh, in this model is defined by Sieder/Tate relationship

$$Sh = 1.86 \, (Gz_{mass})^{1/3} \qquad (4.20)$$

Dimensionless Graetz number Gz_{mass}, for the mass transfer is as follows,

$$Gz_{mass} = Re \cdot Sc \cdot \frac{d}{l} \qquad (4.21)$$

where Reynolds number Re, Schmidt number Sc, diameter d and channel length l.

The amount of a certain species stored on the surface is represented by a surface fraction θ_k. The conservation of the species on the surface is accounted by the following equation,

$$\frac{\partial \theta_k}{\partial t}\left(\Theta \cdot GSA\right) = \dot{r_k} \qquad k = 1 \dots K_{stor} \qquad (4.22)$$

where the product ($\Theta \cdot GSA$) of the site density, Θ, and the geometrical surface, GSA, is a measure for the entire storage capacity.

The gas solid heat transfer coefficient in this model, k_h, is defined by Nusselt number Nu,

$$k_h = \frac{Nu \cdot \lambda_g}{d_{hyd}} \qquad (4.23)$$

Nusselt number Nu, is defined by Graetz number (Gz_{heat}). For choosing the model, approximate value of Graetz number is calculated by using the following equation,

$$Gz = \frac{\dot{Q}_{mass,mixture} \cdot c_p}{k_{mixture} \cdot l} \qquad (4.24)$$

where $\dot{Q}_{mass,mixture}$ is the mass transfer rate of the gas mixture.

It is defined by the overall mass transfer rate multiplied by the gas mixture density, ρ_g. c_p is the gas mixture specific heat capacity. $k_{mixture}$ is the gas mixture thermal conductivity. Temperature used for the prediction of Gz are 373 K and 523 K. The approximation gives Gz of 487.9 and 253.5, respectively. Based on the Gz, the Sieder/Tate relationship, for laminar flow in narrow channel (Perry, Green and Southard, 2018; Sieder and Tate, 1936), is used to define the Nusselt number Nu.

Nusselt number Nu defined by Sieder/Tate relationship is as follows,

$$Nu = 1.86 \, (Gz_{heat})^{1/3} \qquad (4.25)$$

By using the correlation of Graetz number Gz_{heat} with Reynolds number Re, Prandtl number Pr, for heat transfer is as follows,

$$Gz_{heat} = Re \cdot Pr \cdot \frac{d}{l} \qquad (4.26)$$

where d is the diameter, and l is the channel length.

Velocity of each species in the system, v_k moving in one direction, and in the ATM model, the relationship of it with the mean velocity of the all species is defined as follows (Bird, Steward and Lightfoot, 2006),

$$v_g \equiv \sum_k^K w_{k,g} v_{k,g} \qquad (4.27)$$

From the relation, mass-averaged velocity can be determined, and the diffusive velocity, $v_{k,g}^D$ which is the difference between the velocity of the mass continuum and that of a single species, is quantified by the following equation in the ATM model following the Fick's first law of diffusion (Taylor and Krishna, 1993),

$$v_{k,g}^D = -\frac{D_{k,g}}{w_{k,g}} \cdot \frac{dw_{k,g}}{dz} \qquad (4.28)$$

Mass-specific enthalpy h_g of the entire gas phase is described as follows,

$$h_g = \sum_k^K w_{k,g} h_{k,g} \qquad (4.29)$$

Then, by the assumption of constant pressure and gas composition, heat capacity

of the entire gas phase can be described as follows,

$$c_p \equiv \left.\frac{\partial h_g}{\partial T_g}\right|_{p_g, w_{k,g}} \qquad (4.30)$$

In the ATM model, required thermodynamic and transport properties for the numerical simulation are calculated based on the literature or by polynomial fittings of the literature (Barin, 1985; Reid, Prausnitz and Poling, 1988; Fuller, Schettler and Giddings, 1966; Perry, Green and Southard, 2018), stored and can be used as internal database. As for the thermodynamic properties of user defined reaction mechanism, if the database is available, CHEMKIN format (Coltrin, Kee and Rupley, 1996) can be used to input, and in this study, gas phase and surface phase thermodynamic properties of the species in the proposed reaction mechanism are referred from the database of DETCHEM (Deutschmann et.al., 2020) and are shown in the Appendix section together with the reaction mechanism in CHEMKIN format.

4.3.6   Boundary conditions

Boundary conditions at the catalyst inlet in axial directions are defined as the experimental conditions. As for the outlet conditions, assumption of adiabatic backflow conditions, where temperature and mass fraction gradients are neglected, are used and it is reasonable to assume for laminar flow of gases in the channel used in catalytic applciations (Hayes and Kolaczkowski, 1998).

In the experiment, the monolith catalyst is wrapped with heat insulator, and the outside of quartz reactor is covered by the glass wool to reduce the heat loss to the surroundings and illustration and schematic of it can be seen in Fig 4.3.

Heat loss to the surroundings per unit length of z direction is calculated by the following equation,

$$\dot{q}_{ext} = k_{out} d_{mon} \pi \Delta T_{s-e} \qquad (4.31)$$

where d_{mon} is the monolith diameter, and ΔT_{s-e} is the difference between monolith temperature at the boundary, T_s, with the temperature at the surrounding, T_e.

Overall heat loss coefficient k_{out} is determined by the conduction occurred between the monolith and the insulator, between the insulator and the reactor wall,

between the reactor wall and the boundary layer, and is as follows,

$$k_{out} = \cfrac{1}{\cfrac{d_{mon}}{2} \cdot \left[\cfrac{1}{\lambda_{mat}} \cdot \ln\left(\cfrac{d_{mat}}{d_{mon}}\right) + \cfrac{1}{\lambda_{shell}} \cdot \left(\cfrac{d_{shell}}{d_{mat}}\right) + \cfrac{1}{\alpha_{out}} \cdot \cfrac{1}{d_{shell}}\right]} \quad (4.32)$$

where d_{mat} is the diameter of the insulator, d_{shell} is the diameter of the reactor wall, λ_{mon} is the thermal conductivity of the monolith catalyst, λ_{mat} is the thermal conductivity of the insulator, λ_{shell} is the conductivity reactor wall, and α_{out} is the heat transfer coefficient between the outer surface of the shell and the environment.

4.3.7   Initial conditions

In the ATM model, all initial conditions are derived from the inlet boundary conditions.   Inlet temperature of the solid is assumed to be identical as it is defined to the gas phase.   Initial pressure and velocity field is evaluated using the inlet mass flux.

4.3.8   Pore diffusion model inside the washcoat layer

As mentioned before, in the ATM model, gaseous reactants are assumed to be transferred onto the converter surface across the boundary layer, and further transported through and into washcoat layer by pore diffusion phenomena.   The mass and heat transfer from main gas flow to the converter surface through the boundary layer is modeled by Sieder/Tate equation based on the Graetz number for laminar flow in narrow channel (Perry, Green and Southard, 2018; Sieder and Tate 1936).   In the washcoat layer, diffusive transfer inside the washcoat layer is considered only in y-direction (not for z-direction) as shown in Fig. 4.2(B).   The heat conduction in washcoat and cordierite are also considered with the assumption that the temperature of washcoat layer is uniform in y-direction.

The balance equation for species k inside the washcoat layer is given by

$$\varepsilon_{wcl} \cdot \frac{\partial\left(\rho^L \cdot w_k^L\right)}{\partial t} = \frac{\partial}{\partial y}\left(D_{k,eff} \cdot \rho^L \cdot \frac{\partial\left(w_k^L\right)}{\partial y}\right) + MG_{k,g} \cdot \sum_i^I v_{i,k} \cdot \bar{r}_i(c_k^L, T_s) \quad (4.33)$$

where ε_{wcl} is the porosity of the washcoat layer, ρ^L is the density of the gas mixture in

the washcoat layer and $D_{k,eff}$ is the effective diffusion coefficient.

To determine the effective diffusion coefficient, $D_{k,eff}$, transport model is used and, in this study, parallel pore diffusion model is adopted (Sasmaz et al., 2017) for the mass transfer inside the washcoat layer (Hayes et al., 2000; Mladenov et al., 2010), and is as follows,

$$\frac{1}{D_{k,eff}} = \frac{\tau_{wcl}}{\varepsilon_{wcl}} \left(\frac{1}{D_{k,g}} + \frac{1}{D_{Kn}} \right) \tag{4.34}$$

In the model, parallel phenomena of transport effects of pure gas phase and Knudsen diffusion is considered, where D_{Kn} is the Knuden diffusion coefficient depending on the pore diameter, d_{pore}, molar mass of the specific species, M_k, and surface temperature, T_s and is described by the following equation,

$$D_{Kn} = \frac{1}{3} d_{pore} \sqrt{\frac{8RT_s}{\pi M_k}} \tag{4.35}$$

where τ_{wcl} is the tortuosity of the washcoat layer.

In this study, the pore diameter and mean pore volume of washcoat layer are identified by the liquid nitrogen porosimetry as 13.9 nm and 0.955×10^{-3} kg/m^3, respectively. Using the values, porosity of the washcoat is obtained to be 0.590 as shown in Table 2.1. Accordingly, tortuosity is set to be 1.70 due to their reciprocal relation for parallel pore diffusion model (Hayes et al., 2000).

Boundary condition at the solid surface (y = 0) is determined by the balance of diffusion flux and mass transfer through the boundary layer from the bulk gas phase to the solid surface and vice versa and is described as follows,

$$\text{at y = 0,} \qquad D_{k,eff} \cdot \rho^L \cdot \frac{\partial(w_k^L)}{\partial y} = k_{k,m} \cdot \left(\rho^L \cdot w_k^L - \rho^B \cdot w_k^B \right) \tag{4.36}$$

where w_k^B is the mass fraction of the species in the bulk gas.
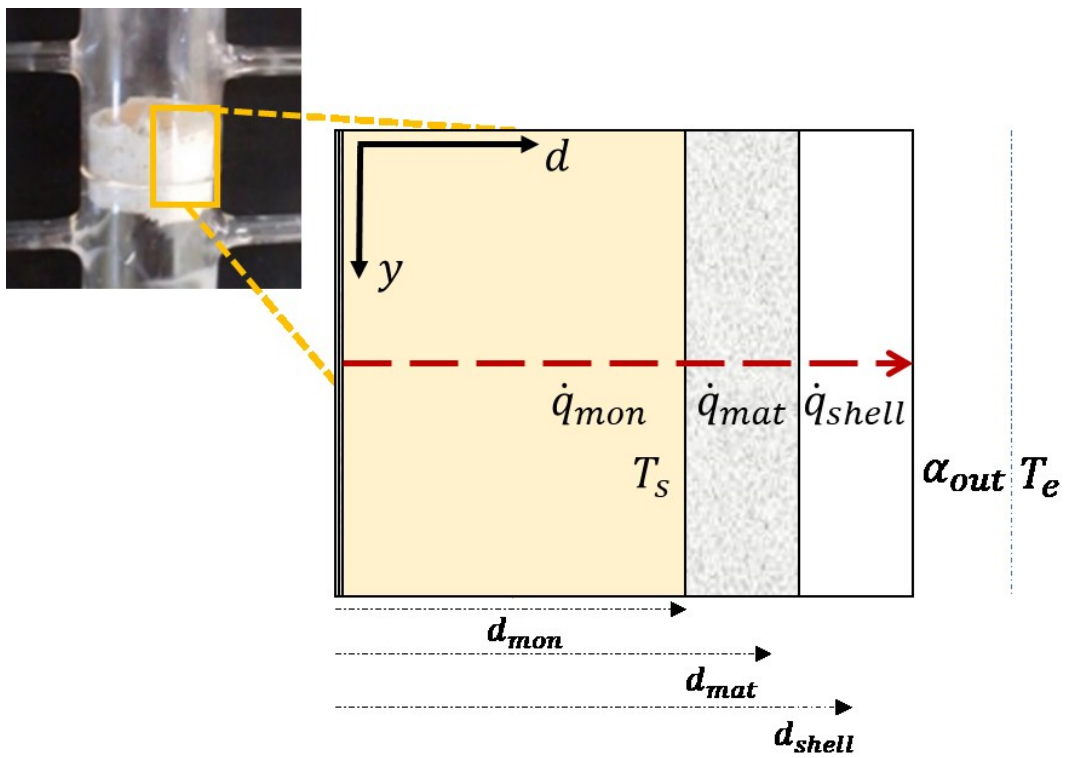
Fig. 4.3   Illustration of the heat insulation in the experiment and schematic of heat loss phenomena from the monolith catalyst to the surroundings

4.3.9   Chemical reaction rate calculation

Generally, a chemical reaction can be expressed as follows (Coltrin, Kee and Rupley, 1996),

$$\sum_{k=1}^{K} v'_{ki}\,\kappa_k \Leftrightarrow \sum_{k=1}^{K} v''_{ki}\,\kappa_k \quad (i = 1, \dots, I) \tag{4.37}$$
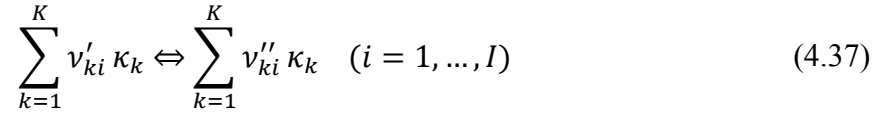
where v is the stoichiometric coefficient of species k, and κ is the chemical symbol of the kth species while K is the total number of gas phase species and surface phase species in the system and I is the total number of chemical reactions considered.

Stoichiometric coefficient of species k in reaction i is defined as follows,

$$v_{ki} = v'_{ki} - v''_{ki} \tag{4.38}$$

Production rate of k species is defined as follows,

$$\dot{r}_k = \sum_{i=1}^{I} v_{ki}\,\dot{q}_i \tag{4.39}$$

Reaction rate, $\dot{q}_i$, of reaction i is defined as follows,

$$\dot{q}_i = k_{fi} \prod_{k=1}^{K} \left[c_{k,g}\right]^{Fo_{ki}} - k_{r_i} \prod_{k=1}^{K} \left[c_{k,g}\right]^{Ro_{ki}} \tag{4.40}$$

Exponents of concentration of the gas phase species in rection i for forward and backward reaction are Fo_{ki} and Ro_{ki}, and are same as the stoichiometric coefficients v'_{ki} and v''_{ki} for elementary reactions.

Assuming as ideal gas, concentration of gas phase species, $c_{k,g}$ is defined as follows:

$$c_{k,g} = y_{k,g} \frac{p_g}{RT_g} \tag{4.42}$$

Species concentration on the surface is defined as follows,

$$c_{k,g} = \theta_k \Theta \tag{4.42}$$

where θ_k is the fraction of species k, and Θ is site density of the metal, in this study, Pt.

Forward reaction rate constant expression for adsorption reactions is defined as follows,

$$k_{f_i} = \frac{\gamma_i}{(\Gamma_{tot})^m} \sqrt{\frac{RT}{2\pi M_{k,g}}} \tag{4.42}$$

where $M_{k,g}$ is the molecular weight of the gas phase species, Γ_{tot} is the total surface site concentration, m is the sum of all the stoichiometric coefficients of reactant surface species, and γ_i is the sticking coefficient which is the probability of adsorption of a molecule on the surface when a collision occurs and it is defined as follows,

$$\gamma_i = min\left[1, A_i T^{b_i} exp\left(-\frac{E_i}{RT}\right)\right] \tag{4.43}$$

where A_i, b_i, E_i are the Arrhenius parameters and here, A_i and b_i are dimensionless while the unit of E_i is in kJ/(kmol·K).

Forward reaction rate constant expression for surface reactions between adsorbed surface species is defined as the modified Arrhenius expression which include the coverage parameters considerations and is as follows,

$$k_{f_i} = A_i T^{b_i} exp\left(-\frac{E_i}{RT}\right) \prod_{k=1}^{K_{stor}} \left(10^{\eta_{ki}\theta_k} (\theta_k)^{\mu_{ki}} exp\left(-\frac{\varepsilon_{ki}\theta_k}{RT}\right)\right) \qquad (4.44)$$

where η_{ki}, μ_{ki}, ε_{ki} are the three coverage parameters for the surface site species k, and the reaction i. These parameter values are available from the literature and $\prod$-term enhances the Arrhenius expression so that the preexponential factor A and the activation energy E can be defined as follows,

$$\log_{10} A = \log_{10} A_i + \sum_{k=1}^{K_{stor}} \eta_{ki}\theta_k \qquad (4.45)$$

$$E = E_i + \sum_{k=1}^{K_{stor}} \varepsilon_{ki}\theta_k \qquad (4.46)$$

Forward reaction rate constant expression for desorption reactions from the surface is defined as the Arrhenius expression and is as follows,

$$k_{f_i} = A_i T^{b_i} exp\left(-\frac{E_i}{RT}\right) \qquad (4.47)$$

For irreversible reactions, the backward rate constant k_{r_i} is defined as zero. However, in this study, all of the reaction from the adsorption step to the desorption steps are considered as reversible reactions. For reversible reactions, the backward reaction rate is evaluated from the equilibrium constant and as follows,

$$k_{r_i} = \frac{k_{f_i}}{K_{c_i}} \qquad (4.48)$$

where K_{c_i} is the equilibrium constant in concentration units for reaction i.

K_{c_i} can be obtained from K_{p_i} from the following expression,

$$K_{c_i} = \left(\frac{p_g}{RT_g}\right)^{\sum_{k=1}^{K_{gas}} v_{ki}} \cdot \Theta^{\sum_{k=1}^{K_{stor}} v_{ki}} \cdot K_{p_i} \tag{4.49}$$

where if there is no adsorbed species, the site density term becomes unity.

Equilibrium constant K_{p_i} is obtained from the standard state Gibbs free energy of formation and is defined as follows,

$$K_{p_i} = e^{\left(\frac{\Delta S_i}{R} - \frac{\Delta H_i}{RT}\right)} \tag{4.50}$$

where the entropy and enthalpy terms of species k for reaction i is defined as follows,

$$\frac{\Delta S_i}{R} = \sum_{k=1}^{K} v_{ki} \frac{S_k}{R} \tag{4.51}$$

$$\frac{\Delta H_i}{RT} = \sum_{k=1}^{K} v_{ki} \frac{H_k}{RT} \tag{4.52}$$

The additional equations included in the numerical model are as follows. Reaction rates are modified as in the experiments since the noble metals responsible for the surface catalytic reactions are distributed in the porous washcoat layer. The total surface area of noble metal, A_{PGM} is estimated as follows,

$$A_{PGM} = \frac{\gamma_{cat} \cdot W_{PGM}}{M_{PGM} \cdot \Gamma_{tot}} \cdot V \tag{4.53}$$

where γ_{cat} is the metal dispersion, V is the volume of computational cell, and M_{PGM} is the molar mass, respectively.　In the numerical simulation studies, experimentally obtained metal dispersion shown in Table 2.1. is used.

The species consumption and creation rate per unit PGM area, $\bar{r}$, is the function of the rate constant of surface elementary reactions which are described before. Converter (monolith) volume-based species consumption and creation rate which is included in eq.(4.15), (4.16) and (4.17) can be obtained by the following equation,

$$\dot{r} = \frac{A_{PGM}}{V_{conv}}\bar{r} \tag{4.54}$$

where V_{conv} is the converter (monolith's) volume.

4.3.10　Kinetic parameter estimation

As for the reaction mechanism, the proposed reaction mechanism, which includes 38 elementary-step reactions with 15 surface species and 7 gaseous species, discussed in the previous chapter is used.　As for the kinetic parameter estimation, literature studies are used as reference and based values.　The estimation of kinetic parameters is systematically performed by fitting the experimental results.

First, CO-O_2 reaction parameters are fixed by the respective experimental results and the results are extensively discussed in our study (Shimokuri et al., 2020).　In the study, by using the developed detailed CO / O_2 surface reaction mechanism, not only the variations of CO to CO_2 conversion rates with temperature are quantitatively reproduced for various O_2 concentration, but also CO conversion rates on bimetal catalysts agree quantitatively with experimental results for various metal ratios as well as gas mixture ratios.　The CO / O_2 surface reaction mechanism is developed from the aspects of thermodynamic consistency.

The same principle is applied in this study.　CO / H_2 / O_2 surface reaction is developed in the same manner and the kinetic parameters are used as based values in this study.　As for the kinetic parameters such as initial sticking coefficient of adsorption and activation energy of desorption for C_3H_6 is based on the previous studies (Koop and Deutschmann, 2009; Kota et al., 2017) and those for C_2H_4 are based on the heterogeneous ignition study (Perger et al., 2005).　Finally, all reaction parameters are tuned from the aspect of thermodynamic consistency.

4.4 Thermodynamic Consistency

In the development of a detailed surface reaction mechanism, an important major issue often overlooked is thermodynamic consistency. Enthalpic and entropic inconsistency distorts the underlying equilibrium constant (Mhadeshwar et al., 2003). The lack of thermochemical data for surface species is the major issue.

For an individual reaction, enthalpic and entropic consistency can be easily satisfied, however, it is difficult for the entire reaction mechanism. Being state functions, linear combination of enthalpy and entropy functions of elementary reactions must obey the same consistency level of the global reaction and that principle is used in this study.

In this study, thermodynamic consistency is applied for the kinetic parameter fitting as the same manner as Stotz et.al (Stotz et al., 2017). For the proposed surface elementary reactions, enthalpy and entropic constraints are defined as follows,

$$\Delta_R H_i = E_{f,i} - E_{r,i} \tag{4.55}$$

$$\Delta_R S_i = R \cdot ln\left(\frac{A_{f,i}}{A_{r,i}} \cdot \frac{1}{Q_i^0}\right) \tag{4.56}$$

where Q_i^0 is the reaction quotient evaluated at reference concentration and is as follows,

$$Q_i^0 = \prod_i [c_k^0]^{v_{ki}'' - v_{ki}'} \tag{4.57}$$

where c_k^0 is the reference concentration which depend on the type of the species.

For gas species,

$$c_k^0 = \frac{p_0}{RT} \tag{4.58}$$

where p_0 is the standard state pressure.

For surface species,

$$c_k^0 = \frac{\Gamma_{tot}}{\sigma_k} \qquad (4.59)$$

where σ_k is the number of surface sites occupied by species k.

Kinetic parameters with thermodynamics in Gibbs free energy, $\Delta_R G_i$, of the reaction step, k, is as follows,

$$\Delta_R G_i = \left(E_{f,i} - E_{r,i}\right) - RT \cdot ln\left(\frac{A_{f,i}}{A_{r,i}} \cdot \frac{1}{Q_i^0}\right) \qquad (4.60)$$

Equation 4.60 is basically the same as the derived form of equation 4.48 without the consideration of surface coverage parameters of adsorbed species. Also, surface coverage parameters of adsorbed species are ignored in the thermodynamic consistency calculation of kinetic parameter estimation process.

Thermochemical data for the calculations of Gibbs free energies of the global reactions are referred from Chase and Chao et.al. (Chao and Zwolinski, 1975; Chase, 1998).

4.5   Conclusions

In this chapter, numerical modelling method used in this study is explained in detail together with illustrations and equations.   "Aftertreatment model" (ATM model) of BOOST^{TM} (AVL Corp.), in which a single cell of monolith honeycomb reactor can be modelled in not only gas flow along the channel but also into the washcoat layer, is used.

In the ATM model, essential tools for numerical modelling of a heterogenous catalytic reaction are applied as follows,

1. Gaseous reactants are assumed to be transferred onto the converter surface across the boundary layer, and further transported through and into the washcoat layer by pore diffusion phenomena.

2. Mass and heat transfer from main gas flow to the converter surface through the boundary layer is modeled by Sieder/Tate equation based on the Graetz number for laminar flow in narrow channel

3. Parallel pore diffusion model is adopted for the mass transfer inside the washcoat, and the parameters needed for the pore diffusion model are investigated by the liquid nitrogen porosimetry.

4. Rate constants of surface elementary reactions are in the form of sticking coefficient formulation for the adsorption reactions, while in the form of the Arrhenius and modified Arrhenius expression for other reactions.

5. Thermodynamic consistency is applied for the kinetic parameter estimation and the based values of the parameters are referred from well-developed detailed surface reaction mechanisms.

Chapter 5

Numerical Studies

5.1   Introduction

In this chapter, first, the procedure of kinetic parameter estimation for the proposed detailed surface reaction mechanism is presented, and then, the numerical simulation results carried out by using numerical modelling method presented in the previous chapter and the developed surface reaction mechanism, are discussed.   As for numerical studies, conversion results as well as surface coverage results are discussed. Lastly, the developed detailed surface reaction mechanism is validated by the multiple gas compositions, and their conversion and coverage are discussed.

Numerical calculations are done by using the gas temperatures before the catalyst as in the experiments.   Numerically calculated results are exported as time series data at each calculation temperature and an example is as shown in Fig. 5.1.   In Fig. 5.1, numerical calculation results for the experimental condition of 3000 ppm of CO and 1500 ppm of O_2 at different calculation temperatures are shown.   Here, horizontal axis is the calculation time in second and vertical axis is the CO conversion.   Steady state conversion results are extracted at the same measurement time seconds as they are in the gas phase conversion experiments, which is usually within 5 minutes.   Numerically calculated conversion results are presented as steady state results and all of the gas temperatures in the horizontal axis represent gas temperatures before the catalyst in the following sections.

5.2   Development of the detailed surface reaction mechanism

5.2.1   CO / O_2 surface reaction mechanism

The procedure of development of CO / O_2 surface reaction mechanism is widely discussed in our study (Shimokuri et al., 2020).   Firstly, kinetic parameters from the previous detailed surface reaction studies are used as reference values (Koop and Deutschmann, 2009; Kota et al., 2017).   It is reliable that kinetic parameters were based on the literature studies, and thermodynamic consistency was considered in their

development process so that the use of their kinetic parameter as a starting point is a reasonable idea.   Then by using the gas phase conversion experiments, kinetic parameters are carefully fitted and tuned to be thermodynamically consistent. Experimental conditions used to develop CO / O_2 surface reaction mechanism on Pt/Al$_2$O$_3$ monolith catalyst are nearly the same as the conditions used in this study as shown in Table 2.3.   3000 ppm of CO is fixed for all experimental conditions and for oxygen concentration, 1500 ppm is used as stoichiometric condition, 3000 ppm and 10000 ppm as fuel lean (O_2 excess) conditions.   Comparison between the experimental results and numerical calculation results are shown in Fig. 5.2.   In Fig. 5.2, points represent the experimental results and dashed lines represent the numerical results.   It can be seen that the numerical results quantitatively reproduce the experimental conversion rates from light-off to 100 % conversion.   Moreover, it is validated by experimental results of bimetal catalyst and agree well.

5.2.2   CO / H$_2$ / O$_2$ surface reaction mechanism

As a next step, detailed CO / H$_2$ / O$_2$ surface reaction mechanism is developed. Kinetic parameters from the CO / O$_2$ surface mechanism and previous detailed surface reaction studies are used as reference values (Koop and Deutschmann, 2009; Kota et al., 2017).   Using the gas phase conversion experiments, kinetic parameters are carefully fitted and tuned to be thermodynamically consistent.   Experimental condition used to develop CO / H$_2$ / O$_2$ surface reaction mechanism on Pt/Al$_2$O$_3$ monolith catalyst is the stoichiometric condition in which 3000 ppm of CO, 3000 ppm of H$_2$ and 3000 ppm of O$_2$ contained.   Comparison between the experimental results and numerical calculation results are shown in Fig. 5.3.   In Fig. 5.3, points represent the experimental results and dashed lines represent the numerical results.   It can be seen that numerical results quantitatively reproduce the experimental conversion rates from light-off to 100 % conversion rates for both CO and H$_2$.   Moreover, it is validated by the experimental condition of 500 ppm CO, 3000 ppm of H$_2$ and 1500 ppm of O$_2$ and results are shown in Fig. 5.4.   In Fig. 5.4, points represent the experimental results and dashed lines represent the numerical results.   It can be seen that numerical calculation results agree well with the experimental results for both CO and H$_2$.
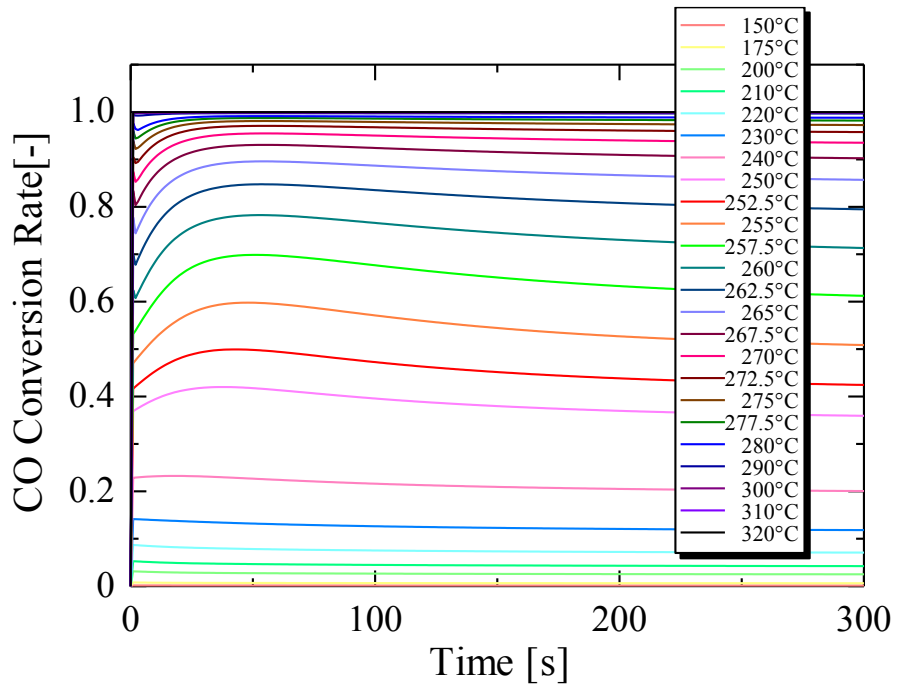
Fig. 5.1   Temporal profiles of CO conversion for experimental condition of 3000 ppm CO and 1500 ppm O_2 at different calculation temperatures
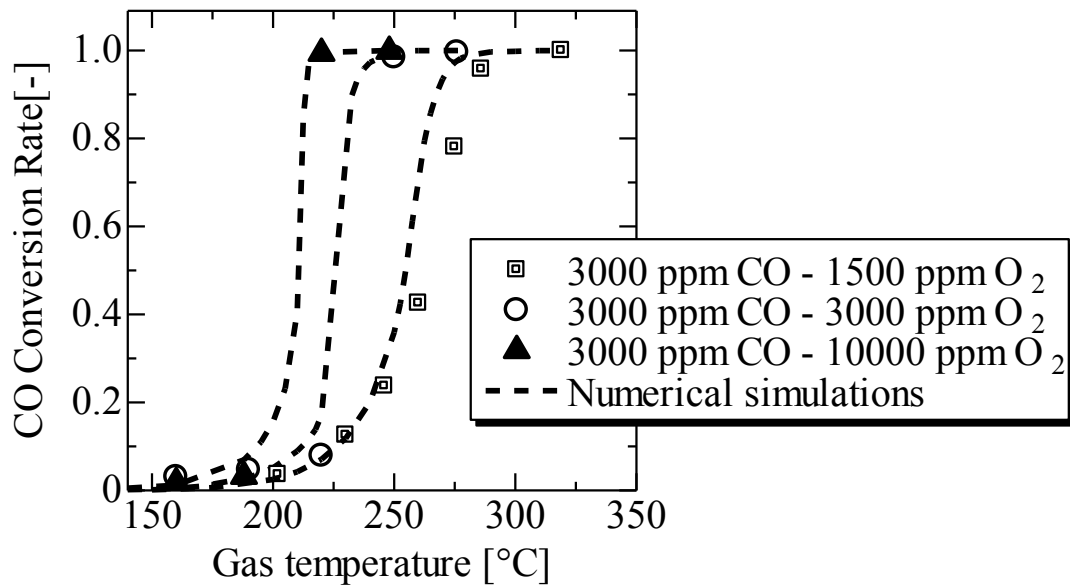
Fig. 5.2   Comparison between experimental results and numerical results of CO / O_2 oxidation for different oxygen concentrations
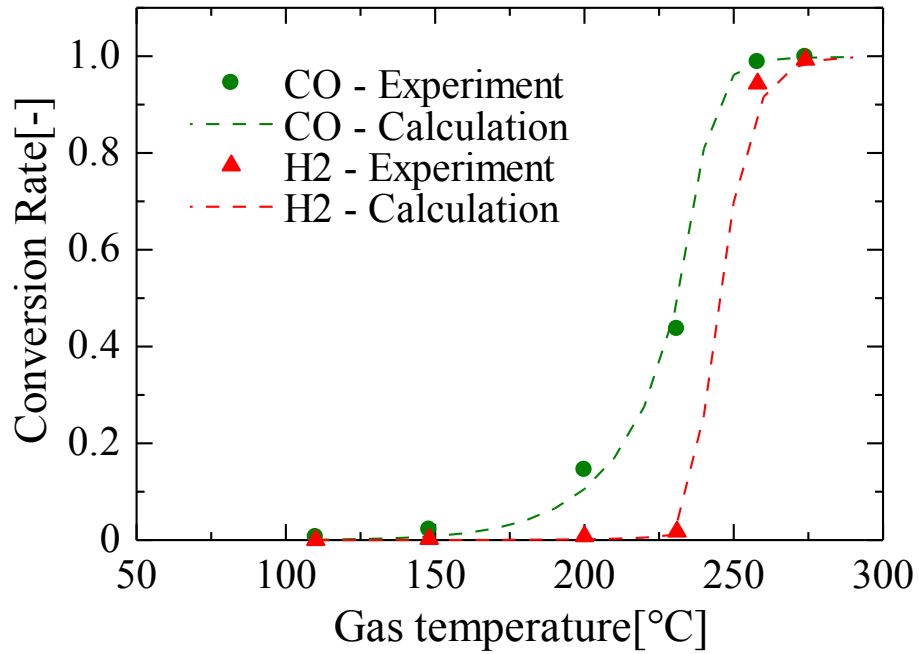
Fig. 5.3   Comparison between experimental results and numerical results for the
condition of 3000 ppm CO, 3000 ppm H_2 and 3000 ppm O_2
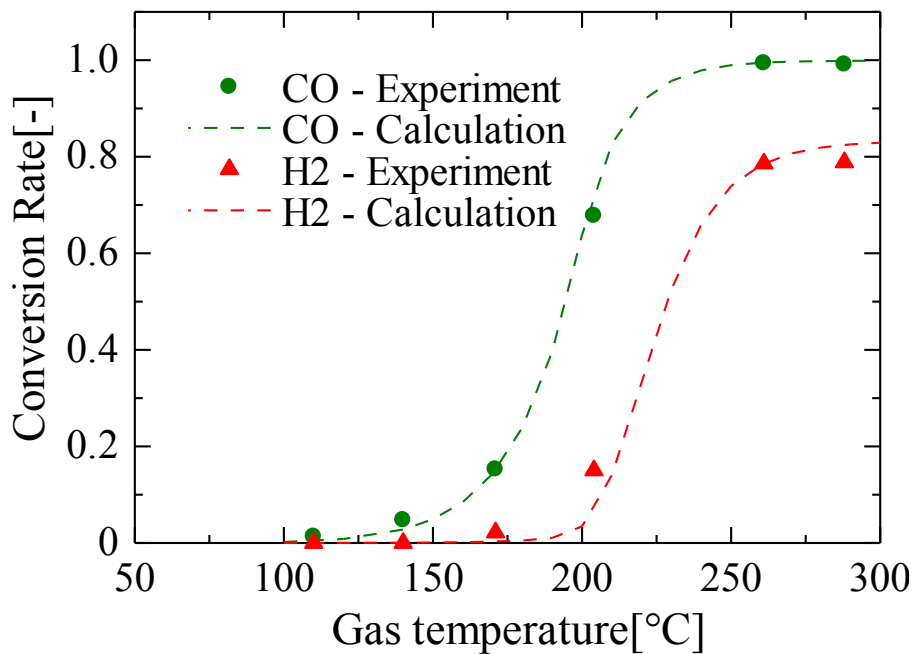
Fig. 5.4   Comparison between experimental results and numerical results for the
condition of 500 ppm CO, 3000 ppm H_2 and 1500 ppm O_2

5.2.3 C_2H_4 / O_2 and C_3H_6 / O_2 surface reaction mechanism

C_2H_4 and C_3H_6 oxidation parameters are fixed by fitting the C_2H_4 / O_2 / N_2 and C_3H_6 / O_2 / N_2 stoichiometric conditions (Case I & V in Table 2.3) of gas phase conversion experimental results. Kinetic parameters such as initial sticking coefficient of adsorption and activation energy of desorption for C_3H_6 is based on the previous studies (Chatterjee et al., 2001; Koop and Deutschmann, 2009; Kota et al., 2017) and those for C_2H_4 are based on the heterogeneous ignition study (Perger et al., 2005). Finally, all reaction parameters are tuned from the aspect of thermodynamic consistency.

Table A.1 shows the proposed detailed surface reaction mechanism with kinetic parameters and is shown in the appendix section. Here, it is worth to note and found that the low temperature light-off performance is controlled by the kinetic properties and the high temperature light-off performance is controlled by the transport properties of pore diffusion. This fact is consistent with previous studies reported the importance of the intraparticle diffusion limitations (Hayes et al., 2000; Karadeniz et al., 2013; Mladenov et al., 2010; Sharma et al., 1991). In the low temperature conditions, catalytic reaction rates are slow, i.e., "reaction limiting". On the other hand, in high temperature conditions, catalytic reaction rate is enough high and therefore, transport of reactants onto the catalytic metal surface limits the conversion, i.e., "diffusion limiting". Hence, careful choice and parameter identification of pore diffusion model are important for the modelling of monolith honeycomb catalyst with washcoat.

Representative free energy diagrams of C_2H_4 / O_2 / N_2 at 250 °C and C_3H_6 / O_2 / N_2 at 250 °C for the stoichiometric conditions (Case I & V in Table 2.3), obtained by same manner as Stotz (Stotz et al. 2017), are given in Fig. 5.5. Vertical axis is the variation of free energy ($\Delta_R G_i$) and horizontal axis is the reaction progress. The initial states for Pt with respect to the free energy of $C_2H_4(g)$ or $C_3H_6(g)$ in Fig. 5.5(A) or Fig. 5.5(B) is defined as the clean Pt(S) surface with 1 mole of $C_2H_4(g)$ and 3 mole of $O_2(g)$ or 1 mole of $C_3H_6(g)$ and 4.5 mole of $O_2(g)$ in the gas phase. The thermodynamically obtained $\Delta_R G_i$ values (Chao and Zwolinski 1975) to form all of the $CO_2(g)$ and $H_2O(g)$ from $C_2H_4(g)$ is -1306 kJ/mol while $C_3H_6(g)$ is -1937 kJ/mol.

In both Fig. 5.5(A) and Fig. 5.5(B), $\Delta_R G_i$ increases at the initial adsorption step, however, decreases to form the intermediate species and final product species. Here, at the intermediate steps, $\Delta_R G_i$ is calculated as the formation of corresponding intermediate species, and if $CO_2(S)$ and $H_2O(S)$ are formed during these steps, $\Delta_R G_i$ for the desorption of the gas phase $CO_2(g)$ and $H_2O(g)$ are included. In both Fig. 5.5(A) and Fig. 5.5(B), it can be observed that decrease in $\Delta_R G_i$ is greater for the reactions in

which more active surface Pt(S) site occupations are occurred than for those without any more Pt(S) site occupation, for example, from C_2H_4 (2S) to C_2H_3(3S) ((i) in Fig. 5.5(A)), and from C_3H_6(2S) to C_3H_5(3S) and from C_3H_5(3s) to C_3H_4(3S) ((ii) and (iii) in Fig. 5.5(B)). Moreover, $\Delta_R G_i$ for the formation of C_2H_3(3S), which is the same intermediate species for both C_2H_4 and C_3H_6 proposed in this study, for C_2H_4/O_2 system is -523 kJ/mol while for C_3H_6/O_2 system is -1189 kJ/mol. This fact indicates that the conversion of C_2H_4 on Pt/Al_2O_3 may be inhibited by the presence of C_3H_6 in the system, which will be discussed in the following section.

5.2.4   Numerically calculated conversion rates

Comparison between numerical simulation results and experimental results for the conditions as shown in Table 2.3 are shown in Fig. 5.6. Experimental results are represented by the points and simulation results are represented by the dashed lines for their respective conditions. It is investigated that not only C_2H_4 conversion (Fig. 5.6(A)) but also C_3H_6 conversion (Fig. 5.6(B)) is limited by the kinetics at lower temperature conditions while the conversion at high temperature conditions is limited by the transport properties of diffusion into the washcoat. It can be observed that both light-off temperature and complete conversion temperature range from the numerical simulations have a good agreement with the experimental results.

5.2.5   Numerically calculated surface species profiles

Numerically simulated surface species profiles of C_2H_4 / O_2 / N_2 and C_3H_6 / O_2 / N_2 are shown in figures from Fig. 5.7 to Fig. 5.14. For the purpose of better understanding, experimental and numerically calculated gas concentration at the downstream of the catalyst are shown together with surface species profiles. In these figures, horizontal axis is the gas temperature before the catalyst and vertical axis for upper part is gas concentration in ppm and lower part is the surface coverage fraction. Experimental gas concentrations are shown as color-coded points and numerically calculated gas concentrations are shown as color-coded dashed lines, in which red for $C_2H_{4(g)}$, $C_3H_{6(g)}$ and green for CO_2(g). Only C_2H_4(g), C_3H_6(g) and CO_2(g) are presented to observe the clear conversion of HC to CO_2 together with surface species variations. Single Pt sited species are referred as S and multiple Pt sited species are referred as 2S or 3S. Same interpretation method is used for all figures presented in the following sections.
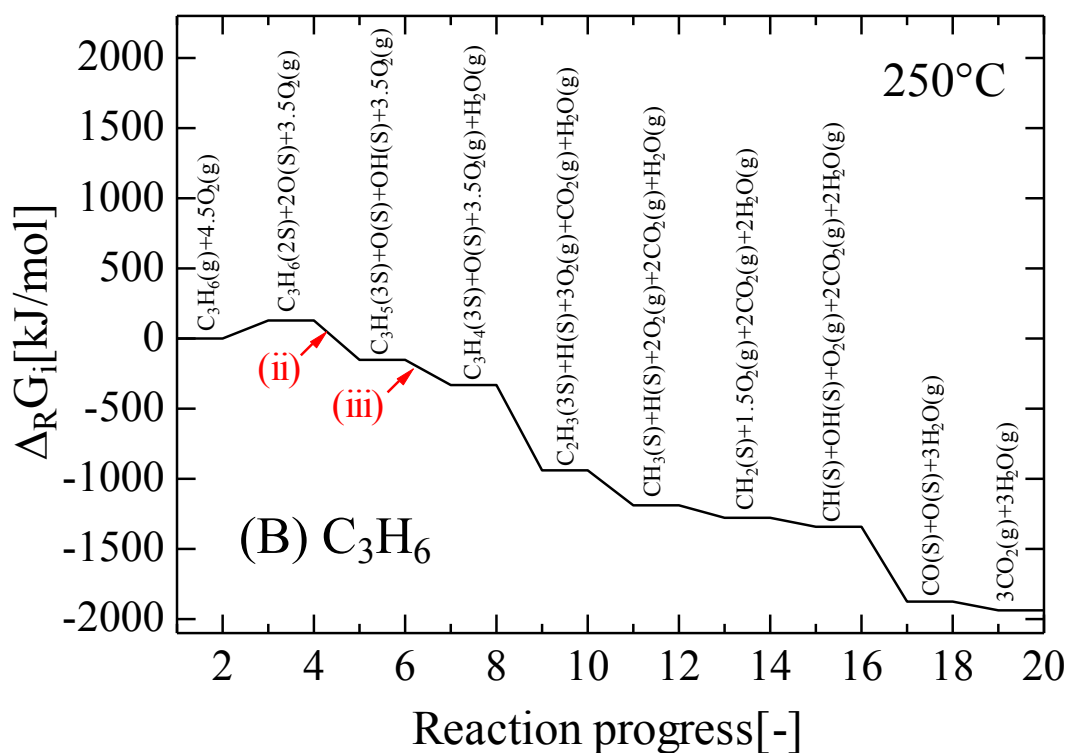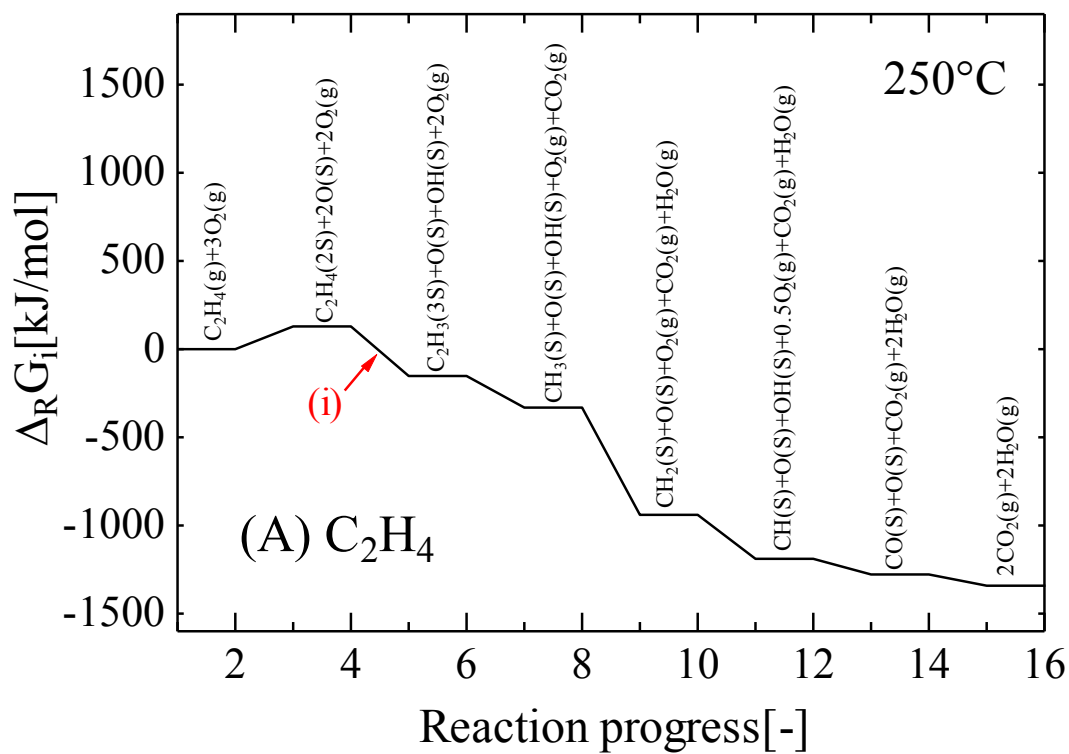
Fig. 5.5   Free energy diagrams of proposed reaction mechanism
(A) C_2H_4 / O_2 at 250°C, (B) C_3H_6 / O_2 at 250°C
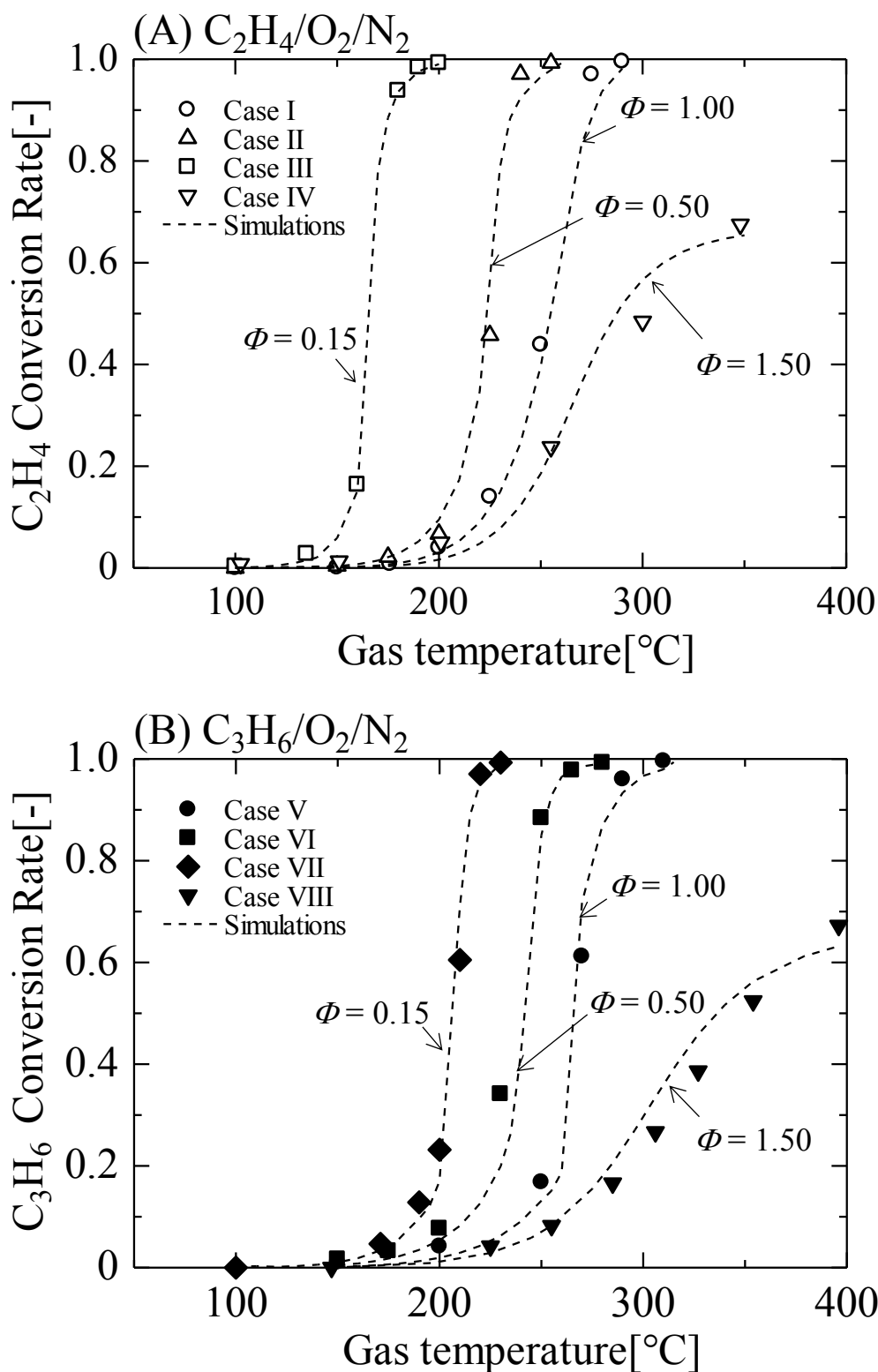
Fig. 5.6   Comparison between experimental and numerical results for different O_2 concentrations (A) C_2H_4 (Case I, II, III & IV in Table.2.3), (B) C_3H_6 (Case V, VI, VII & VIII in Table.2.3)

In Fig. 5.7, numerically calculated surface species profiles of C_2H_4 / O_2 / N_2 for fuel rich condition (Case IV in Table. 2.3) are shown and, it can be observed that surface is mostly covered by three Pt sited $C_2H_3(3S)$ species and, even though the light-off temperature, 250 °C, is reached, there is less space on the surface for $O_2(g)$ species to be dissociatively adsorbed and procced the oxidation reactions.   Therefore, the oxidation reaction rates are slow, and the maximum conversion temperature range become significantly wider than other conditions.   The similar behavior can be observed in Fig. 5.11 which shows the surface species profiles of C_3H_6 / O_2 / N_2 for fuel rich condition (Case VIII in Table. 2.3).   It is due to the higher sticking probabilities of $C_2H_4(g)$ and $C_3H_6(g)$, and lower probability of $O_2(g)$.   Since the gas species are competitively diffuse into the washcoat layer, for HC species, they can stick on the surface faster than $O_2(g)$ so that the active Pt surface sites are occupied by the stable intermediate species, here by $C_2H_3(3S)$ species.

In Fig. 5.8 and Fig. 5.12, surface species profiles for stoichiometric conditions (Case I and V in Table. 2.3) are shown and in the low temperature regions, surface is also mostly covered by the multiple Pt sited $C_2H_3(3S)$ species.   However, as soon as the light-off temperature is achieved, 230 °C for Case I and 250 °C Case V, $O_2(g)$ can adsorb on the surface and oxidation reactions can be proceeded, therefore, conversion of HC to CO_2 become considerably faster than fuel rich conditions.   For every 1 mole of $C_2H_3(3S)$ species decomposition, 3 moles of Pt(S) are free, and reactions can be carried out effectively on the surface.   This behavior can be clearly observed in both Fig. 5.8 and Fig. 5.12 because the surface coverage of O(S), OH(S), $CO_2(S)$ and Pt(S) drastically increase with the increase in temperature and decrease in $C_2H_3(3S)$ surface coverage.

This can explain why the conversion process increase sharply for higher oxygen concentration conditions.   For fuel lean (O_2 excess conditions), significant increase in the surface coverage of O(S) is observed from the low temperature regions before light-off temperature and such a presence of O(S) can promote the oxidation process.   On the other hand, higher surface coverage of Pt(S), i.e., higher number of free Pt surface site, during the oxidation process can make faster conversion, i.e., earlier light-off of HC species.   Such kind of behavior can be clearly observed in this study because surface coverage of Pt(S) for stoichiometric conditions of C_2H_4 and C_3H_6 are 0.28 and 0.22 at the same temperature of 290 °C, respectively.   Same behavior is observed for fuel lean conditions such as for the same 3000 ppm O_2 conditions, surface coverage of Pt(S) is 0.1 for C_2H_4 and 0.067 for C_3H_6 at 250 °C, and for 10000 ppm conditions, it is 0.026 for C_2H_4 and 0.002 for C_3H_6 at 200 °C, respectively.   This fact can explain why C_2H_4 has higher reactivity than C_3H_6 for same oxygen concentration conditions.

Fig. 5.7   Experimental and numerical results of gas phase C_2H_4 and CO_2 at downstream of catalyst, and simulated surface species profiles for fuel rich condition (500 ppm C_2H_4 and 1000 ppm O_2, Case IV in Table. 2.3)

Fig. 5.8　Experimental and numerical results of gas phase C_2H_4 and CO_2 at downstream of catalyst, and simulated surface species profiles for stoichiometric condition (500 ppm C_2H_4 and 1500 ppm O_2, Case I in Table. 2.3)

Fig. 5.9   Experimental and numerical results of gas phase C_2H_4 and CO_2 at downstream of catalyst, and simulated surface species profiles for fuel lean (O_2 excess) condition (500 ppm C_2H_4 and 3000 ppm O_2, Case II in Table. 2.3)

Fig. 5.10 Experimental and numerical results of gas phase C_2H_4 and CO_2 at downstream of catalyst, and simulated surface species profiles for fuel lean (O_2 excess) condition (500 ppm C_2H_4 and 10000 ppm O_2, Case III in Table. 2.3)
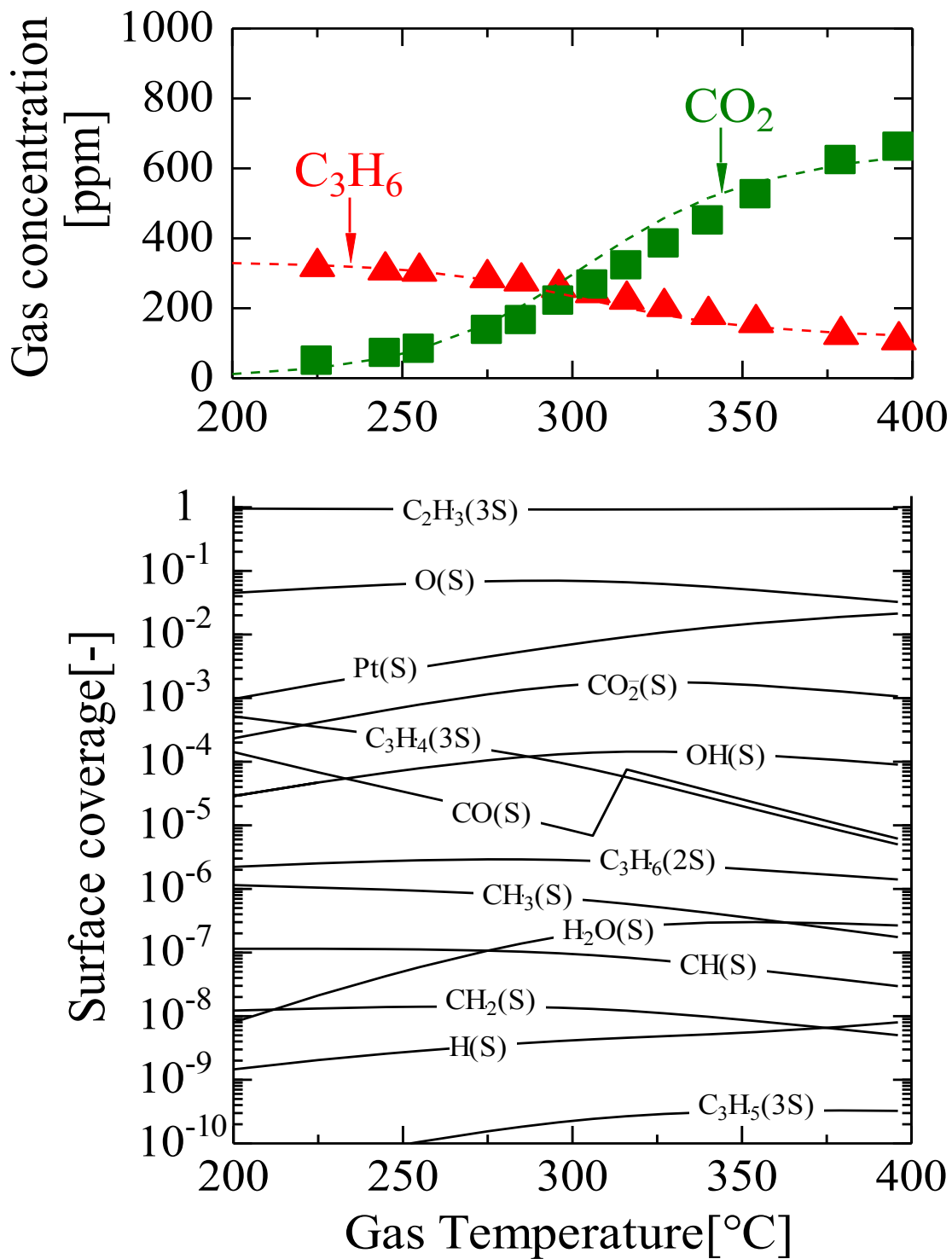
Fig. 5.11 Experimental and numerical results of gas phase C_3H_6 and CO_2 at downstream of catalyst, and simulated surface species profiles for fuel rich condition (333 ppm C_3H_6 and 1000 ppm O_2, Case VIII in Table. 2.3)
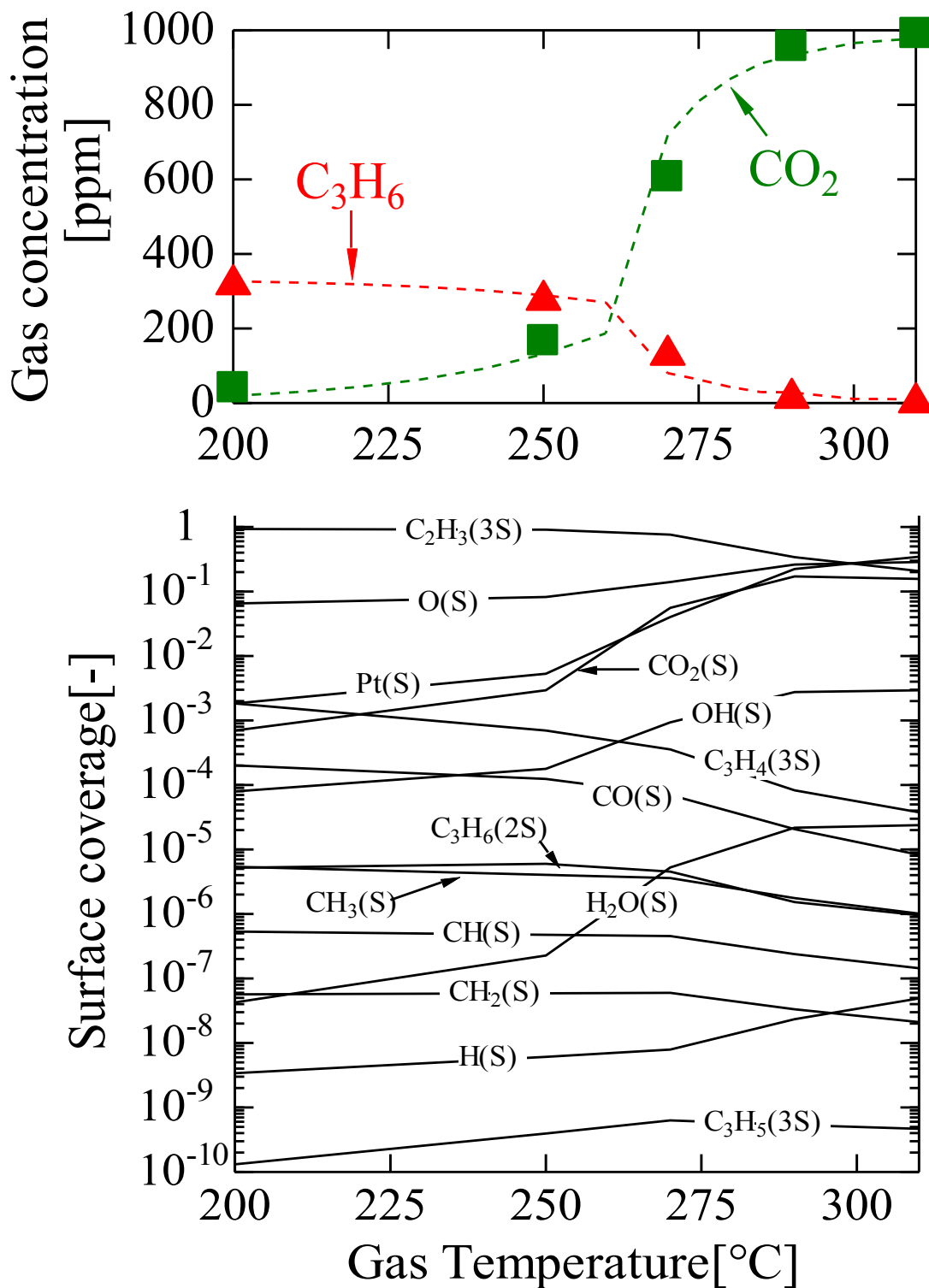
Fig. 5.12 Experimental and numerical results of gas phase C_3H_6 and CO_2 at downstream of catalyst, and simulated surface species profiles for stoichiometric condition (333 ppm C_3H_6 and 1500 ppm O_2, Case V in Table. 2.3)
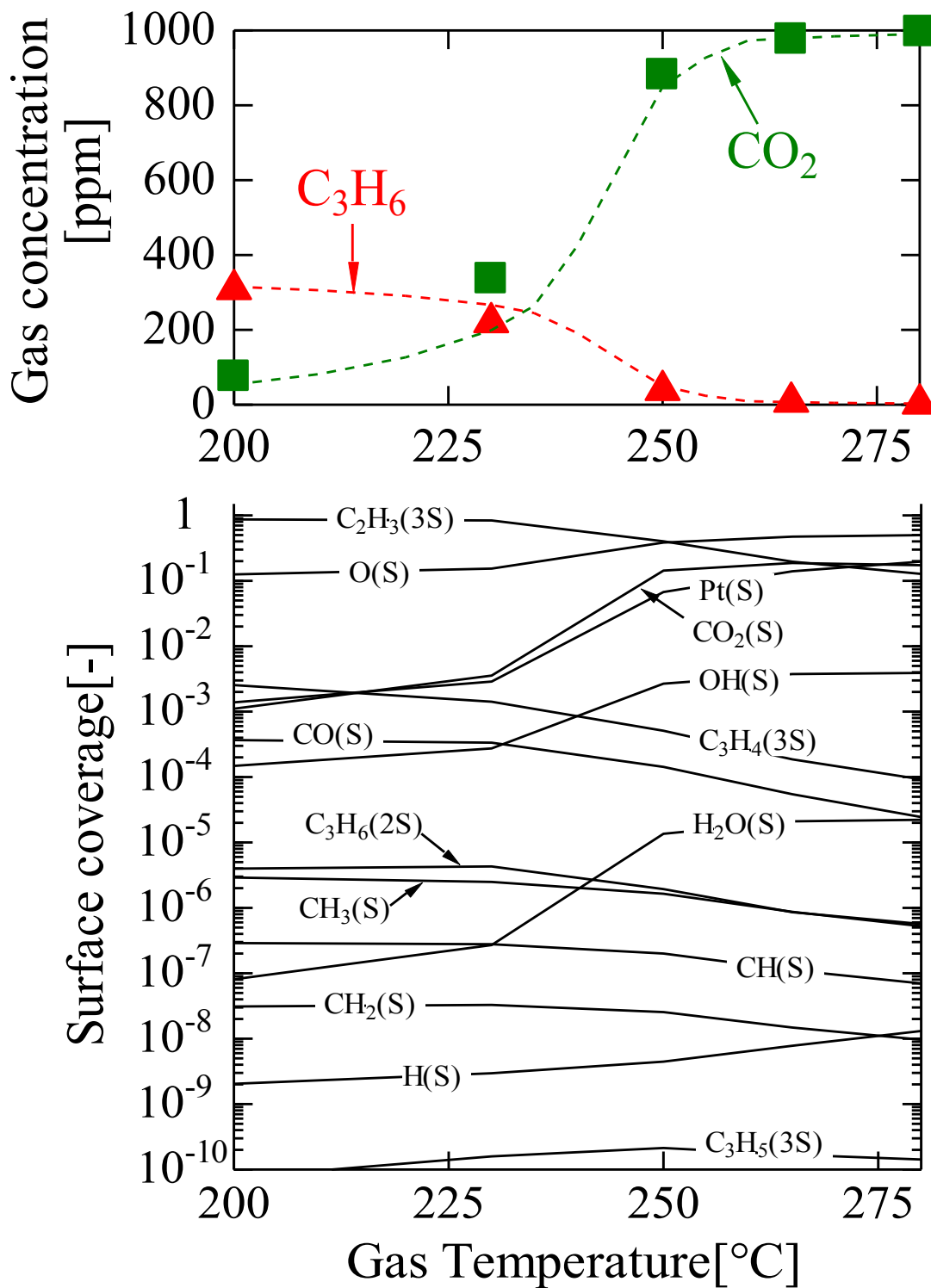
Fig. 5.13 Experimental and numerical results of gas phase C_3H_6 and CO_2 at downstream of catalyst, and simulated surface species profiles for fuel lean (O_2 excess) condition (333 ppm C_3H_6 and 3000 ppm O_2, Case VI in Table. 2.3)
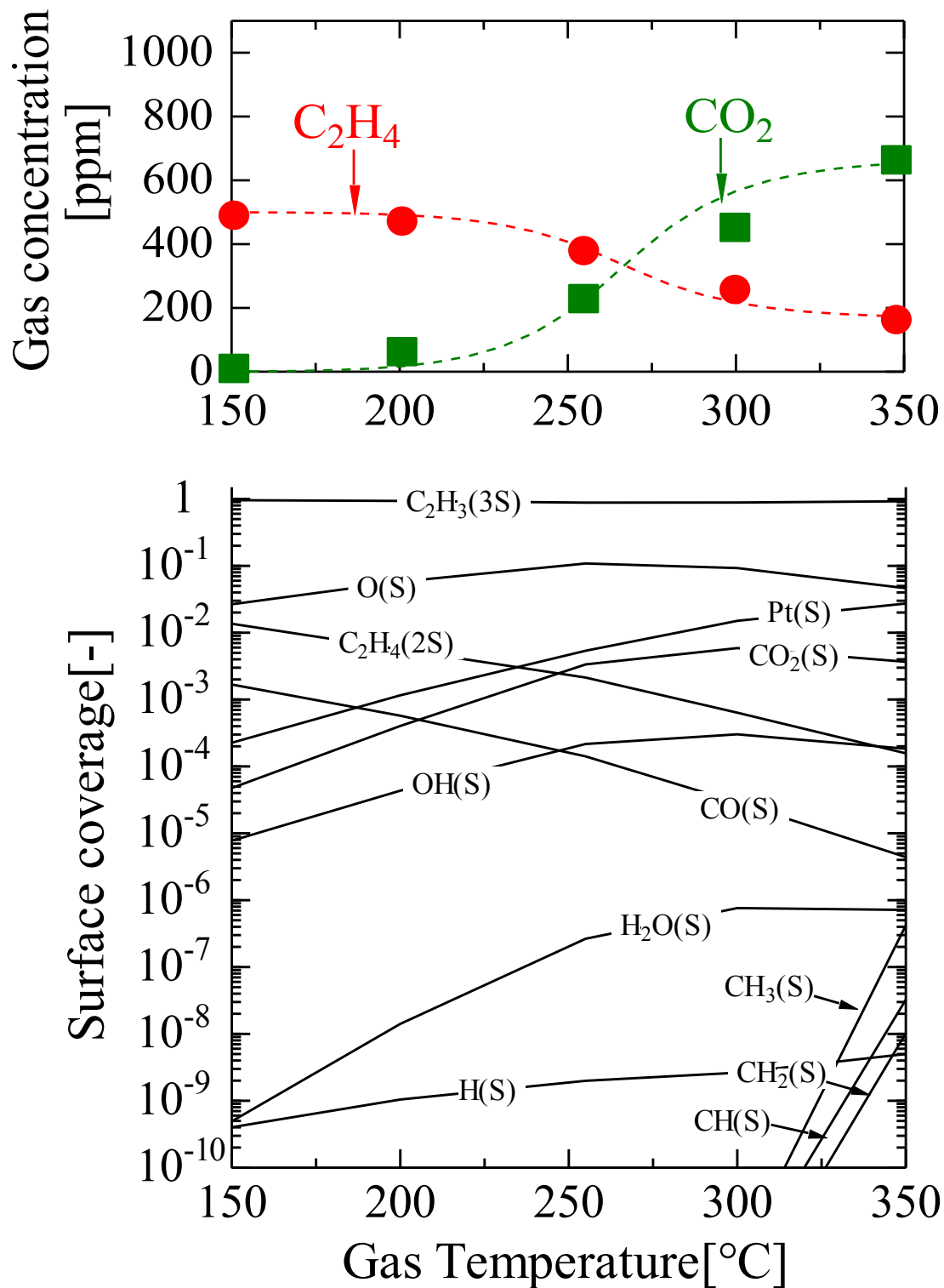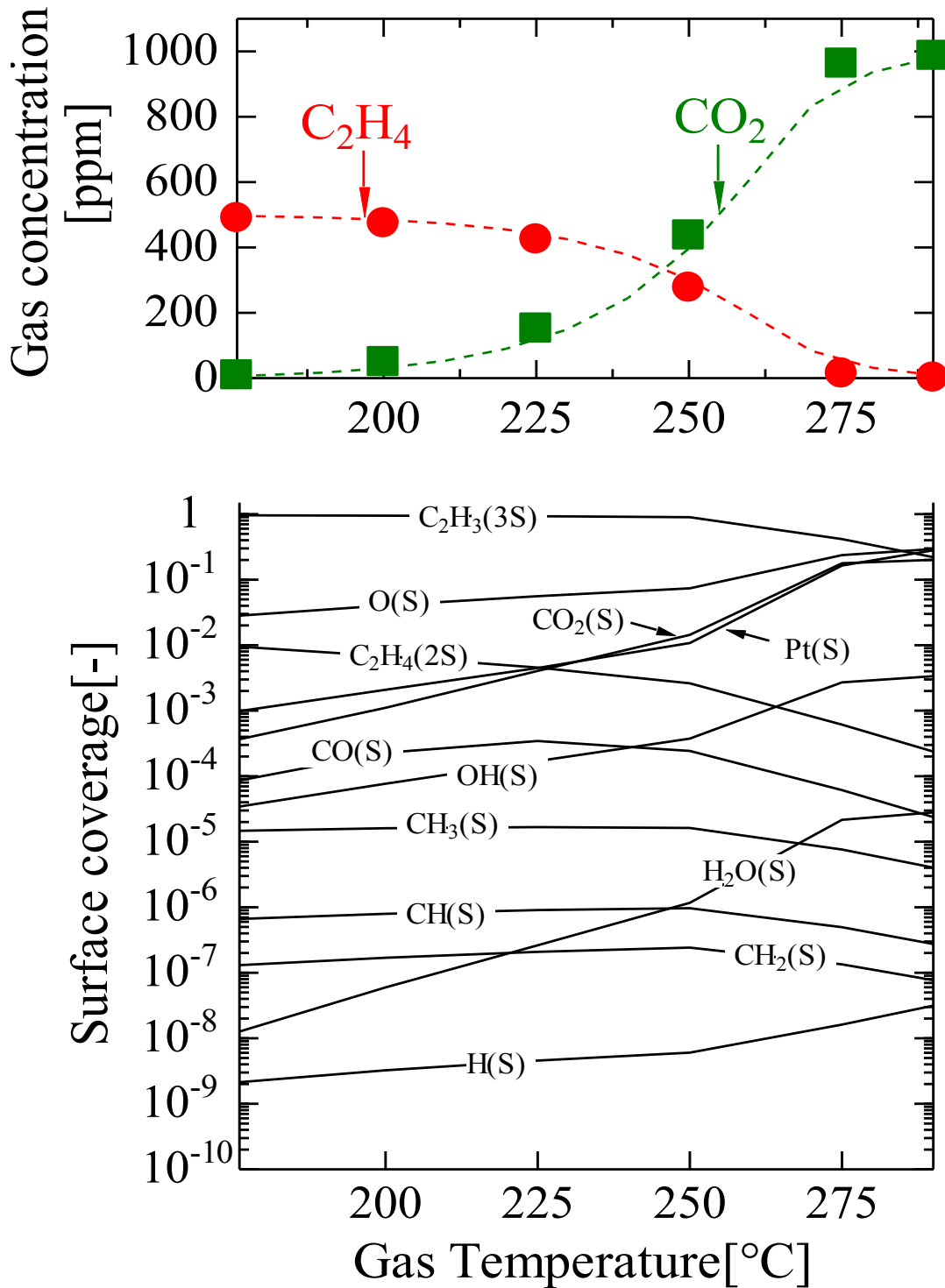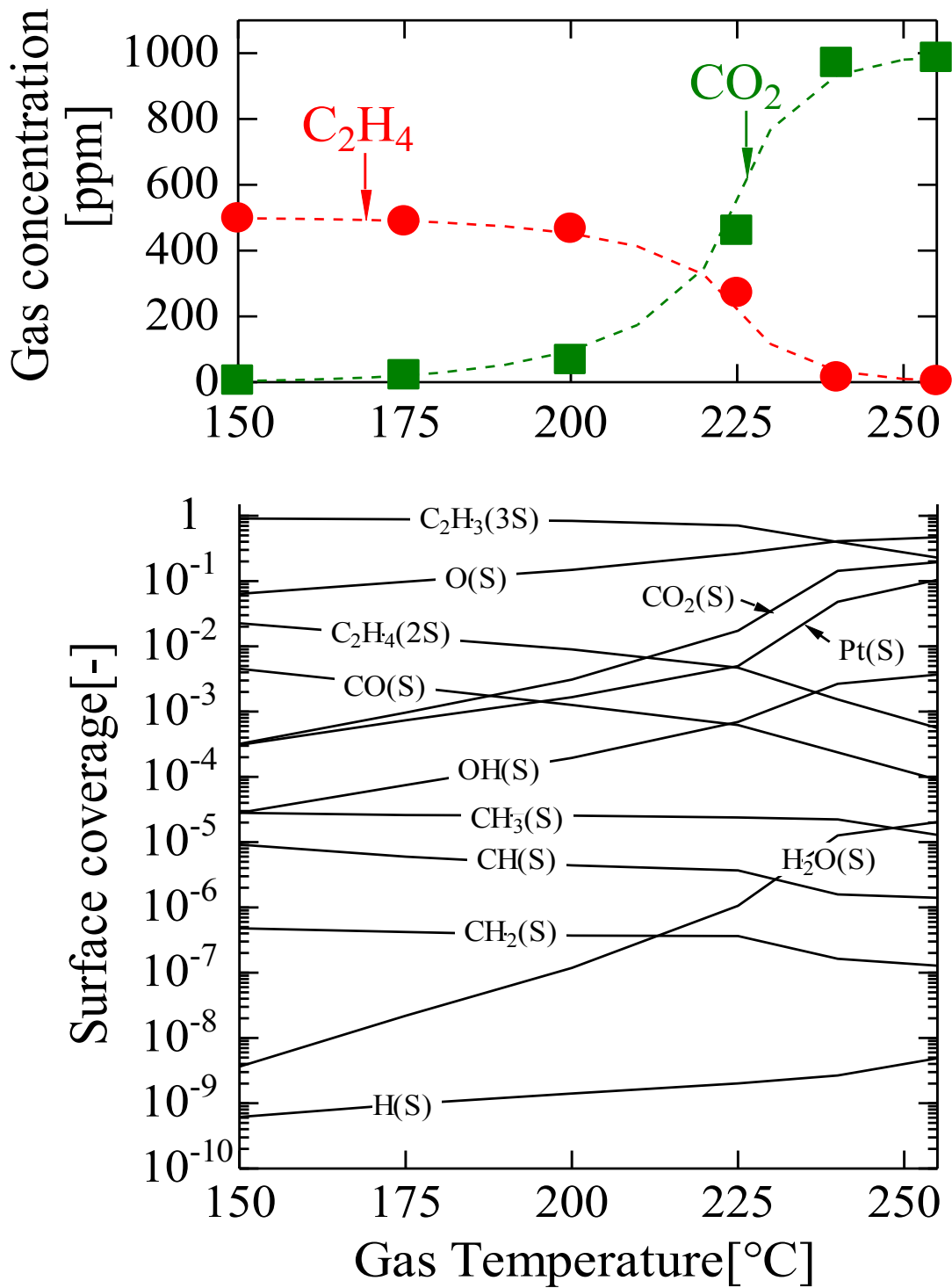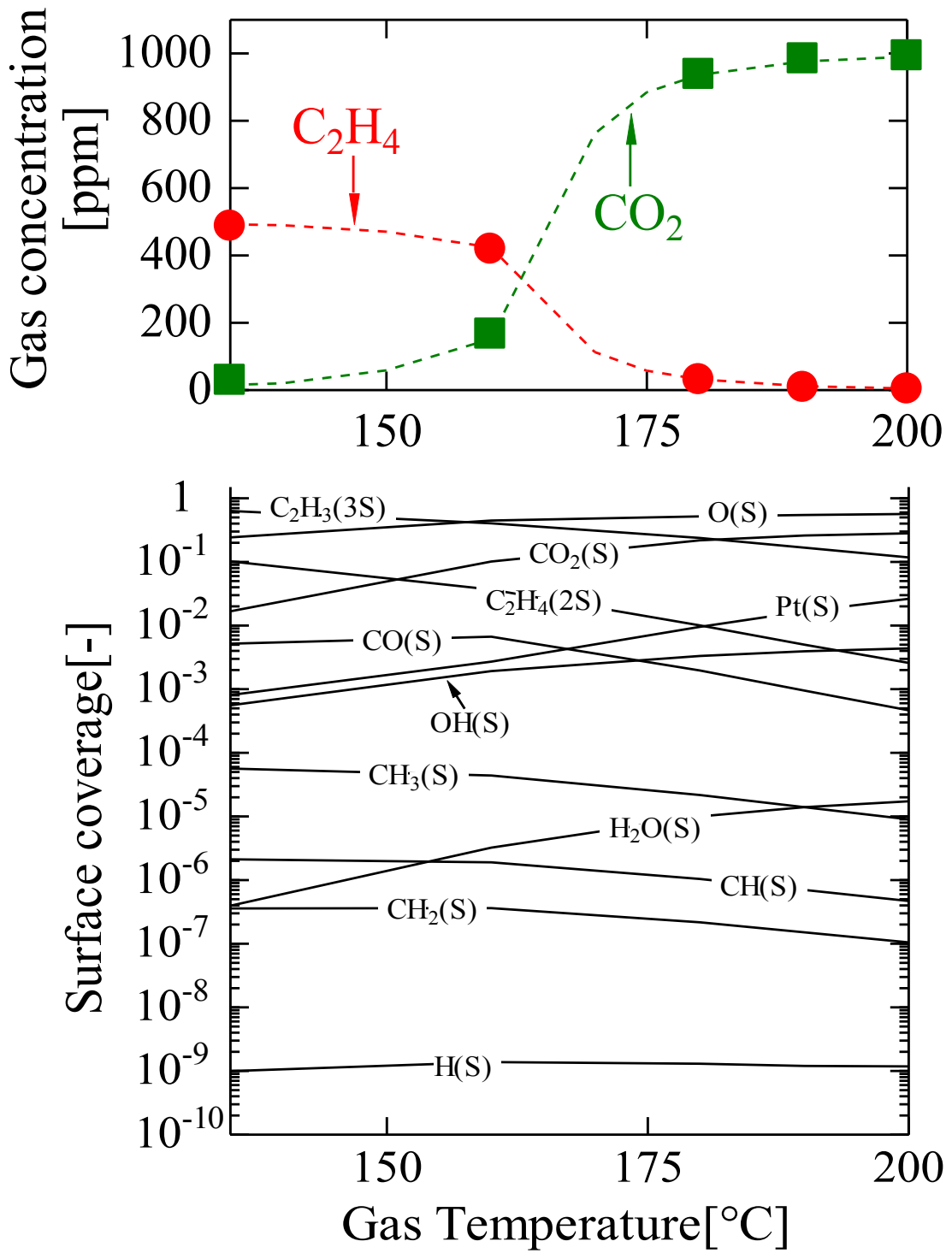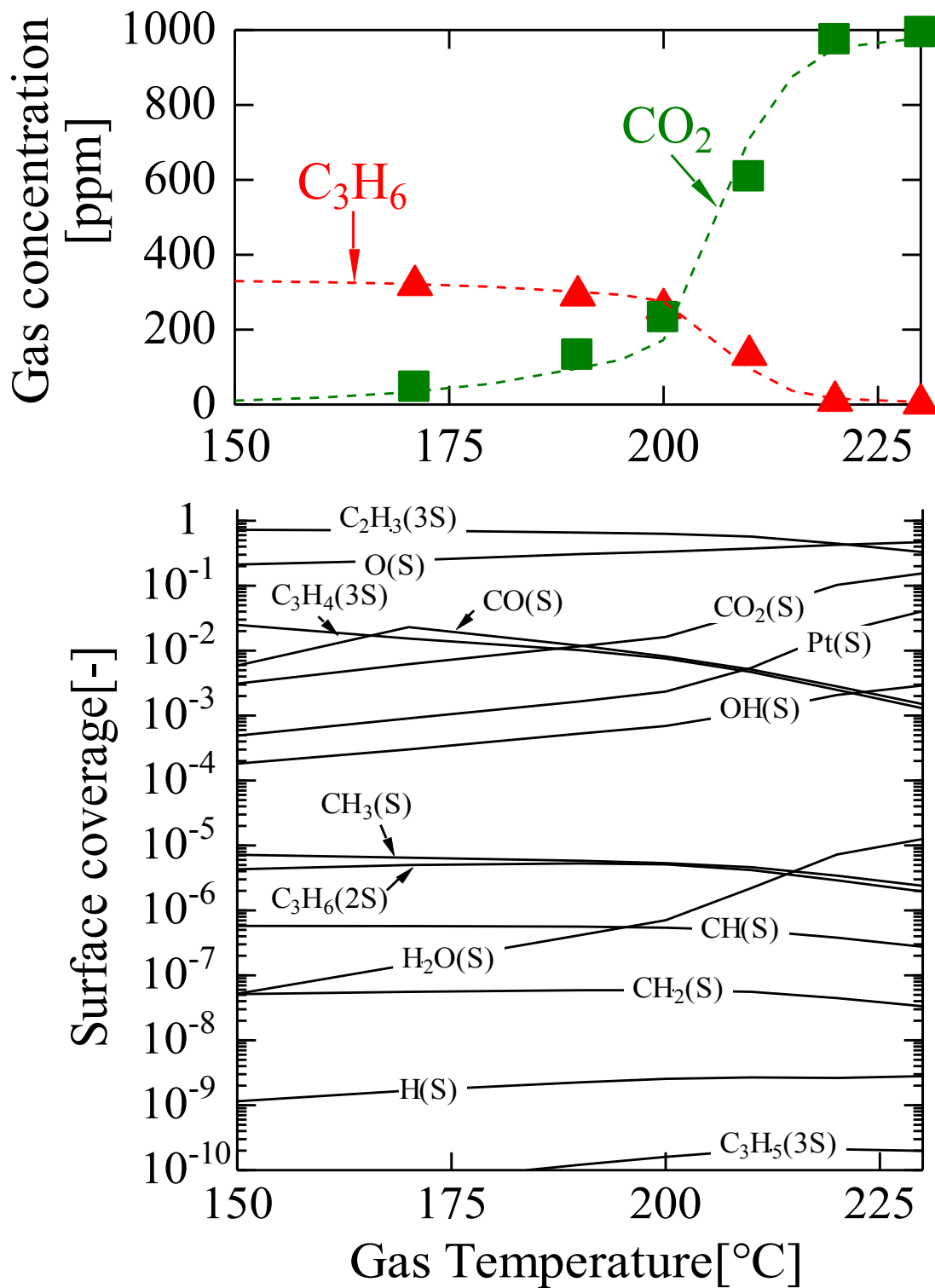
Fig. 5.14　Experimental and numerical results of gas phase C_3H_6 and CO_2 at downstream of catalyst, and simulated surface species profiles for fuel lean (O_2 excess) condition (333 ppm C_3H_6 and 10000 ppm O_2, Case VII in Table. 2.3)

5.2.6   Comparison between surface experiments and simulations results

Quantitative comparison between the surface species profiles by the numerical calculations and experiments are difficult.   Here, it should be noted that the weak peak of CH_x in the surface experiments does not directly mean that CH_x coverage is low. Again, only qualitative information, but not absolute information from the IR peaks is included for the modelling.   Only qualitative information, but not absolute information from the IR peaks can be obtained.   On the other hand, despite the CH_x weak peak intensities, the presence of linearly adsorbed CO(S) can be clearly confirmed from both experimental and simulated results.   Behavior of CO coverage for C_2H_4 / O_2 seems to have good tendency with the experiments qualitatively whereas poor tendency for C_3H_6 / O_2.   But, absolute value of the calculated CO(S) coverage are considerably smaller than those of CH_x, so that it can be ignored.   Another factor recognized in the figures from Fig. 5.7 to Fig. 5.14 is the drastic increase in the coverage of $CO_2(S)$ with temperature. Such kind of behavior can be proved from the surface species experimental results (in the figures from Fig. 2.12 to Fig. 2.17), in which gas phase CO_2 peaks, that come from the desorption of surface $CO_2(S)$ species, also increases with the temperature.

5.3   Validation of the versatility of the reaction mechanism

5.3.1   Comparison with C_3H_6 / CO / O_2 / N_2 and C_3H_6 / CO / O_2 / N_2 experiments

As for the validation of the reaction mechanism, additional experiments including multiple gas components are conducted and compared with the numerical simulations.   Table 2.4 in the chapter of experimental studies shows the experimental conditions, and here, realistic practical gas concentrations are focused to investigate. Fig. 5.15 and Fig. 5.16 show the comparison between the experimental conversion rate and simulation results for the C_2H_4 / CO / O_2 / N_2 and C_3H_6 / CO / O_2 / N_2 stoichiometric conditions (Case IX and X in Table 2.4).   Not only the light-off temperatures and complete conversion range of C_2H_4 and C_3H_6, but also those of CO agree well with the gaseous experimental results.   Stoichiometric light-off temperature of CO increases from 240 °C (Shimokuri et al., 2020) to around 260 °C with the presence of C_3H_6 and to around 270 °C with the presence of C_2H_4.   The same behavior can be seen for C_2H_4 that light-off temperature increases from 230 °C to 290 °C, and for C_3H_6, it increases from 250 °C to 273 °C.   Therefore, presence of CO makes the decrease in light-off performance of C_2H_4 and C_3H_6 and, the same fact for CO with the presence of HC species.
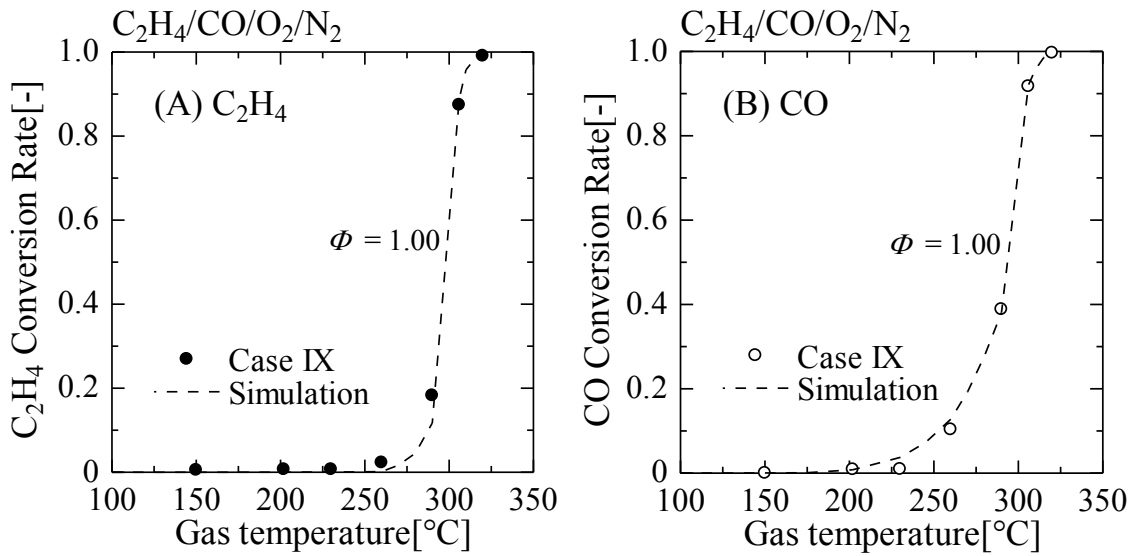
Fig. 5.15   Comparison between experimental and simulation results for stoichiometric condition (200 ppm C_2H_4, 5000 ppm CO and 3100 ppm O_2, Case IX in Table 2.4) (A) C_2H_4, (B) CO
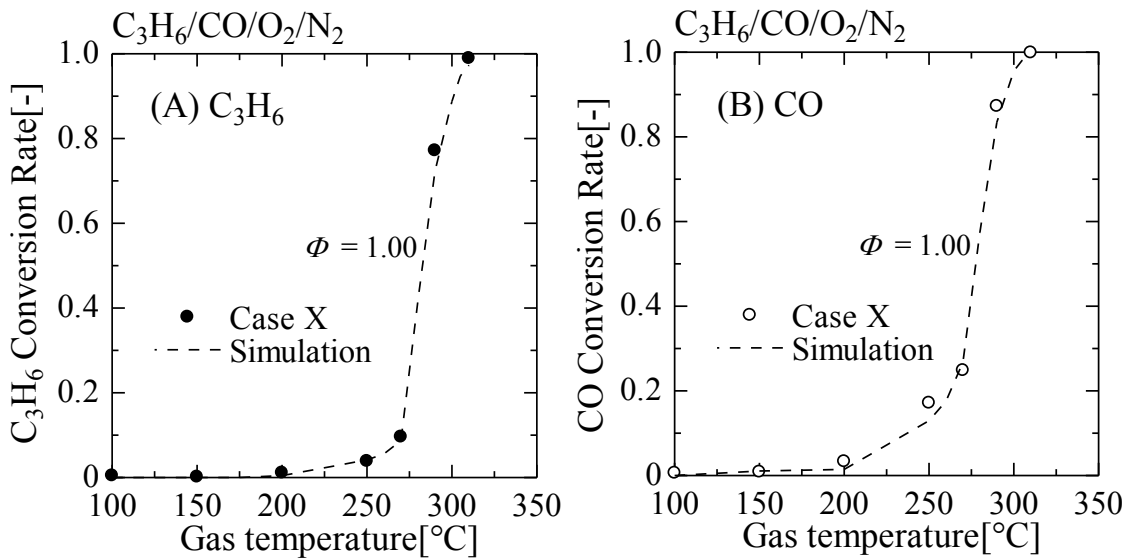
Fig. 5.16   Comparison between experimental and simulation results for stoichiometric condition (111 ppm C_3H_6, 5000 ppm CO and 3000 ppm O_2, Case X in Table 2.4) (A) C_3H_6, (B) CO

In Fig. 5.17 and Fig. 5.18, numerically calculated surface species profiles of case IX and X in Table 2.4 are shown together with their respective downstream gas compositions. In these figures, horizontal X axis is the gas temperature and vertical Y axis is the gas concentration for gas species and surface coverage fraction for surface species. R axis is also included as vertical axis and unit is same as Y axis, and respective gas concentration can be read on the axis by the directions as shown on the curves.

From the surface profiles shown in Fig. 5.17, it is observed that the multiple Pt sited $C_2H_3(3S)$ is mostly covered on the species. Despite the lower sticking probability of $C_2H_4(g)$ than $CO(g)$, surface is mostly covered by the intermediate HC species meaning that the potential active Pt surface sites for $CO(g)$ to form $CO(S)$ are blocked by the intermediate $C_2H_3(3S)$ species. Moreover, because of having very low sticking probabilities and being blocked by $CO(S)$ and $C_2H_3(3S)$, $O_2(g)$ cannot stick on the surface, and thus with the absence of $O(S)$ on the surface, the oxidation of both C_2H_4 and CO becomes slower than their respective 2 gas component (CO / O_2 and C_2H_4 / O_2) systems. This can explain why the light-off temperature of both CO and C_2H_4 increases with the presence of each other. Once the light-off temperature of C_2H_4 is achieved, in other words, the C-C bond in the $C_2H_3(3S)$ is broken, more free surface sites are available for $CO(g)$ and $O_2(g)$ to adsorb, therefore, the oxidation process can be proceeded.

Similar behavior is observed for C_3H_6 / CO / O_2 / N_2 system and is shown in Fig. 5.18. In Fig. 5.18, surface is also mostly covered by the multiple Pt sited $C_2H_3(3S)$ species so that less active surface sites for $CO(g)$ and $O_2(g)$. It is well known that presence of $C_3H_6(g)$ can inhibit $CO(g)$ oxidation in the aftertreatment system (Abedi et al., 2012; Březina et al., 2020; Voltz et al., 1973). From Fig. 5.18, such kind of behavior can be clearly explained since the coverage of $CO(S)$ decreases drastically as the temperature increases while $C_2H_3(3S)$ gradually decreases toward the light-off temperature. Also, once the light-off temperature of C_3H_6 is achieved, potential surface sites for $CO(g)$ and $O_2(g)$ becomes available, and the oxidation process can be proceeded.

Presence of CO makes the more reactive C_2H_4 becomes less reactive than C_3H_6. It can be observed by the increase in light-off temperature, only about 23K increase for C_3H_6 while 60K increase for C_2H_4. This can be explained by the surface coverage of $C_2H_3(3S)$ species since for C_2H_4 / CO / O_2 / N_2 system, maximum coverage fraction of it is 0.975, while for C_3H_6 / CO / O_2 / N_2 system, it is 0.76. This leads $CO(g)$ to have less active surface sites for its adsorption, and maximum coverage of $CO(S)$ in C_2H_4 / CO / O_2 / N_2 system is 0.062 while in C_3H_6 / CO / O_2 / N_2 system, it is around 0.14, resulting higher chances to achieve lower light-off temperature. Therefore, CO light-off promotes C_3H_6 light-off and C_2H_4 becomes less reactive than C_3H_6.

In addition, complete conversion temperature of C_2H_4 and CO becomes higher for C_2H_4 / CO / O_2 / N_2 system than their respective C_2H_4 / O_2 / N_2 and CO / O_2 /N_2 systems.   But for C_3H_6, it stays nearly the same at 310 °C for both systems while for CO, it increases from 290 °C to 310 °C.   Presence of CO makes the increase in complete conversion temperature of C_2H_4 from 290 °C to 320 °C, and the same temperature increment for CO in the presence of C_2H_4.   It is found and discussed that washcoat diffusion is the dominant process for high temperature conversion.   However, in this case, it cannot be clearly explained by the process because the effective diffusion coefficient of C_2H_4 and CO are nearly the same value, which is shown in Fig. 5.19.   In Fig. 5.19, effective diffusion coefficient of C_2H_4, C_3H_6 and CO are shown for the catalyst used in this study.   Therefore, due to the fact, diffusion process alone cannot explain why the complete conversion temperature increases.   By comparing the surface species coverage of stoichiometric conditions of C_2H_4 / O_2 / N_2 (Fig. 5.8) and C_2H_4 / CO / O_2 / N_2 (Fig. 5.17), the surface coverage of C_2H_3(3S) starts to decrease from 230 °C in the C_2H_4 / O_2 / N_2 (Fig. 5.8) system making more free space for O(S) for the complete oxidation, and in the C_2H_4 / CO / O_2 / N_2 (Fig. 5.17) system, it only starts to decrease from 290 °C making less space for O(S), therefore, the complete conversion temperature increases in the C_2H_4 / CO / O_2 / N_2 system.

However, for the C_3H_6 / O_2 / N_2 system (Fig. 5.12) and C_3H_6 / CO / O_2 / N_2 system (Fig. 5.18), it can be clearly explained from the diffusion process because C_3H_6 has lower effective diffusion coefficient value than CO as shown in Fig. 5.19, and therefore, diffusion of C_3H_6 dominate for both systems and the complete oxidation temperature stays nearly the same at 310 °C.

Fig. 5.17 Experimental and numerical results of gas phase C_2H_4, CO and CO_2 at downstream of catalyst, and simulated surface species profiles for stoichiometric condition (200 ppm C_2H_4, 5000 ppm CO and 3100 ppm O_2, Case IX in Table 2.4)

Fig. 5.18 Experimental and numerical results of gas phase C_3H_6, CO and CO_2 at downstream of catalyst, and simulated surface species profiles for stoichiometric condition (111 ppm C_3H_6, 5000 ppm CO and 3000 ppm O_2, Case X in Table 2.4)
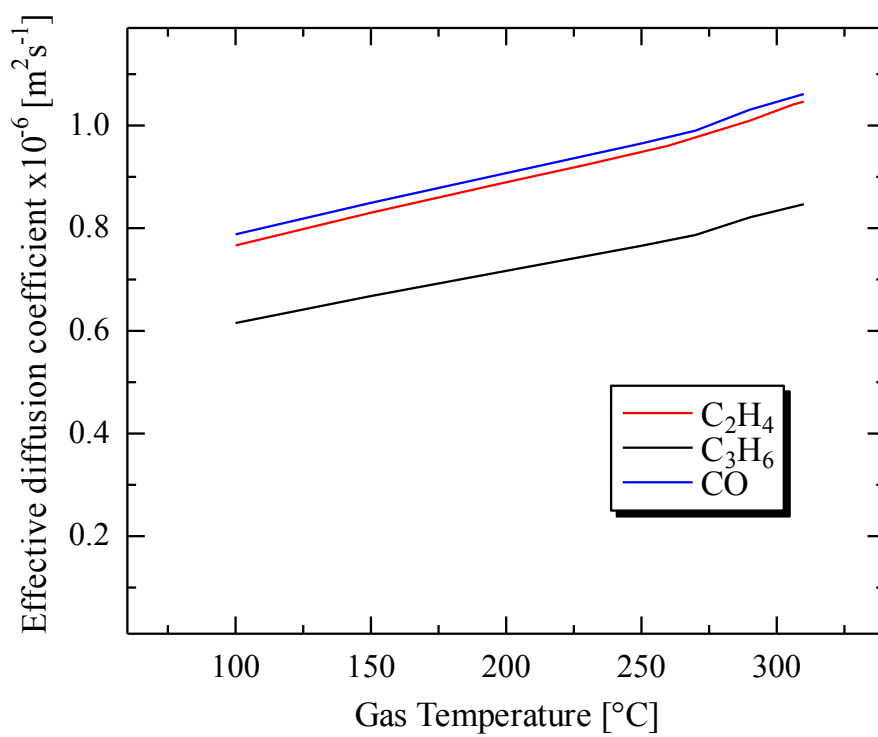
Fig. 5.19   Effective diffusion coefficients of C_2H_4, C_3H_6 and CO
for the catalyst used in this study

5.3.2　Comparison with C_2H_4 / C_3H_6 / CO / O_2 / N_2 experiments

More realistic practical gas composition conditions such as the mixture of C_2H_4, C_3H_6, and CO for different O_2 concentration are investigated.　In Fig. 5.20, comparison between the experimental conversion rate and simulation results for the mixture of C_2H_4 / C_3H_6 / CO / O_2 / N_2 stoichiometric condition and fuel lean (O_2 excess) conditions (Case XI, XII and XIII in Table 2.4).　It can be observed that there is a good agreement between experimental and simulation results.　Here, the light-off temperature of C_2H_4 and C_3H_6 becomes nearly the same for all oxygen concentration conditions, and the quantitative values are less than those of two-gas (C_2H_4 / O_2 / N_2 and C_3H_6 / O_2 / N2) component systems.　It is due to the blocking of potential active surface sites by the intermediate species and it prevents the most reactive HC species from being oxidized faster.

In Fig. 5.21, Fig. 5.22 and Fig. 5.23, simulated surface species profiles for the stoichiometric and fuel lean (O_2 excess) conditions (Case XI, XII and XIII in Table 2.4) are shown and, it can be clearly observed that the surface is mostly occupied by the $C_2H_3(3S)$ species.　Due to the high sticking probability, CO(g) and C_3H_6(g) can be adsorbed preferentially than C_2H_4(g).　Presence of C_2H_4(2S) shows that the formation of C_2H_3(3S) may mostly come from C_3H_6(g) than from C_2H_4(g).　Also, the fact reported in the potential energy section indicates that formation of C_2H_3(3S) from C_3H_6(g) preferentially proceeds than from C_2H_4(g), which leads to slow oxidation of C_2H_4(g) due to the co-existing C_3H_6(g).　Energy to form C_2H_3(3S) is more favorable from C_3H_6(2S) than from C_2H_4(2S), so that there is lower chance for C_2H_4(g) to proceed the oxidation than in the two gas (C_2H_4 / O_2 / N_2) component system.　From Fig. 5.20, it can be found that even though CO(g) has earlier light-off temperature than C_2H_4(g) and C_3H_6(g), higher conversion temperatures of CO(g) approached to be nearly the same as those of C_2H_4(g) and C_3H_6(g).　It is because of the blocking of the potential active surface sites by the C_2H_3(3S) intermediate species, and there is less space for O_2(g) to adsorb on the surface so that the conversion temperature of CO(g) becomes higher as the HC species.

Upon the increase in oxygen concentration, both the light-off temperatures of C_2H_4, C_3H_6 and CO , and the complete conversion temperatures decrease as shown in Fig. 5.20.　For fuel lean (O_2 excess) conditions, decrease in C_2H_3(3S) species coverage starts earlier than stoichiometric condition so that the light-off temperature decreases. However, for the complete conversion temperatures of stoichiometric condition, it becomes higher than less gas component systems which means not only the low effective diffusion coefficient of C_3H_6 but also higher number of intermediate C_2H_3(3S) play important roles in the C_2H_4 / C_3H_6/ CO / O_2 / N_2 system.

Fig. 5.20   Comparison between experimental and simulation results for stoichiometric and fuel lean (O$_2$ excess) conditions (200 ppm C$_2$H$_4$, 100 ppm C$_3$H$_6$, 5000 ppm CO and 3550 ppm / 6000 ppm / 10000 ppm O$_2$, Case XI, XII and XIII in Table 2.4) (A) C$_2$H$_4$, (B) C$_3$H$_6$, (C) CO
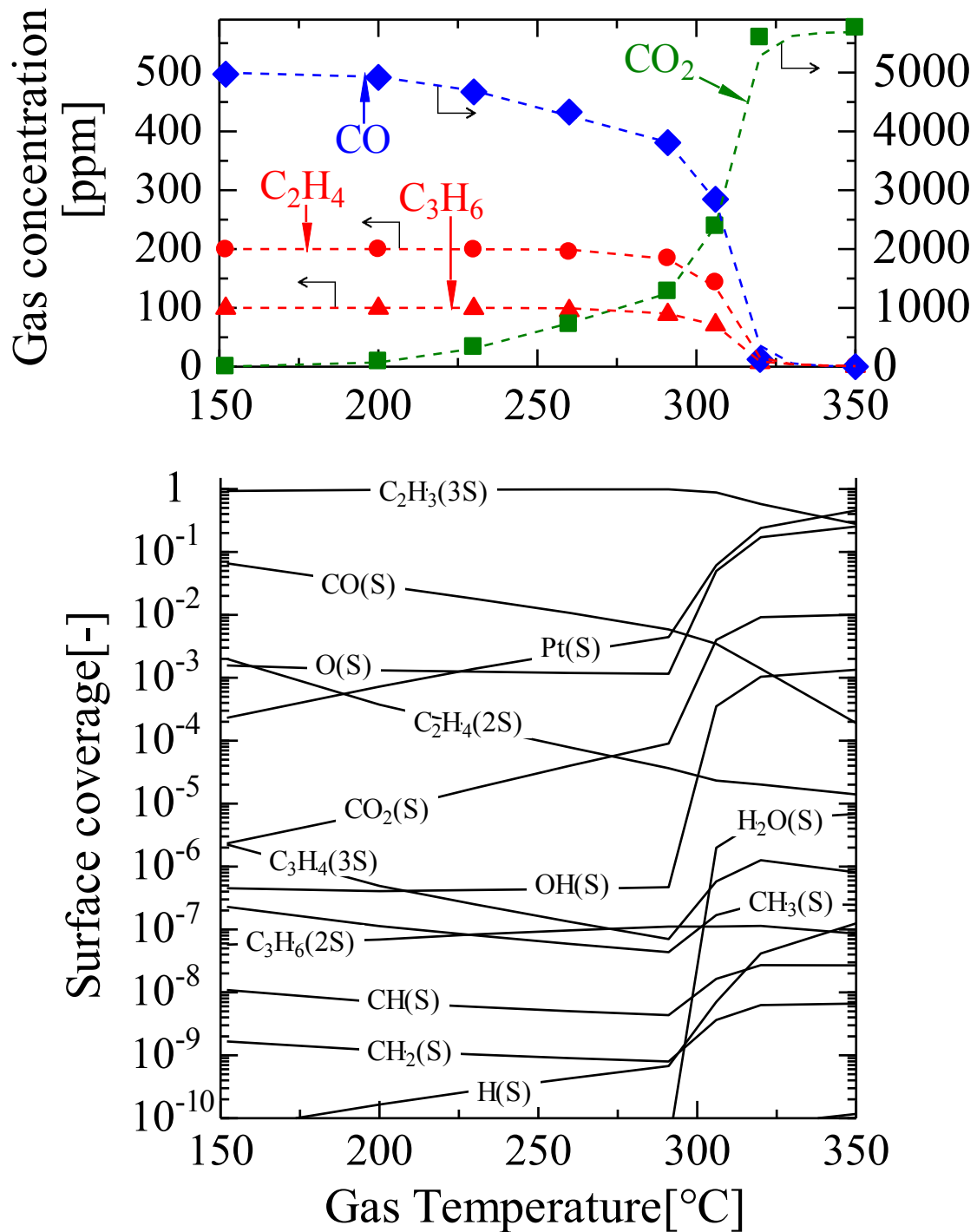
Fig. 5.21   Experimental and numerical results of gas phase C_2H_4, C_3H_6, CO and CO_2 at downstream of catalyst, and simulated surface species profiles for stoichiometric   condition (200 ppm C_2H_4, 100 ppm C_3H_6, 5000 ppm CO and 3550 ppm O_2, Case XI in Table 2.4)
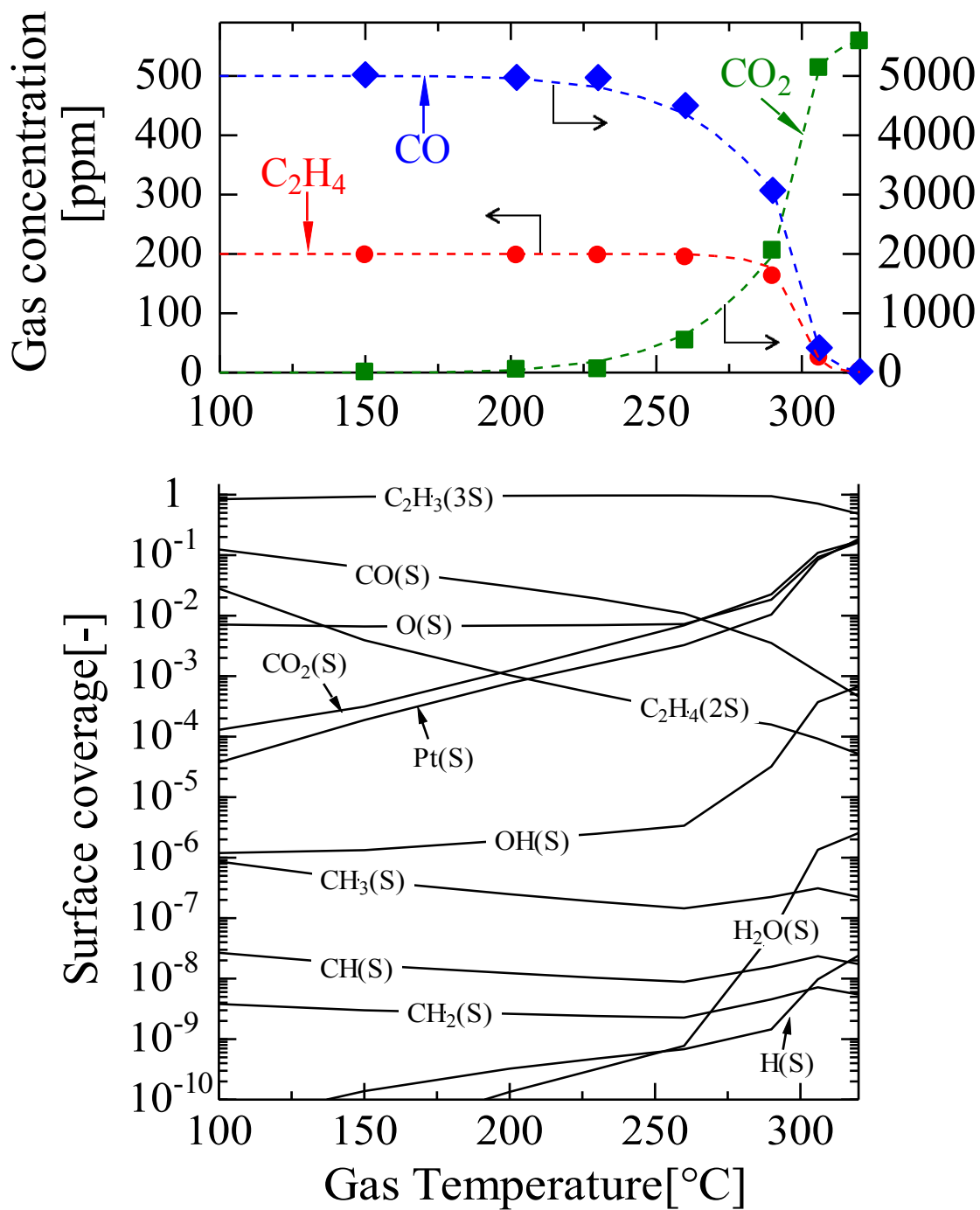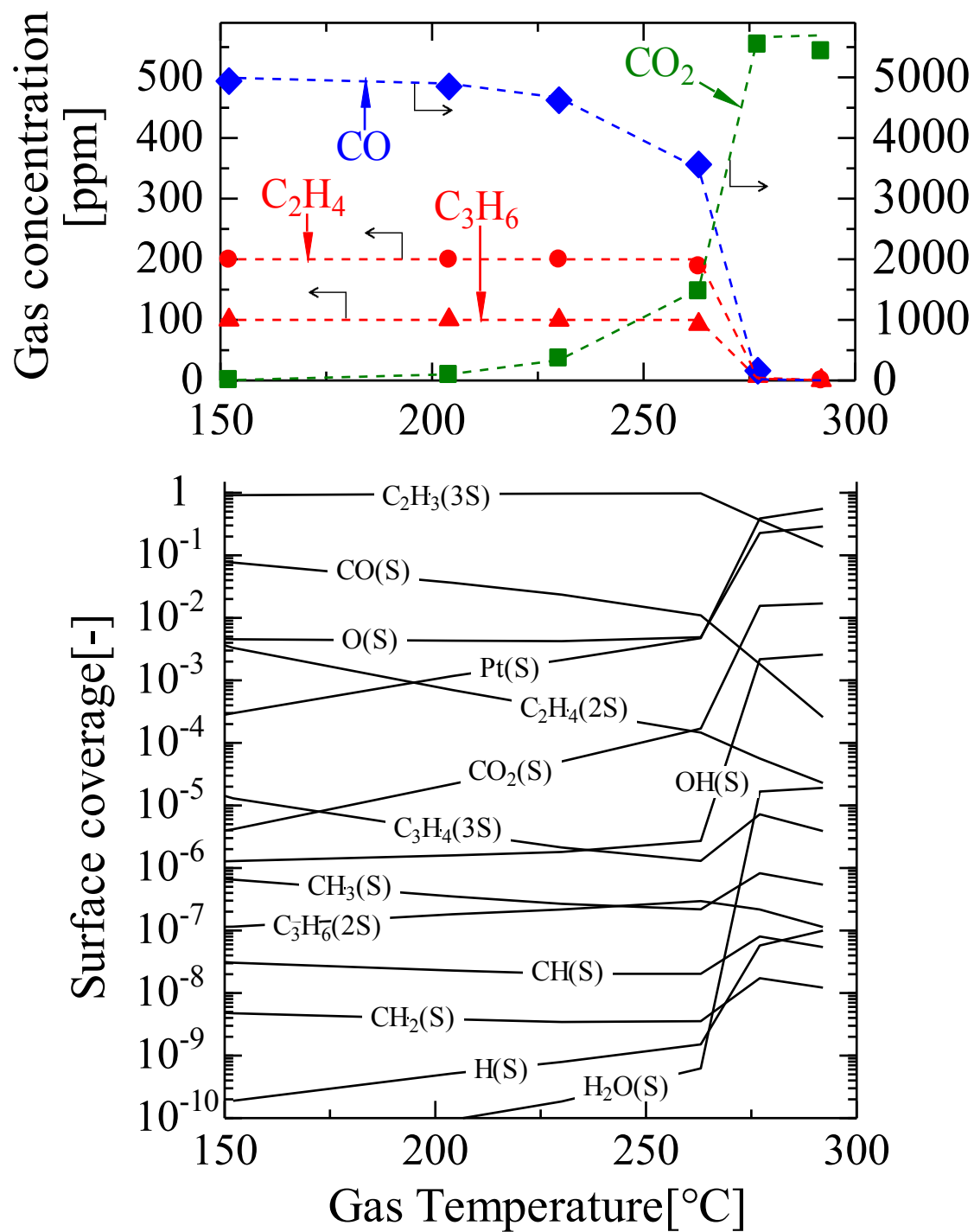
Fig. 5.22 Experimental and numerical results of gas phase C_2H_4, C_3H_6, CO and CO_2 at downstream of catalyst, and simulated surface species profiles for fuel lean (O_2 excess) condition (200 ppm C_2H_4, 100 ppm C_3H_6, 5000 ppm CO and 6000 ppm O_2, Case XII in Table 2.4)
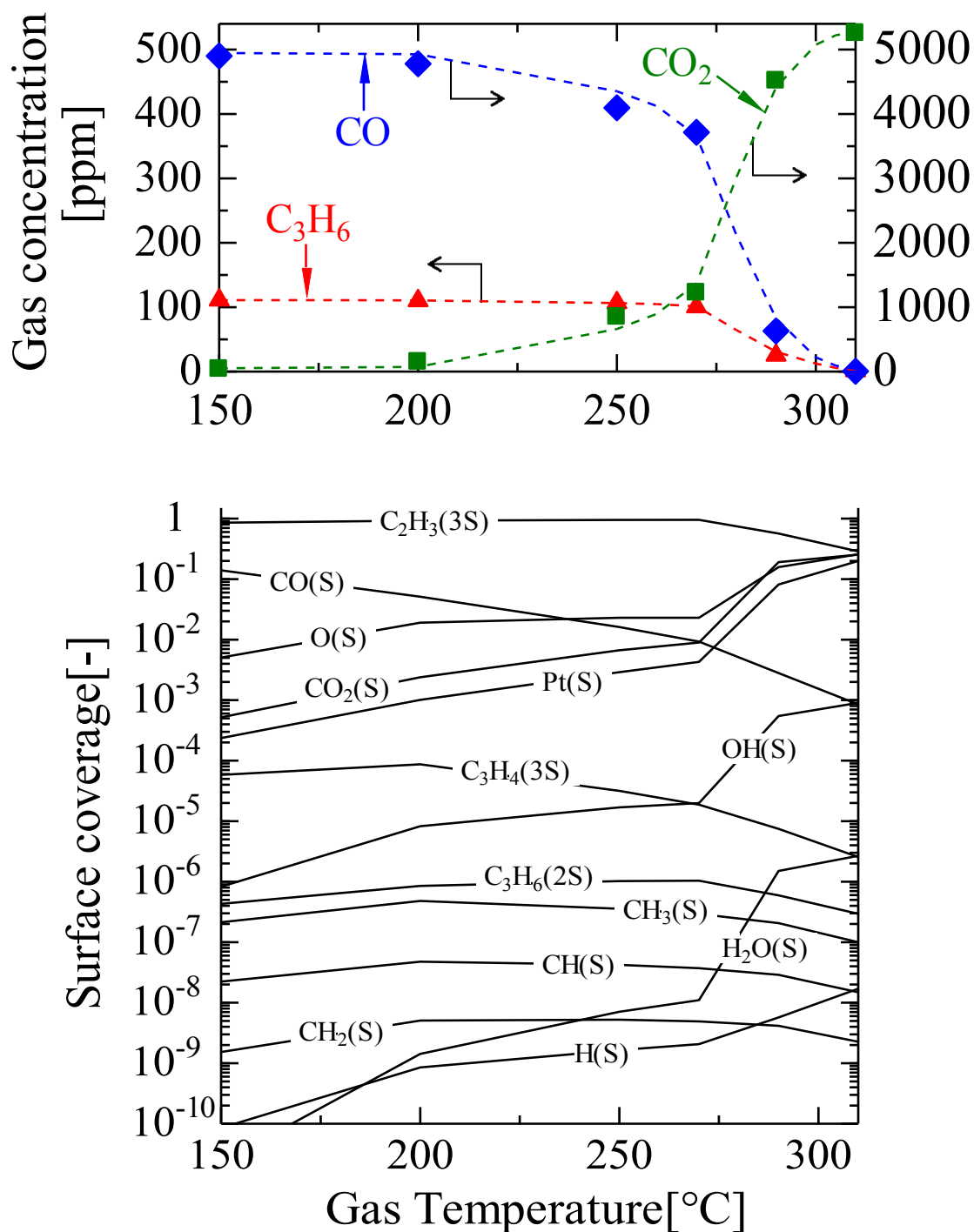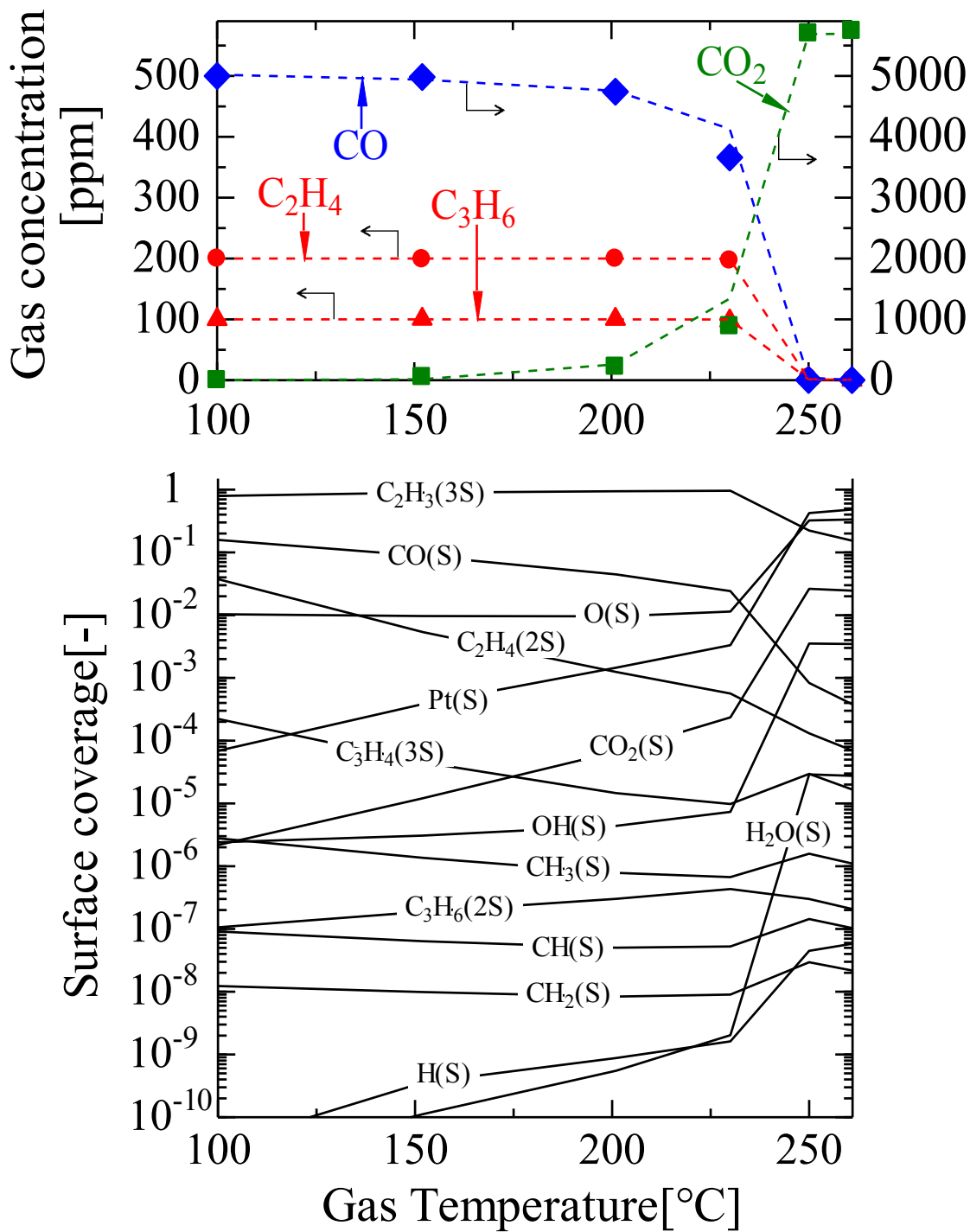
Fig. 5.23   Experimental and numerical results of gas phase C_2H_4, C_3H_6, CO and CO_2 at downstream of catalyst, and simulated surface species profiles for fuel lean (O_2 excess) condition (200 ppm C_2H_4, 100 ppm C_3H_6, 5000 ppm CO and 10000 ppm O_2, Case XIII in Table 2.4)

5.3.3　Comparison with C_2H_4 / C_3H_6 / CO / O_2 / CO_2 experiment

As a final step, more precise realistic practical gas condition, which is the mixture of C_2H_4, C_3H_6, CO, O_2 and CO_2 is investigated. Experimental condition is the stoichiometric condition with 200 ppm of C_2H_4, 100 ppm of C_3H_6, 5000 ppm of CO, 3550 ppm of O_2 and 60000 ppm of CO_2. In Fig. 5.24, comparison between the experimental conversion rate and simulation result is shown and it can be observed that there is a good agreement between experimental and simulation results. Numerically calculated surface species profiles are also checked, and the results are nearly the same as the results shown in Fig. 2.21.
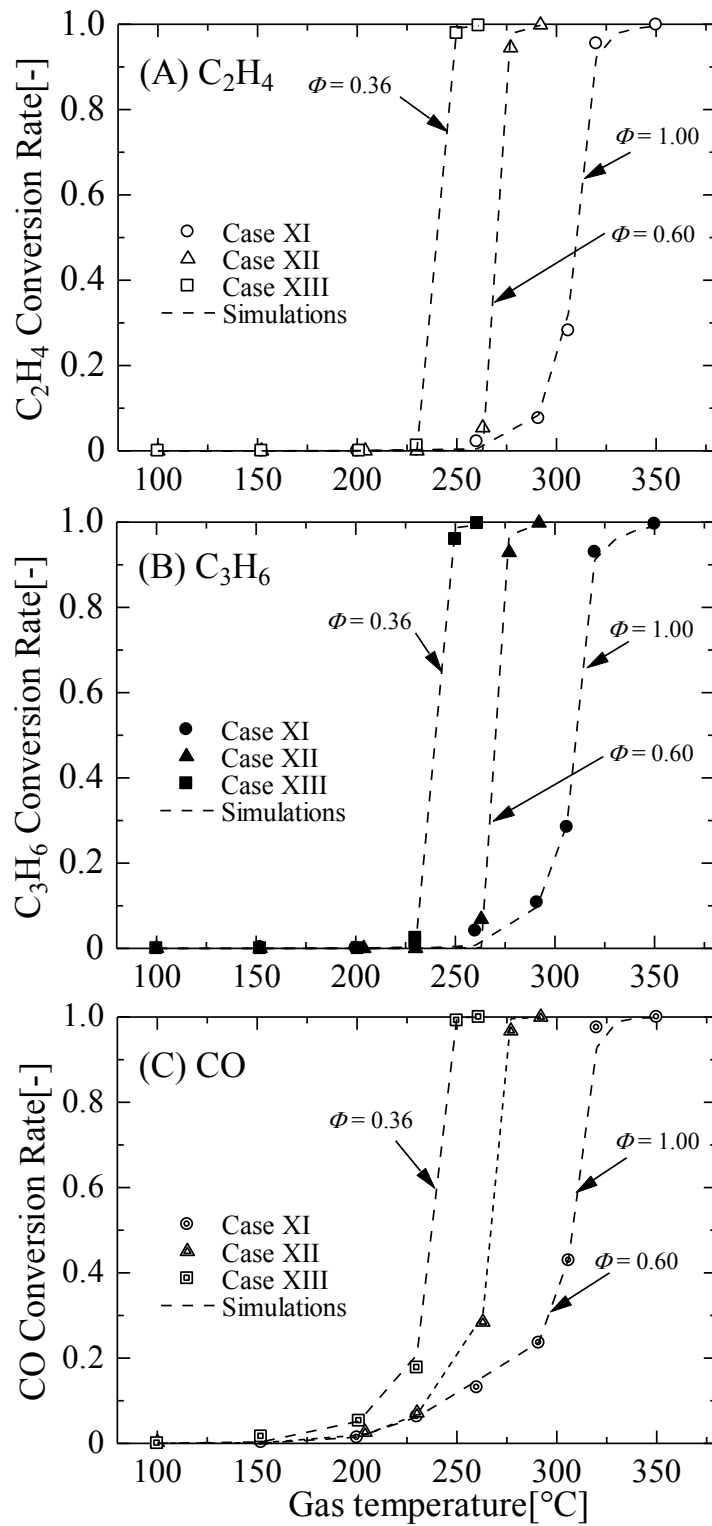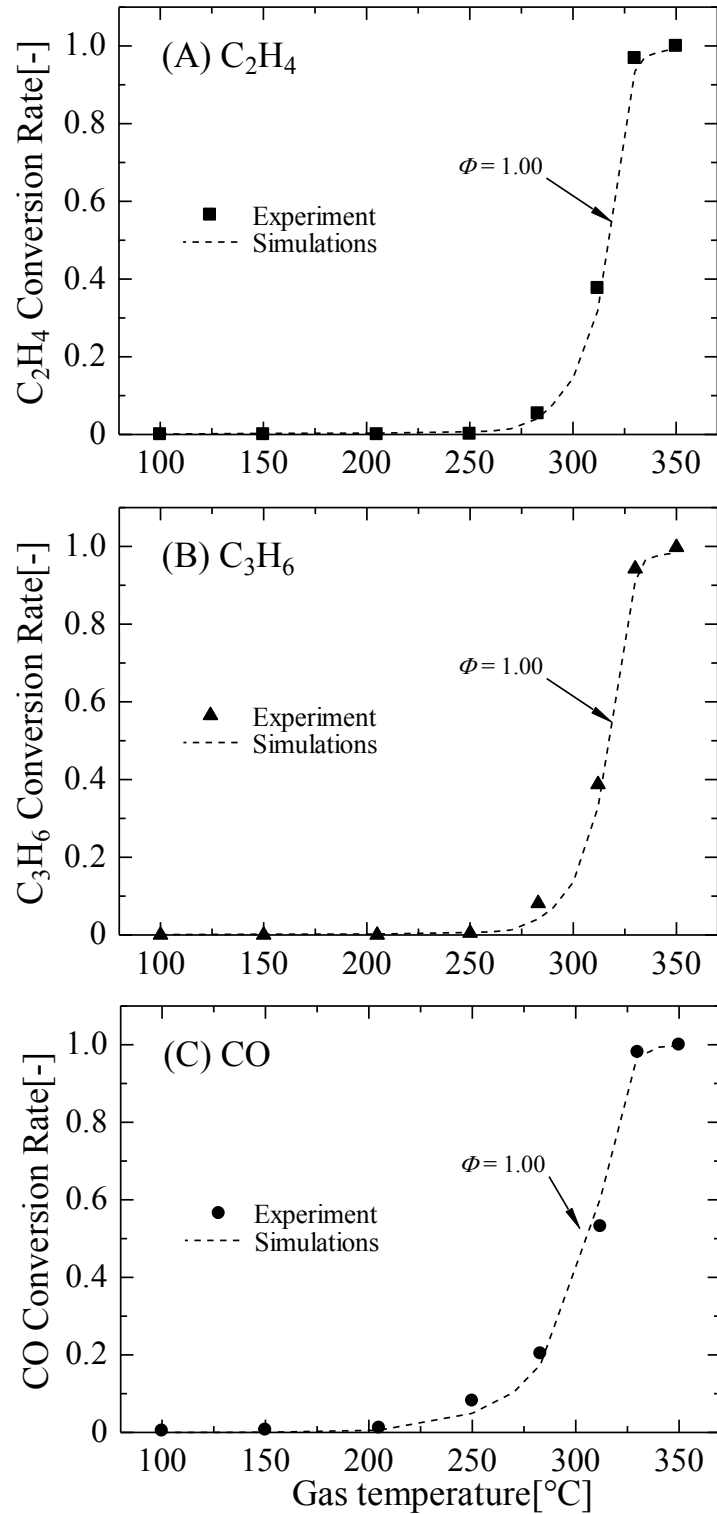
Fig. 5.24   Comparison between experimental and simulation results for
stoichiometric condition (200 ppm C_2H_4, 100 ppm C_3H_6, 5000 ppm CO, 3550 ppm
O_2 and 60000 ppm CO_2 (A) C_2H_4, (B) C_3H_6, (C) CO

5.4   Conclusions

In this chapter, systematic procedure of kinetic parameter estimation for the proposed detailed surface reaction mechanism is discussed.   Fundamental chemistry set of CO / O_2 surface reaction mechanism, CO / H_2 / O_2 surface reaction mechanism and then, the final reaction mechanism are developed step by step by carefully considering the kinetic parameters from the aspects of thermodynamic consistency.   By using the proposed developed surface reaction mechanism and numerical modelling method, numerical simulations, such as conversion results as well as surface coverage results, are carried out and discussed.   Developed detailed surface reaction mechanism is validated by the multiple gas compositions experiments, and realistic exhaust gas composition experiment.   From these results, conclusions can be drawn as the following:

1. Numerical simulations by the proposed C_2H_4 / C_3H_6 detailed surface mechanism can reproduce the gas phase conversion experimental results in a wide range of oxygen concentration conditions, as shown in this study, especially from $\Phi = 0.15$ to $\Phi = 1.5$.
2. Change in the light-off temperature by the surface coverage of multiple sited intermediate HC species, in this study, $C_2H_3(3S)$, for different oxygen concentration condition is proved, to show that presence of multiple active surface site occupied stable HC intermediate species is an important fact to consider in the heterogenous catalytic reaction modelling.
3. Versatility of the reaction mechanism is validated by using multiple gas composition experiments, such as C_2H_4 / CO / O_2 / N_2, C_3H_6 / CO/ O_2 / N_2, C_2H_4 / C_3H_6 / CO/ O_2 / N_2, and C_2H_4 / C_3H_6 / CO/ O_2 / CO_2 systems, and results show good agreement.
4. Although the washcoat diffusion phenomena is the dominant process in high temperature conversion region, complete oxidation temperature can be increased by the surface coverage of multiple sited species if the effective diffusion coefficient of the species is nearly the same.
5. In the higher number of gas composition conditions, higher number of multiple sited stable intermediate species can affect the light-off performance, and transport properties of reactant gases into the washcoat layer can affect the complete oxidation temperature well.
6. The proposed reaction mechanism can reproduce good agreement over realistic exhaust gas conditions.

Chapter 6

Conclusions and suggestions for future work

6.1   Conclusions

In this study, numerical modelling of washcoated honeycomb monolith catalyst is presented ,and from the aspect of the possibilities of more than one site occupations by CH_x species on PGM, a thermodynamic consistent detailed surface reaction mechanism for C_2H_4 and C_3H_6 over Pt/Al_2O_3 catalyst is proposed and developed based on the gaseous and surface species measurements.   Experimental studies of the gas phase conversion and surface species are conducted by using monolith honeycomb catalyst and powdered catalyst, which is the fragment of monolith washcoat.   Gas phase conversion rate experiments are measured by using Fourier Transform Infrared (FT-IR) equipment and gas analyzers.   Surface species experiments are measured by using *in-situ* FT-IR equipment.   The physical parameters of the catalyst such as metal dispersions, washcoat pore diameters and so on are identified with powdered catalyst, and furthermore, coverage of surface species in various adsorption regimes are examined by *in-situ* FT-IR under the same conditions of inlet gas temperature and compositions as monolith honeycomb experiments.

From the gas phase experimental results, among the exhaust hydrocarbon species from the internal combustion engines, C_2H_4 and C_3H_6 are found to have the highest reactivity, while CH_4 with the lowest reactivity for the catalyst used in this study. Therefore, light-off performance of the unburned HCs can be dominated by C_2H_4 and C_3H_6 species.   Moreover, complete or optimal conversion temperature ranges of C_2H_4 and C_3H_6 become narrower with the increase in oxygen concentration, and hence, it can be concluded that presence of surface oxygen species on the catalyst promote the decomposition of C_2H_4 and C_3H_6.

From the surface species experimental results, presence of adsorbed HC species and linearly adsorbed CO are confirmed on the platinum metal.   In addition, faster reaction or oxidation rate of intermediate HC species compared to the oxidation of linearly adsorbed surface CO are observed.   Moreover, early formation of CO_2 is detected so that the early C-C bond cracking to form the CO_2 is observed.

111

From the surface species measurement results and the literature studies, considerations and construction of reaction steps of C_2H_4 and C_3H_6 are discussed. In the surface reaction mechanism construction process, multiple site occupations of active Pt surface sites are included for both C_2H_4 and C_3H_6 surface reaction steps from the adsorption step to the oxidation steps. Then, the formation of the same intermediate surface species with three active Pt surface sites, which is C_2H_3, is proposed as a dominant stable intermediate species in the surface reaction mechanism. Systematic procedure of kinetic parameter estimation for fundamental chemistry set of CO / O_2 surface reaction mechanism, CO / H_2 / O_2 surface reaction mechanism and then, the final HC reaction mechanism are done and, developed step by step by carefully considering the kinetic parameters from the aspects of thermodynamic consistency.

Numerical modelling method, in which a single cell of monolith honeycomb reactor can be modelled not only along the gas flow channel direction but also into the washcoat layer direction independently with proper considerations of flow model, heat and mass transfer model, and the transport model into the washcoat layer, is presented, discussed and used, together with the proposed developed detailed surface reaction mechanism for numerical simulations.

From the numerically simulated results, numerical simulations by the proposed C_2H_4 / C_3H_6 detailed surface mechanism can reproduce the gas phase conversion experimental results in a wide range of oxygen concentration conditions from $\Phi = 0.15$ to $\Phi = 1.5$. Change in the light-off temperature by the surface coverage of multiple sited intermediate HC species for different oxygen concentration condition is proved, to show that presence of multiple active surface site occupied stable HC intermediate species is an important fact to consider in the heterogenous catalytic reaction modelling. Moreover, versatility of the reaction mechanism is validated by using multiple gas composition experiments, such as C_2H_4 / CO / O_2 / N_2, C_3H_6 / CO/ O_2 / N_2, C_2H_4 / C_3H_6 / CO/ O_2 / N_2, and C_2H_4 / C_3H_6 / CO/ O_2 / CO_2 systems, and results show good agreement. It is found that despite the washcoat diffusion phenomena is the dominant process in high temperature conversion region, complete oxidation temperature can be increased by the surface coverage of multiple sited species if the effective diffusion coefficient of the species is nearly the same. In the higher number of gas composition conditions, higher number of multiple sited stable intermediate species can affect the light-off performance, and transport properties of reactant gases into the washcoat layer can affect the complete oxidation temperature as well. Lastly, it is validated that the numerical model and the proposed reaction mechanism used in this study can reproduce good agreement over realistic exhaust gas conditions.

6.2   Suggestions for future work

As for the suggestions of future work,

1. For numerical model and the detailed surface reaction mechanism proposed and developed in this study, further improvements should be done by validating with a wider range of temperature, gas composition, realistic practical conditions and different metal loading of catalysts.
2. The detailed surface reaction mechanism should be improved by including other HC species which play important roles in HC emissions.
3. The detailed surface reaction mechanism should be improved by including NO_x emission surface reaction mechanism for the better application of realistic exhaust gas composition conditions and running conditions.
4. Numerical model presented in this study should be applied to different kinds of catalysts with their corresponding investigated physical parameters.

Appendix

Table A.1   Detailed surface reaction mechanism of C_2H_4/C_3H_6 for Pt/Al_2O_3

Reactions		A/S_0	E [kJ/mol]
R1	$O2 + 2.0\ Pt(S)$ → $2.0\ O(S)$	0.024	-
R2	$2.0\ O(S)$ → $O2 + 2.0\ Pt(S)$	1.35E+16	112.35
			ε_O=-120
R3	$CO + Pt(S)$ → $CO(S)$	0.84	-
R4	$CO(S)$ → $CO + Pt(S)$	1.50E+13	80.2
			ε_{CO}=-33
R5	$CO2 + Pt(S)$ → $CO2(S)$	0.005	-
R6	$CO2(S)$ → $CO2 + Pt(S)$	2.51E+09	70
R7	$CO(S) + O(S)$ → $CO2(S) + Pt(S)$	1.50E+25	127
			ε_{CO}=-33
R8	$CO2(S) + Pt(S)$ → $CO(S) + O(S)$	7.06E+07	235
			ε_O=60
R9	$H2 + 2.0\ Pt(S)$ → $2.0\ H(S)$	0.046	0
R10	$2.0\ H(S)$ → $H2 + 2.0\ Pt(S)$	5.00E+15	69.11
			ε_H=-6
R11	$H(S) + O(S)$ → $OH(S) + Pt(S)$	1.00E+18	70.8
R12	$OH(S) + Pt(S)$ → $H(S) + O(S)$	1.00E+21	130.69
R13	$OH(S) + H(S)$ → $H2O(S) + Pt(S)$	1.48E+21	17.4
R14	$H2O(S) + Pt(S)$ → $OH(S) + H(S)$	6.824E+20	67.56
R15	$2.0\ OH(S)$ → $H2O(S) + O(S)$	1.48E+21	48.2
R16	$H2O(S) + O(S)$ → $2.0\ OH(S)$	2.515E+20	38.17
R17	$H2O + Pt(S)$ → $H2O(S)$	0.75	0
R18	$H2O(S)$ → $H2O + Pt(S)$	5.013E+13	49.16
R19	$C3H6 + 2.0\ Pt(S)$ → $C3H6(2S)$	0.98	0
R20	$C3H6(2S)$ → $C3H6 + 2.0\ Pt(S)$	2.50E+13	72.36
R21	$C3H6(2S) + O(S) + Pt(S)$ → $C3H5(3S) + OH(S)$	1.20E+26	15
R22	$C3H5(3S) + OH(S)$ → $C3H6(2S) + O(S) + Pt(S)$	1.50E+18	146
R23	$C3H5(3S) + O(S)$ → $C3H4(3S) + OH(S)$	1.00E+20	19
R24	$C3H4(3S) + OH(S)$ → $C3H5(3S) + O(S)$	2.00E+18	104
R25	$C3H4(3S) + Pt(S)$ → $C2H3(3S) + CH(S)$	1.00E+20	69
R26	$C2H3(3S) + CH(S)$ → $C3H4(3S) + Pt(S)$	5.00E+17	139

	Reactions		A/S$_0$	E [kJ/mol]
R27	C2H4 + 2.0 Pt(S)	→ C2H4(2S)	0.3	-
R28	C2H4(2S)	→ C2H4 + 2.0 Pt(S)	1.00E+17	138.3
R29	C2H4(2S) + O(S) + Pt(S)	→ C2H3(3S) + OH(S)	2.00E+27	55
R30	C2H3(3S) + OH(S)	→ C2H4(2S) + O(S) + Pt(S)	4.00E+08	221
R31	C2H3(3S) + 2.0 O(S)	→ CH3(S) + CO2(S) + 3.0 Pt(S)	8.50E+23	55
R32	CH3(S) + CO2(S) + 3.0 Pt(S)	→ C2H3(3S) + 2.0 O(S)	3.50E+18	182
R33	CH3(S) + O(S)	→ CH2(S) + OH(S)	1.50E+21	75
R34	CH2(S) + OH(S)	→ CH3(S) + O(S)	2.80E+15	38
R35	CH2(S) + O(S)	→ CH(S) + OH(S)	5.00E+21	62
R36	CH(S) + OH(S)	→ CH2(S) + O(S)	2.00E+14	80
R37	CH(S) + O(S)	→ CO(S) + H(S)	5.00E+21	68
R38	CO(S) + H(S)	→ CH(S) + O(S)	2.00E+17	260

Kinetic parameters are given in Arrhenius and modified Arrhenius form for surface reactions as shown in equation (4.44) and (4.47), and in sticking coefficient including expression form for adsorption reactions as shown in equation (4.42).

The surface site density or total surface site concentration is 2.72 x 10^{-5} molm^{-2}.

Table A.2   Thermodynamic data for the gas phase and surface species used in this study

C3H6		120186C	3H	6	G	0300.00	5000.00	1000.00	1
0.06732257E+02	0.14908336E-01	-0.04949899E-04	0.07212022E-08	-0.03766204E-12	2
-0.09235703E+04	-0.13313348E+02	0.14933071E+01	0.02092517E+00	0.04486794E-04	3
-0.16689121E-07	0.07158146E-10	0.10748264E+04	0.16145340E+02		4
C2H4		121286C	2H	4	G	0300.00	5000.00	1000.00	1
0.03528418E+02	0.11485185E-01	-0.04418385E-04	0.07844600E-08	-0.05266848E-12	2
0.04428288E+05	0.02230389E+02	-0.08614880E+01	0.02796162E+00	-0.03388677E-03	3
0.02785152E-06	-0.09737879E-10	0.05573046E+05	0.02421148E+03		4
CO		121286C	1O	1	G	0300.00	5000.00	1000.00	1
0.03025078E+02	0.14426885E-02	-0.05630827E-05	0.10185813E-09	-0.06910951E-13	2
-0.14268350E+05	0.06108217E+02	0.03262451E+02	0.15119409E-02	-0.03881755E-04	3
0.05581944E-07	-0.02474951E-10	-0.14310539E+05	0.04848897E+02		4
CO2		121286C	1O	2	G	0300.00	5000.00	1000.00	1
0.04453623E+02	0.03140168E-01	-0.12784105E-05	0.02393996E-08	-0.16690333E-13	2
-0.04896696E+06	-0.09553959E+01	0.02275724E+02	0.09922072E-01	-0.10409113E-04	3
0.06866686E-07	-0.02117280E-10	-0.04837314E+06	0.10188488E+02		4
H2		121286H	2		G	0300.00	5000.00	1000.00	1
0.02991423E+02	0.07000644E-02	-0.05633828E-06	-0.09231578E-10	0.15827519E-14	2
-0.08350340E+04	-0.13551101E+01	0.03298124E+02	0.08249441E-02	-0.08143015E-05	3
-0.09475434E-09	0.04134872E-11	-0.10125209E+04	-0.03294094E+02		4
H2O		20387H	2O	1	G	0300.00	5000.00	1000.00	1
0.02672145E+02	0.03056293E-01	-0.08730260E-05	0.12009964E-09	-0.06391618E-13	2
-0.02989921E+06	0.06862817E+02	0.03386842E+02	0.03474982E-01	-0.06354696E-04	3
0.06968581E-07	-0.02506588E-10	-0.03020811E+06	0.02590232E+02		4
O2		121386O	2		G	0300.00	5000.00	1000.00	1
0.03697578E+02	0.06135197E-02	-0.12588420E-06	0.01775281E-09	-0.11364354E-14	2
-0.12339301E+04	0.03189165E+02	0.03212936E+02	0.11274864E-02	-0.05756150E-05	3
0.13138773E-08	-0.08768554E-11	-0.10052490E+04	0.06034737E+02		4
Pt(Pt)		dummy	Pt	1	S	300.00	3000.00	1000.00	1
0.00000000E+00	0.00000000E+00	0.00000000E+00	0.00000000E+00	0.00000000E+00	2
0.00000000E+00	0.00000000E+00	0.00000000E+00	0.00000000E+00	0.00000000E+00	3
0.00000000E+00	0.00000000E+00	0.00000000E+00	0.00000000E+00		4

```
C3H6(2Pt)                          Pt  1C    2H    4      S     300.00    3000.00    1000.00      1
   1.85583448E+00     2.09575461E-02    -2.21362246E-06   -7.09409927E-09    2.97758999E-12    2
  -8.13308559E+03     4.17679549E+00     1.85583448E+00    2.09575461E-02   -2.21362246E-06    3
  -7.09409927E-09     2.97758999E-12    -8.13308559E+03    4.17679549E+00                       4
C2H4(2Pt)                          Pt  1C    1H    2      S     300.00    3000.00    1000.00      1
   0.00000000E+00     0.00000000E+00     0.00000000E+00    0.00000000E+00    0.00000000E+00    2
   0.00000000E+00     0.00000000E+00     0.00000000E+00    0.00000000E+00    0.00000000E+00    3
   0.00000000E+00     0.00000000E+00     0.00000000E+00    0.00000000E+00                       4
C3H5(3Pt)                          Pt  1C    2H    3      S     300.00    3000.00    1000.00      1
   4.83555099E-01     1.80358010E-02     1.05860725E-05    2.44828289E-08    1.09002865E-11    2
   8.98332516E+03     7.16225851E+00     4.83555099E-01    1.80358010E-02    1.05860725E-05    3
  -2.44828289E-08     1.09002865E-11     8.98332516E+03    7.16225851E+00                       4
C3H4(3Pt)                          Pt  1C    2H    3      S     300.00    3000.00    1000.00      1
   0.00000000E+00     0.00000000E+00     0.00000000E+00    0.00000000E+00    0.00000000E+00    2
   0.00000000E+00     0.00000000E+00     0.00000000E+00    0.00000000E+00    0.00000000E+00    3
   0.00000000E+00     0.00000000E+00     0.00000000E+00    0.00000000E+00    0.00000000E+00    4
C2H3(3Pt)                          Pt  1C    2H    3      S     300.00    3000.00    1000.00      1
   1.00267303E+00     1.12120748E-02     1.08826725E-06    7.20229473E-09    3.28613356E-12    2
   3.80551264E+03     4.19828627E+00     1.00267303E+00    1.12120748E-02    1.08826725E-06    3
  -7.20229473E-09     3.28613356E-12     3.80551264E+03    4.19828627E+00                       4
CH(Pt)                             Pt  1C    1H    1      S     300.00    3000.00    1000.00      1
   3.76853374E-01     4.33007371E-03     1.26813836E-06   -4.03298591E-09    1.91710002E-12    2
   1.95692528E+04     2.10382533E+00     3.76853374E-01    4.33007371E-03    1.26813836E-06    3
  -4.03298591E-09     1.91710002E-12     1.95692528E+04    2.10382533E+00                       4
CH2(Pt)                            Pt  1C    1H    2      S     300.00    3000.00    1000.00      1
   8.33824124E-02     7.46370122E-03     1.10415461E-06   -5.20153053E-09    2.18780284E-12    2
   8.36101765E+03     2.55159890E+00     8.33824124E-02    7.46370122E-03    1.10415461E-06    3
  -5.20153053E-09     2.18780284E-12     8.36101765E+03    2.55159890E+00                       4
CH3(Pt)                            Pt  1C    1H    3      S     300.00    3000.00    1000.00      1
   8.57809745E-01     9.76143682E-03    -3.41063308E-06    2.57308727E-10   -3.74694697E-13    2
  -4.64570142E+03     1.16541017E-01     8.57809745E-01    9.76143682E-03   -3.41063308E-06    3
   2.57308727E-10    -3.74694697E-13    -4.64570142E+03    1.16541017E-01                       4
CO(Pt)                             Pt  1C    1O    1      S     300.00    3000.00    1000.00      1
   2.71277410E+00     1.59098477E-03    -3.74426457E-06    5.29775390E-09   -2.33787849E-12    2
  -3.06782579E+04    -4.40481342E+00     2.71277410E+00    1.59098477E-03   -3.74426457E-06    3
   5.29775390E-09    -2.33787849E-12    -3.06782579E+04   -4.40481342E+00                       4
```

CO2(Pt)		Pt 1C	1O	2	S	300.00	3000.00	1000.00	1
4.10777858E+00	2.27188590E-03	-4.99101157E-06		7.57467258E-09		-3.73435334E-12			2
-5.16326794E+04	-9.57779283E+00	4.10777858E+00		2.27188590E-03		4.99101157E-06			3
7.57467258E-09	-3.73435334E-12	-5.16326794E+04		-9.57779283E+00					4
H(Pt)		Pt 1H	1		S	300.00	3000.00	1000.00	1
9.90750227E-01	6.94689242E-04	-2.54107153E-09		-1.41451113E-10		0.00000000E+00			2
-4.51438985E+03	-4.19517661E+00	9.90750227E-01		6.94689242E-04		-2.54107153E-09			3
-1.41451113E-10	0.00000000E+00	-4.51438985E+03		-4.19517661E+00					4
H2O(Pt)		Pt 1H	2O	1	S	300.00	3000.00	1000.00	1
3.33746420E+00	3.52784936E-04	2.42556322E-06		-1.48206404E-09		0.00000000E+00			2
-3.62057980E+04	-9.72027689E+00	3.33746420E+00		3.52784936E-04		2.42556322E-06			3
-1.48206404E-09	0.00000000E+00	-3.62057980E+04		-9.72027689E+00					4
O(Pt)		Pt 1O	1		S	300.00	3000.00	1000.00	1
1.52967014E+00	-2.63766497E-04	1.28966071E-06		-8.04441298E-10		0.00000000E+00			2
-1.40432598E+04	-3.37596736E+00	1.52967014E+00		-2.63766497E-04		1.28966071E-06			3
-8.04441298E-10	0.00000000E+00	-1.40432598E+04		-3.37596736E+00					4
CO(Pt)		Pt 1C	1O	1	S	300.00	3000.00	1000.00	1
2.33488520E+00	3.22820417E-04	1.77158426E-06		-1.19563622E-09		0.00000000E+00			2
-2.57097938E+04	-7.40908407E+00	2.33488520E+00		3.22820417E-04		1.77158426E-06			3
-1.19563622E-09	0.00000000E+00	-2.57097938E+04		-7.40908407E+00					4

Stoichiometry of the reactions are adjusted in the user defined reaction mechanism of BOOST (Boost) software.

References

Abedi, A., Hayes, R., Votsmeier, M., Epling, W.S., 2012. Inverse hysteresis phenomena during CO and C3H6 oxidation over a Pt/Al2O3 catalyst. Catal. Letters 142, 930–935. https://doi.org/10.1007/s10562-012-0861-x

Almusaiteer, K.A., Chuang, S.S.C., 2000. Infrared Characterization of Rh Surface States and Their Adsorbates during the NO-CO Reaction. J. Phys. Chem. B 104, 2265–2272. https://doi.org/10.1021/jp9922155

Bamwenda, G.R., Ogata, A., Obuchi, A., Oi, J., Mizuno, K., Skrzypek, J., 1995. Selective reduction of nitric oxide with propene over platinum-group based catalysts: Studies of surface species and catalytic activity. Appl. Catal. B, Environ. 6, 311–323. https://doi.org/10.1016/0926-3373(95)00020-8

Barin, I., 1985. Thermochemical Data of Pure Substances, 3rd Edition, John Wiley & Sons Inc, New York, London, Sidney.

Bart, J.M., Pentenero, A., Prigent, M.F., 1992. Experimental Comparison Among Hydrocarbons and Oxygenated Compounds for their Elimination by Three-Way Automotive Catalysts 42–60. https://doi.org/10.1021/bk-1992-0495.ch004

Baxter, R.J., Hu, P., 2002. Insight into why the Langmuir-Hinshelwood mechanism is generally preferred. J. Chem. Phys. 116, 4379–4381. https://doi.org/10.1063/1.1458938

Bazin, P., Saur, O., Lavalley, J.C., Daturi, M., Blanchard, G., 2005. FT-IR study of CO adsorption on Pt/CeO2: Characterisation and structural rearrangement of small Pt particles. Phys. Chem. Chem. Phys. 7, 187–194. https://doi.org/10.1039/b414159h

Beebe, T.P., Albert, M.R., Yates, J.T., 1985. Infrared spectroscopic observation and characterization of surface ethylidyne on supported palladium on alumina. J. Catal. 96, 1–11. https://doi.org/10.1016/0021-9517(85)90354-9

Berlowitz, P., Megiris, C., Butt, J.B., Kung, H.H., 1985. Temperature-Programmed Desorption Study of Ethylene on a Clean, a H-Covered, and an O-Covered Pt(111) Surface. Langmuir 1, 206–212. https://doi.org/10.1021/la00062a005

Bird, R. B., Stewart, W. E. Lightfoot, E. N., 2006. Transport Phenomena, 6th Edition, John Wiley & Sons Inc., New York, London, Sydney.

Boost. 0000. Boost, exhaust gas aftertreatment simulation. AVL LIST GmbH.

Březina, J., Pečinka, R., Boutikos, P., Kočí, P., 2020. Comparison of dual CO light-off effect on Pt/CeO2/γ-Al2O3, Pd/CeO2/γ-Al2O3, Pt/γ-Al2O3 and Pd/γ-Al2O3 in the presence of C3H6. Chem. Eng. Sci. 218. https://doi.org/10.1016/j.ces.2020.115542

Burch, R., Watling, T.C., 1997. The difference between alkanes and alkenes in the

reduction of NO by hydrocarbons over Pt catalysts under lean-burn conditions. Catal. Letters 43, 19–23. https://doi.org/10.1023/a:1018974102756

Burnett, D.J., Gabelnick, A.M., Fischer, D.A., Marsh, A.L., Gland, J.L., 2005. In situ soft X-ray studies of ethylene oxidation mechanisms and intermediates on the Pt(111) surface. J. Phys. Chem. B 109, 5659–5666. https://doi.org/10.1021/jp048106u

Buzková Arvajová, A., Březina, J., Pečinka, R., Kočí, P., 2018. Modeling of two-step CO oxidation light-off on Pt/Γ-Al2O3 in the presence of C3H6 and NOx. Appl. Catal. B Environ. 233, 167–174. https://doi.org/10.1016/j.apcatb.2018.03.081

Captain, D.K., Amiridis, M.D., 1999. In situ FTIR studies of the selective catalytic reduction of NO by C3H6 over Pt/Al2O3. J. Catal. 184, 377–389. https://doi.org/10.1006/jcat.1999.2463

Captain, D.K., Roberts, K.L., Amiridis, M.D., 1998. The selective catalytic reduction of nitric oxide by propylene over Pt/SiO2. Catal. Today 42, 93–100. https://doi.org/10.1016/S0920-5861(98)00080-7

Chao, J., Zwolinski, B.J., 1975. Ideal gas thermodynamic properties of ethylene and propylene. J. Phys. Chem. Ref. Data 4, 251–262. https://doi.org/10.1063/1.555518

Chase, M.W., 1998. NIST-JANAF Thermochemical Tables. J. Phys. Chem. Ref. Data Monogr.

Chatterjee, D., Deutschmann, O., Warnatz, J., 2001. Detailed surface reaction mechanism in a three-way catalyst. Faraday Discuss. 119, 371–384. https://doi.org/10.1039/b101968f

Chauvin, C., Saussey, J., Lavalley, J.C., Idriss, H., Hindermann, J.P., Kiennemann, A., Chaumette, P., Courty, P., 1990. Combined infrared spectroscopy, chemical trapping, and thermoprogrammed desorption studies of methanol adsorption and decomposition on ZnAl2O4 and Cu/ZnAl2O4 catalysts. J. Catal. 121, 56–69. https://doi.org/10.1016/0021-9517(90)90216-7

Chesters, M.A., De La Cruz, C., Gardner, P., McCash, E.M., Pudney, P., Shahid, G., Sheppard, N., 1990. Infrared spectroscopic comparison of the chemisorbed species from ethene, propene, but-1-ene and cis- and trans-but-2-ene on Pt(111) and on a platinum/silica catalyst. J. Chem. Soc. Faraday Trans. 86, 2757–2763. https://doi.org/10.1039/FT9908602757

Coltrin, M.E., Kee, R.J., Rupley, F.M. and Meeks, E., 1996. Surface Chemkin III: A Fortran Package for Analyzing Heterogeneous Chemical Kinetics at a Solid Surface - Gas Phase Interface. Sandia National Laboratories Report, SAND96-8217 Unlimited Release.

Delphi, 2020. Passenger Cars and Light Duty Vehicles, Worldwide emissions standards. Delphi Technologies.

Demoulin, O., Navez, M., Ruiz, P., 2005. Investigation of the behaviour of a Pd/γ-Al2O3 catalyst during methane combustion reaction using in situ DRIFT spectroscopy. Appl. Catal. A Gen. 295, 59–70. https://doi.org/10.1016/j.apcata.2005.08.008

Deutschmann, O., 2015. Modeling of the Interactions Between Catalytic Surfaces and Gas-Phase. Catal. Letters 145, 272–289. https://doi.org/10.1007/s10562-014-1431-1

Deutschmann, O., Tischer, S., Correa, C., Chatterjee, D., Kleditzsch, S., Janardhanan, V.M., Mladenov, N., Minh, H. D., Karadeniz, H., Hettel, M., Menon, V., Banerjee, A., Goßler, H., DETCHEM Software package, 2.8 ed., www.detchem.com, Karlsruhe 2020.

Ermini, V., Finocchio, E., Sechi, S., Busca, G., Rossini, S., 2000. An FT-IR and flow reactor study of the conversion of propane on γ-Al2O3 in oxygen-containing atmosphere. Appl. Catal. A Gen. 190, 157–167. https://doi.org/10.1016/S0926-860X(99)00291-4

Finocchio, E., Daturi, M., Binet, C., Lavalley, J.C., Blanchard, G., 1999. Thermal evolution of the adsorbed methoxy species on CexZr1-xO2 solid solution samples: A FT-IR study. Catal. Today 52, 53–63. https://doi.org/10.1016/S0920-5861(99)00062-0

Fuller, E.N., Schettler, P.D., Giddings, J.C., 1966. A new method for the prediction of gas phase diffusion coefficients. Ind. Eng. Chem. 58, 19-27. https://doi.org/10.1021/ie50677a007

Gabelnick, A.M., Gland, J.L., 1999. Propylene deep oxidation on the Pt (111) surface: temperature programmed studies over extended converage ranges. J. Sur. Sci. 440, 340-350. https://doi.org/10.1016/S0039-6028(99)00684-6

Gabelnick, A.M., Capitano, A.T., Kane, S.M., Gland, J.L., Fischer, D.A., 2000. Propylene oxidation mechanisms and intermediates using in situ soft X- ray fluorescence methods on the Pt(111) surface. J. Am. Chem. Soc. 122, 143–149. https://doi.org/10.1021/ja992865m

Gervasini, A., Carniti, P., Ragaini, V., 1999. Studies of direct decomposition and reduction of nitrogen oxide with ethylene by supported noble metal catalysts. Appl. Catal. B Environ. 22, 201–213. https://doi.org/10.1016/S0926-3373(99)00053-3

Haneda, M., Sasaki, M., Hamada, H., 2015. Development of diesel hydrocarbon oxidation catalysts aimed at reducing platinum group metals usage. J. Japan Pet.

Inst. 58, 205–217. https://doi.org/10.1627/jpi.58.205

Hayes, R. E., Kolaczkowski, S.T., 1998. Introduction to catalytic combustion. USA: CRC press.

Hayes, R.E., Kolaczkowskib, S.T., Li, P.K.C., Awdry, S., 2000. Evaluating the effective diffusivity of methane in the washcoat of a honeycomb monolith. Appl. Catal. B Environ. 25, 93–104. https://doi.org/10.1016/S0926-3373(99)00122-8

Hazlett, M.J., Epling, W.S., 2016. Spatially resolving CO and C3H6 oxidation reactions in a Pt/Al2O3 model oxidation catalyst. Catal. Today 267, 157–166. https://doi.org/10.1016/j.cattod.2015.11.033

Hazlett, M.J., Moses-Debusk, M., Parks, J.E., Allard, L.F., Epling, W.S., 2017. Kinetic and mechanistic study of bimetallic Pt-Pd/Al2O3 catalysts for CO and C3H6 oxidation. Appl. Catal. B Environ. 202, 404–417. https://doi.org/10.1016/j.apcatb.2016.09.034

Hinokuma, S., Matsuki, S., Kawabata, Y., Shimanoe, H., Kiritoshi, S., Machida, M., 2016. Copper Oxides Supported on Aluminum Oxide Borates for Catalytic Ammonia Combustion. J. Phys. Chem. C 120, 24734–24742. https://doi.org/10.1021/acs.jpcc.6b07157

Holmgren, A., Andersson, B., Duprez, D., 1999. Interactions of CO with Pt/ceria catalysts. Appl. Catal. B Environ. 22, 215–230. https://doi.org/10.1016/S0926-3373(99)00047-8

Karadeniz, H., Karakaya, C., Tischer, S., Deutschmann, O., 2013. Numerical modeling of stagnation-flows on porous catalytic surfaces: CO oxidation on Rh/Al2O3. Chem. Eng. Sci. 104, 899–907. https://doi.org/10.1016/j.ces.2013.09.038

Kaviani, M., 1991. Principles of Heat Transfer in Porous Media, Mechanical Engineering Series, Springer, Berlin Heidelberg, New York.

Kesmodel, L.L., Dubois, L.H., Somorjai, G.A., 1979. LEED analysis of acetylene and ethylene chemisorption on the Pt(111) surface: Evidence for ethylidyne formation. J. Chem. Phys. 70, 2180–2188. https://doi.org/10.1063/1.437772

Koestner, R.J., Frost, J.C., Stair, P.C., Van Hove, M.A., Somorjai, G.A., 1982. Evidence for the formation of stable alkylidyne structures from C3 and C4 unsaturated hydrocarbons adsorbed on the pt(111) single crystal surface. Surf. Sci. 116, 85–103. https://doi.org/10.1016/0039-6028(82)90680-X

Koop, J., Deutschmann, O., 2009. Detailed surface reaction mechanism for Pt-catalyzed abatement of automotive exhaust gases. Appl. Catal. B Environ. 91, 47–58. https://doi.org/10.1016/j.apcatb.2009.05.006

Kota, A.S., Dadi, R.K., Luss, D., Balakotaiah, V., 2017. Analysis of light-off during

oxidation of reactant mixtures on Pt/Al2O3 using micro-kinetic models. Chem. Eng. Sci. 166, 320–333. https://doi.org/10.1016/j.ces.2017.02.050

Kubo, S., 1995. Formation and Emission Characteristics of Unburned Hydrocarbons During Cold Start of a Spark-Ignited Engine System (in Japanese). Toyota Central R & D Labs Review. 30, 23–33.

Kummer, J.T., 1980. Catalysts for automobile emission control. Stud. Surf. Sci. Catal. 6, 177–199. https://doi.org/10.1016/S0167-2991(08)63984-1

Lindon, J., 2010. Encyclopedia of Spectroscopy and Spectrometry, Encyclopedia of Spectroscopy and Spectrometry, 1210-1217.

Liu, Z., Oh, K.S., Woo, S.I., 2006. Overview on the selective lean NO x reduction by hydrocarbons over Pt-based catalysts. Catal. Surv. from Asia 10, 8–15. https://doi.org/10.1007/s10563-006-9002-0

Malamis, S.A., Li, M., Epling, W.S., Harold, M.P., 2018. Steady state and lean-rich cycling study of a three-way NOX storage catalyst: Experiments. Appl. Catal. B Environ. 237, 588–602. https://doi.org/10.1016/j.apcatb.2018.06.001

Matsouka, V., Konsolakis, M., Lambert, R.M., Yentekakis, I. V., 2008. In situ DRIFTS study of the effect of structure (CeO2-La2O3) and surface (Na) modifiers on the catalytic and surface behaviour of Pt/γ-Al2O3 catalyst under simulated exhaust conditions. Appl. Catal. B Environ. 84, 715–722. https://doi.org/10.1016/j.apcatb.2008.06.004

Mhadeshwar, A.B., Wang, H., Vlachos, D.G., 2003. Thermodynamic Consistency in Microkinetic Development of Surface Reaction Mechanisms. J. Phys. Chem. B 107, 12721–12733. https://doi.org/10.1021/jp034954y

Mittendorfer, F., Thomazeau, C., Raybaud, P., Toulhoat, H., 2003. Adsorption of unsaturated hydrocarbons on Pd(111) and Pt(111): A DFT study. J. Phys. Chem. B 107, 12287–12295. https://doi.org/10.1021/jp035660f

Mladenov, N., Koop, J., Tischer, S., Deutschmann, O., 2010. Modeling of transport and chemistry in channel flows of automotive catalytic converters. Chem. Eng. Sci. 65, 812–826. https://doi.org/10.1016/j.ces.2009.09.034

Mohsin, S.B., Trenary, M., Robota, H.J., 1988. INFRARED IDENTIFICATION OF THE LOW-TEMPERATURE FORMS OF ETHYLENE ADSORBED ON Pt/Al2O3. J. Phys. Chem. 92, 5229–5233. https://doi.org/10.1021/j100329a032

Nykänen, L., Honkala, K., 2013. Selectivity in propene dehydrogenation on Pt and Pt3Sn surfaces from first principles. ACS Catal. 3, 3026–3030. https://doi.org/10.1021/cs400566y

Nykänen, L., Honkala, K., 2011. Density functional theory study on propane and

propene adsorption on Pt(111) and PtSn alloy surfaces. J. Phys. Chem. C 115, 9578–9586. https://doi.org/10.1021/jp1121799

Paffett, M.T., Gebhard, S.C., Windham, R.G., Koel, B.E., 1989. Chemisorption of ethylene on ordered Sn/Pt(111) surface alloys. Surf. Sci. 223, 449–464. https://doi.org/10.1016/0039-6028(89)90673-0

Perger, T., Kovács, T., Turányi, T., Treviño, C., 2005. Determination of the adsorption and desorption parameters for ethene and propene from measurements of the heterogeneous ignition temperature. Combust. Flame 142, 107–116. https://doi.org/10.1016/j.combustflame.2005.03.001

Perry, R.H., Green, D.W., Southard, M.W., 2018. Perry's Chemical Engineer's Handbook, 9th Edition, McGraw Hill, New York.

Rankovic, N., Nicolle, A., Berthout, D., Da Costa, P., 2011. Kinetic modeling study of the oxidation of carbon monoxide-hydrogen mixtures over Pt/Al2O3 and Rh/Al2O3 catalysts. J. Phys. Chem. C 115, 20225–20236. https://doi.org/10.1021/jp205476y

Reid, R.C., Prausnitz, J.M., Poling, B.E., 1988. The properties of gases and liquids, 4th Edition, Mc Graw Hill, New York.

Sasmaz, E., Wang, C., Lance, M.J., Lauterbach, J., 2017. In situ spectroscopic investigation of a Pd local structure over Pd/CeO2 and Pd/MnOx-CeO2 during CO oxidation. J. Mater. Chem. A 5, 12998–13008. https://doi.org/10.1039/c7ta00696a

Satsuma, A., Shimizu, K.I., 2003. In situ FT/IR study of selective catalytic reduction of NO over alumina-based catalysts. Prog. Energy Combust. Sci. 29, 71–84. https://doi.org/10.1016/S0360-1285(02)00033-3

Schießer, W.; Vinek , H.; Jentys, A., 2001. Surface species during catalytic reduction of NO by propene studied by in situ IR-spectroscopy over Pt supported on mesoporous Al2O3 with MCM-41 type structure. Appl. Catal. B Environ. 33, 263–274.

Sharma, R.K., Cresswell, D.L., Newson, E.J., Newson, E.J., 1991. Effective Diffusion Coefficients and Tortuosity Factors for Commercial Catalysts. Ind. Eng. Chem. Res. 30, 1428–1433. https://doi.org/10.1021/ie00055a004

Shen, S.C., Kawi, S., 2001. Kinetic studies of selective catalytic reduction of nitric oxide by propylene on Pt/MCM-41 catalyst. Catal. Today 68, 245–254. https://doi.org/10.1016/S0920-5861(01)00284-X

Shimokuri, D., Murakami, H., Hinokuma, S., Matsumoto, Y., Naing, S., Naito, K., Yokohata, H., Takebayashi, H., Miyoshi, A., 2020. Development of Surface Reaction Mechanisms of CO/O2 on Pt and Rh for Three-Way Catalyst based on

Gas Phase and Surface Species Analyses. Combust. Sci. Technol. 00, 1–21. https://doi.org/10.1080/00102202.2020.1731486

Sieder, E.N., Tate, G.E., 1936. Heat Transfer and Pressure Drop of Liquids in Tubes. Ind. Eng. Chem. 28, 1429–1435. https://doi.org/10.1021/ie50324a027

Srivastava, D.K., Agarwal, A.K., Datta, A., Maurya, R.K., 2018. Advances in Internal Combustion Engine Research. Springer Nature Singapore Pte Ltd. https://doi.org/10.1007/978-981-10-7575-9

Staff writers, 2020, CarParts.com, P2096 Code: Post Catalyst Fuel Trim System Too Lean (Bank 1). https://www.carparts.com/blog/p2096-code-post-catalyst-fuel-trim-system-too-lean-bank-1

Stotz, H., Maier, L., Deutschmann, O., 2017. Methane Oxidation over Palladium: On the Mechanism in Fuel-Rich Mixtures at High Temperatures. Top. Catal. 60, 83–109. https://doi.org/10.1007/s11244-016-0717-5

Taylor, R., Krishna, R., 1993. Multicomponent Mass Transfer, John Wiley & Sons Inc., New York, London, Sydney.

Trautmann, S., Baerns, M., 1994. Infrared spectroscopic studies of CO adsorption on rhodium supported by SiO2, Al2O3, and TiO2. J. Catal. https://doi.org/10.1006/jcat.1994.1352

Tsai, Y.L., Xu, C., Koel, B.E., 1997. Chemisorption of ethylene, propylene and isobutylene on ordered Sn/Pt(111) surface alloys. Surf. Sci. 385, 37–59. https://doi.org/10.1016/S0039-6028(97)00114-3

Twiss, S.B., Teague, D.M., Bozek, J.W., Sink, M. V., 1955. Application of infrared spectroscopy to exhaust gas analysis. J. Air Pollut. Control Assoc. 5, 75–83. https://doi.org/10.1080/00966665.1955.10467692

Valcárcel, A., Ricart, J.M., Clotet, A., Illas, F., Markovits, A., Minot, C., 2006. Theoretical study of dehydrogenation and isomerisation reactions of propylene on Pt(111). J. Catal. 241, 115–122. https://doi.org/10.1016/j.jcat.2006.04.022

Valcárcel, A., Ricart, J.M., Clotet, A., Markovits, A., Minot, C., Illas, F., 2002. Theoretical study of the structure of propene adsorbed on Pt(111). Surf. Sci. 519, 250–258. https://doi.org/10.1016/S0039-6028(02)02220-3

Voltz, S.E., Morgan, C.R., Liederman, D., Jacob, S.M., 1973. Kinetic Study of Carbon Monoxide and Propylene Oxidation on Platinum Catalysts. Ind. Eng. Chem. Prod. Res. Dev. 12, 294–301. https://doi.org/10.1021/i360048a006

Wakao, N., Smith, J.M., 1962. Diffusion in catalyst pellets. Chem. Eng. Sci. 17, 825–834. https://doi.org/10.1016/0009-2509(62)87015-8

Wang, H.P., Yates, J.T., 1984. Infrared spectroscopic study of N2 chemisorption on

rhodium surfaces. J. Phys. Chem. 88, 852–856.
https://doi.org/10.1021/j150649a006

Watwe, R.M., Cortright, R.D., Mavrikakis, M., Nørskov, J.K., Dumesic, J.A., 2001.
Density functional theory studies of the adsorption of ethylene and oxygen on
Pt(111) and Pt3Sn(111). J. Chem. Phys. 114, 4663–4668.
https://doi.org/10.1063/1.1346685

Zaera, F., French, C.R., 1999. Mechanistic changes in the conversion of ethylene to
ethylidyne on transition metals induced by changes in surface coverages. J. Am.
Chem. Soc. 121, 2236–2243. https://doi.org/10.1021/ja981712g

Zaki, M.I., Hasan, M.A., Pasupulety, L., 2001. Surface reactions of acetone on Al2O3,
TiO2, ZrO2, and CeO2: IR spectroscopic assessment of impacts of the surface
acid-base properties. Langmuir 17, 768–774. https://doi.org/10.1021/la000976p